

Reduced gravity and microgravity Integrated Computational Materials Engineering (ICME)

*Andrew O'Connor and Louise Littles
NASA Marshall Space Flight Center,
Huntsville, AL*

*Brodan Richter and Edward Glaessgen
NASA Langley Research Center,
Hampton, VA*

*Alain Karma
Northeastern University, Boston, MA*

*Douglas Matson
Tufts University, Medford, MA*

*Peter Voorhees
Northwestern University, Evanston, IL*

*Fredrick Michael, Benjamin Rupp, Michael
SanSoucie, Jeffrey Sowards, and Jeffrey
West
NASA Marshall Space Flight Center,
Huntsville, AL*

*George R. Weber
NASA Langley Research Center,
Hampton, VA*

*Joshua D. Pribe and Vesselin Yamakov
Analytical Mechanics Associates,
Hampton, VA*

*Saikumar R. Yeratapally
Science and Technology Corporation,
Hampton, VA*

*Vernon Cole and Rae Waxman
CFD Research Corporation, Huntsville, AL*

NASA STI Program Report Series

Since its founding, NASA has been dedicated to the advancement of aeronautics and space science. The NASA scientific and technical information (STI) program plays a key part in helping NASA maintain this important role.

The NASA STI program operates under the auspices of the Agency Chief Information Officer. It collects, organizes, provides for archiving, and disseminates NASA's STI. The NASA STI program provides access to the NTRS Registered and its public interface, the NASA Technical Reports Server, thus providing one of the largest collections of aeronautical and space science STI in the world. Results are published in both non-NASA channels and by NASA in the NASA STI Report Series, which includes the following report types:

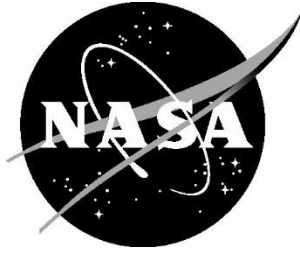
- **TECHNICAL PUBLICATION.** Reports of completed research or a major significant phase of research that present the results of NASA Programs and include extensive data or theoretical analysis. Includes compilations of significant scientific and technical data and information deemed to be of continuing reference value. NASA counterpart of peer-reviewed formal professional papers but has less stringent limitations on manuscript length and extent of graphic presentations.
- **TECHNICAL MEMORANDUM.** Scientific and technical findings that are preliminary or of specialized interest, e.g., quick release reports, working papers, and bibliographies that contain minimal annotation. Does not contain extensive analysis.
- **CONTRACTOR REPORT.** Scientific and technical findings by NASA-sponsored contractors and grantees.

- **CONFERENCE PUBLICATION.** Collected papers from scientific and technical conferences, symposia, seminars, or other meetings sponsored or co-sponsored by NASA.
- **SPECIAL PUBLICATION.** Scientific, technical, or historical information from NASA programs, projects, and missions, often concerned with subjects having substantial public interest.
- **TECHNICAL TRANSLATION.** English-language translations of foreign scientific and technical material pertinent to NASA's mission.

Specialized services also include organizing and publishing research results, distributing specialized research announcements and feeds, providing information desk and personal search support, and enabling data exchange services.

For more information about the NASA STI program, see the following:

- Access the NASA STI program home page at <http://www.sti.nasa.gov>.



Reduced gravity and microgravity Integrated Computational Materials Engineering (ICME)

*Andrew O'Connor and Louise Littles
NASA Marshall Space Flight Center,
Huntsville, AL*

*Brodan Richter and Edward Glaessgen
NASA Langley Research Center,
Hampton, VA*

*Alain Karma
Northeastern University, Boston, MA*

*Douglas Matson
Tufts University, Medford, MA*

*Peter Voorhees
Northwestern University, Evanston, IL*

*Fredrick Michael, Benjamin Rupp, Michael
SanSoucie, Jeffrey Sowards, and Jeffrey
West
NASA Marshall Space Flight Center,
Huntsville, AL*

*George R. Weber
NASA Langley Research Center,
Hampton, VA*

*Joshua D. Pribe and Vesselin Yamakov
Analytical Mechanics Associates,
Hampton, VA*

*Saikumar R. Yeratapally
Science and Technology Corporation,
Hampton, VA*

*Vernon Cole and Rae Waxman
CFD Research Corporation, Huntsville, AL*

National Aeronautics and
Space Administration

Marshall Space Flight Center
Huntsville, AL

April 2025

The use of trademarks or names of manufacturers in this report is for accurate reporting and does not constitute an official endorsement, either expressed or implied, of such products or manufacturers by the National Aeronautics and Space Administration.

Available from:

NASA STI Program / Mail Stop 050
NASA Langley Research Center
Hampton, VA 23681-2199

Table of Contents

1. Introduction.....	5
1.1. Integrated Computational Materials Engineering (ICME).....	5
1.2. Microgravity materials science	9
1.3. BPS Decadal Survey	9
1.4. What has been done, what remains to be done, and where does BPS fit in?	11
2. Thermophysical properties.....	11
2.1. Experimental - Vignettes showcasing past BPS successes in thermophysical properties measurements and associated existing facilities	12
2.2. Computational thermophysical properties	15
2.3. Future	18
Experimental	18
Computational.....	19
2.4. BPS role in future.....	19
Historical datasets	19
Support existing ground and flight facilities.....	19
Advocate for new flight facilities on commercial LEO destinations	19
Invest in HECC via SMD allocations to support PINN/DFT of thermophysical properties	19
3. Solidification & fluids.....	19
3.1. Experimental	20
Historical flight datasets.....	20
Modern benchmark cases using flight experimental data	21
3.2. Computational.....	26
PRISMS-PF.....	27
MOOSE.....	33
An example case of fluids-solidification coupling using historical datasets from BPS-funded flight experiments	36
Computational architectures and infrastructure currently available	39
3.3. Future	41
Experimental	41
Computational.....	42
3.4. BPS role in future.....	42
Historical datasets	42
Community, open-source codes	43
“Can Do” science with existing equipment and facilities	43

Fund further solidification investigations	43
Fluids and coupling to solidification.....	44
4. Meso-/macro-scale.....	44
4.1. Computational.....	44
Dendritic Needle Network (DNN).....	44
Cellular automata - finite element (CAFE).....	45
Hybrid Potts PF - kinetic Monte Carlo with SPPARKS	45
Crystal plasticity	47
4.2. BPS role in future.....	48
5. Uncertainty quantification.....	48
5.1. Typical UQ tasks.....	49
Sensitivity study using PRISMS-PF (2D) and DSI-R parameters	49
Directed acyclic graphs.....	50
CALPHAD as an example of a technique requiring UQ	51
5.2. Future and BPS role	52
6. Conclusion: accomplishments, finding, and recommendations	52
6.1. Accomplishments arising from this study group	53
6.2. Findings.....	54
6.3. Recommendations.....	55
RECOMMENDATION 1.A: Quantify and drive down uncertainty in inputs and models for engineering-relevant data to:.....	55
RECOMMENDATION 1.B: Champion “Can Do” science with existing ground and flight facilities and hardware.....	55
RECOMMENDATION 1.C: Investigate rapid solidification, concentrated alloys, multicomponent engineering alloys, etc. to close science gaps and reduce uncertainty via anchoring datasets.....	56
RECOMMENDATION 1.D: Engage with STMD and ESDMD to identify "experiments of opportunity” and ensure proper instrumentation for validation dataset collection	56
RECOMMENDATION 1.E: Identify facilities requirements for future experimental platforms (i.e. CLDs).....	56
RECOMMENDATION 2.A: Contributing to and leveraging open-source codes.....	56
RECOMMENDATION 2.B: Becoming a visible and trusted partner in the ICME community.....	56
RECOMMENDATION 2.C: Support the transition of legacy codes to modern architectures with enhanced capabilities and ease-of-maintenance (e.g. CPU-bound to GPU-bound, multi-GPU multi-node)	57
RECOMMENDATION 2.D: Explore opportunities to employ cognitive (i.e. AI/ML) computing rather than traditional algorithmic (von Neumann) computing.....	57

RECOMMENDATION 2.E: Support/mentor research teams across multiple academic partners and NASA Centers	57
Bibliography	59
Supplementary material	69
Acknowledgements.....	73
Disclaimer.....	73

1. Introduction

This study seeks to motivate and focus NASA Biological and Physical Sciences (BPS) Division's engagement within the broader Integrated Computational Materials Engineering (ICME) community to understand the phenomena underlying material processing, structure, and properties in the microgravity environment of space and to thereby support future space exploration efforts. Understanding the physical phenomena and properly capturing them in computational models will enable rapid advances in materials for both terrestrial and space use – for example, through better predictions of in-space joining, welding, and manufacturing. We have assembled a diverse, intermural team that connects NASA civil servants and contractors with external academic and industrial partners. A broad range of ICME-relevant disciplines are covered by this team, including but not limited to solidification simulations, thermodynamics and kinetics modeling, atomistic modeling, computational fluid dynamics, plasticity and process modeling, uncertainty quantification, thermophysical property measurements, structural and fracture mechanics, microgravity flight experiments on solidifying alloys, and advanced computing infrastructure. The team's expertise and membership is not exhaustive but serves as a starting point to begin investigations of ICME with respect to BPS. This BPS ICME study group sought to survey the heritage & current flight experiments, current ICME engagement, and future opportunities concentrating on the BPS-relevant fields of thermophysical properties, solidification kinetics, coupled solidification-fluids, and structures up to the grain length scale (mesoscale). These fields were chosen as they represent the disciplines most relevant to metal alloys, which serve as a unifying theme throughout this report to assist the reader in understanding the links and other relations between flight experiments and ICME tools. The emergence of additive and in-space manufacturing gives emphasis to studies of rapid solidification in metal alloys. Certainly, other microgravity materials science themes are vital to study – for instance, semiconductor crystal growth, optical fiber drawing, etc. – but their inclusion is beyond the scope of this report. The study group also documented the required computational resources, elucidated scale bridging¹, and reviewed how uncertainty in this ICME framework can not only be quantified but also how uncertainty reduction via validation datasets is a *raison d'être* for microgravity materials science – generating theory and physically validated computational models useful for understanding materials both in space and on the Earth.

1.1. Integrated Computational Materials Engineering (ICME)

NASA's mission to travel beyond near earth orbit for a sustained human presence in space will require tremendous and rapid innovation. The equipment, processes, and understanding humans use to live on Earth are not necessarily applicable in space environments, even on extraterrestrial surfaces such as the Moon. Under the conditions of high vacuum, cryogenic to hot temperature swings, and reduced gravity, few areas of expertise have more gaps in understanding than materials science. For example, soldering is a common manufacturing method used to create circuits and join electronics. However, solder joints exhibit excessive porosity when fabricated in microgravity, resulting in degradation of mechanical strength and electrical conductivity [1]. Traditionally, experiments were required to reveal material-related issues like these in space environments. However, the adoption of ICME approaches allows prediction of the response of materials under conditions unique to space, such as microgravity, by capturing physics in computational tools to reduce the burden of experimentation. The materials engineer-scientist and component designer can thus make informed, quantitative decisions rather than relying solely on intuition or experimentation. Thus, well-developed ICME tools would greatly accelerate the infusion of innovative materials and processes necessary to achieve a sustainable presence in the space environment. Additionally, with uncertainty quantified and models verified and validated, computationally informed qualification and certification can be applied to terrestrial and in-space materials and processes. For instance, it may be possible to certify an in-space weld based on its known composition and process parameters captured *in situ* and simulated via a computational model without needing expensive and time-consuming physical inspection or mechanical testing in space. The challenge of traditional materials design and performance prediction is illustrated by the example of novel alloy design shown in Figure 1. After identification of the need for a new alloy, the cycle starts by choosing a composition and then a processing path. The sample is then created and tested. Initial compositions are unlikely to achieve the

¹ linking fundamental thermodynamic models derived from first principles *ab initio* and atomistic molecular dynamics via solidification microstructures given by the present study's simulations to mesoscale plasticity models and macroscale property predictions

desired performance. Thus, a new material composition is chosen, and the process is repeated. Not surprisingly, this empirical approach to materials design is costly, laborious, and time-consuming. These costs form barriers to the introduction of new materials and to modifying existing ones for the requirements of space applications. The ICME paradigm aims to break this Sisyphean cycle. Data derived from experiment, simulation, and computational methods drastically decrease the expense to yield a material with the desired performance. A desired set of performance metrics is used to identify properties necessary for this performance. Next the microstructure needed to give those properties is delineated. Finally, the processing needed to create the desired microstructure is selected. This materials development approach is well described by a systems design chart as in Figure 2. This shows the connections between performance, properties, structure, and processing that are needed to engineer a high temperature Co-alloy, for example. The lines that connect one box to another are provided by computational tools, with experiments providing datasets to validate such tools. These process-structure-property/performance (PSP/P) relationships are informed and linked by uncertainty throughout. It is critical to perform uncertainty quantification (UQ) so that these relationships and the eventually resulting materials and processes can be qualified and certified. Figure 2 shows a theoretical model for systems design of a material using this systems design PSP/P framework [2], with Figure 3 demonstrating several of the computational tools that could be used to achieve this in the context of a powder-based additive manufacturing method [3]. Empirical data feeding simulations and simulations guiding experimentation then establish a virtuous cycle that accelerates materials design and innovation. The Materials Genome Initiative is one effort dedicated to bringing this new paradigm into fruition [4]. ICME methods to achieve computationally informed qualification and certification (Q&C) are also critical to actual infusion of these materials and processes into industrial and widespread use. A recently awarded NASA Space Technology Research Institute, the Institute for Model-based Quantification and Certification for Additive Manufacturing, seeks to advance the use of ICME tools for Q&C [5]. However, these goals require data that is high quality and computational methods that are verified and validated (V&V). These methods may be verified against BPS-supported research codes and validated using BPS-supported flight experiments providing validation datasets.

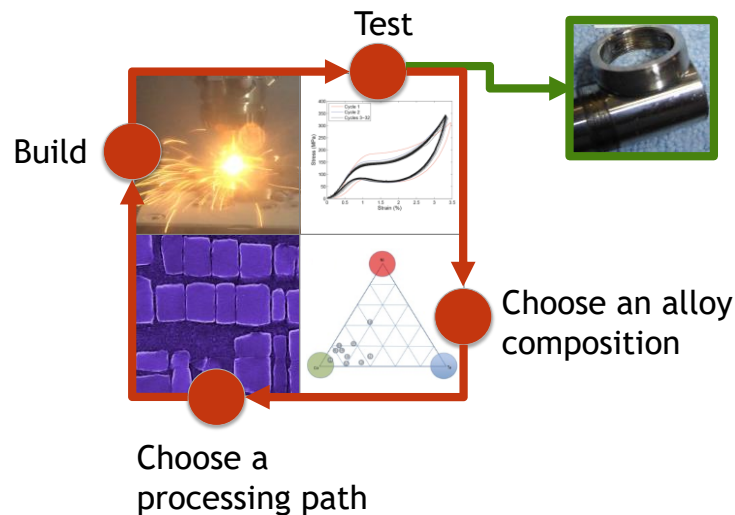


Figure 1: The cycle of alloy development.

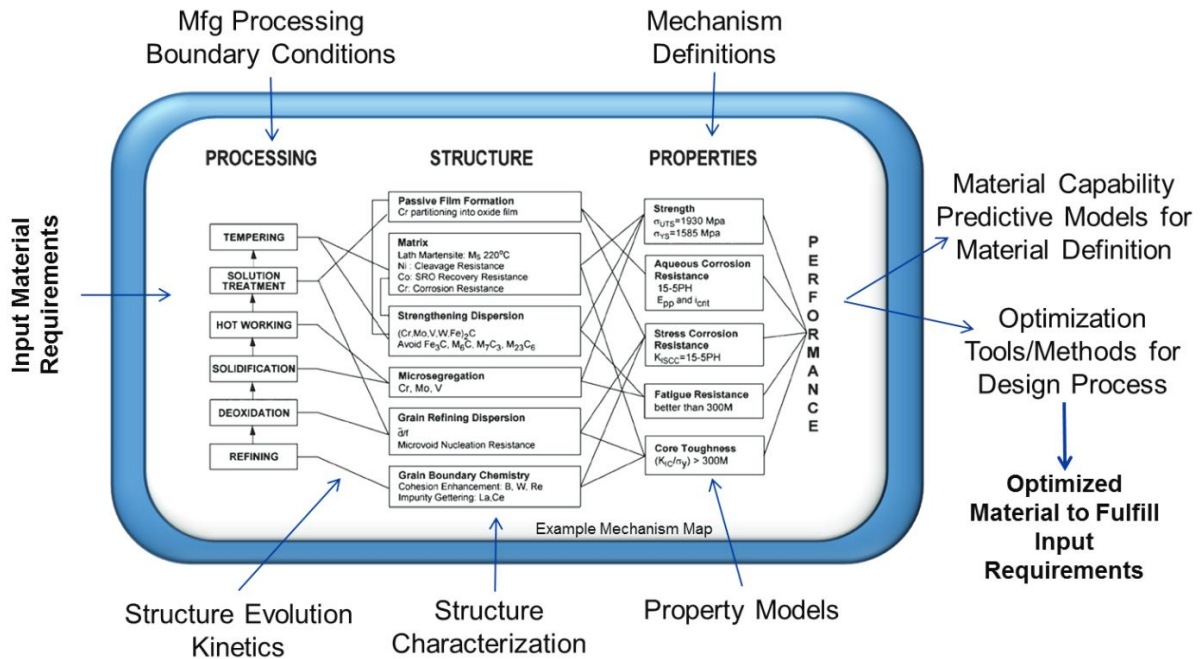


Figure 2: A systems design diagram for a notional material system indicates how models of processing, microstructural evolution (solidification, precipitation, etc.), and mesoscale phenomena like grain boundaries can be linked to enable model-based systems engineering of an optimized material system based on defined performance requirements and bottom-up constraints [2].

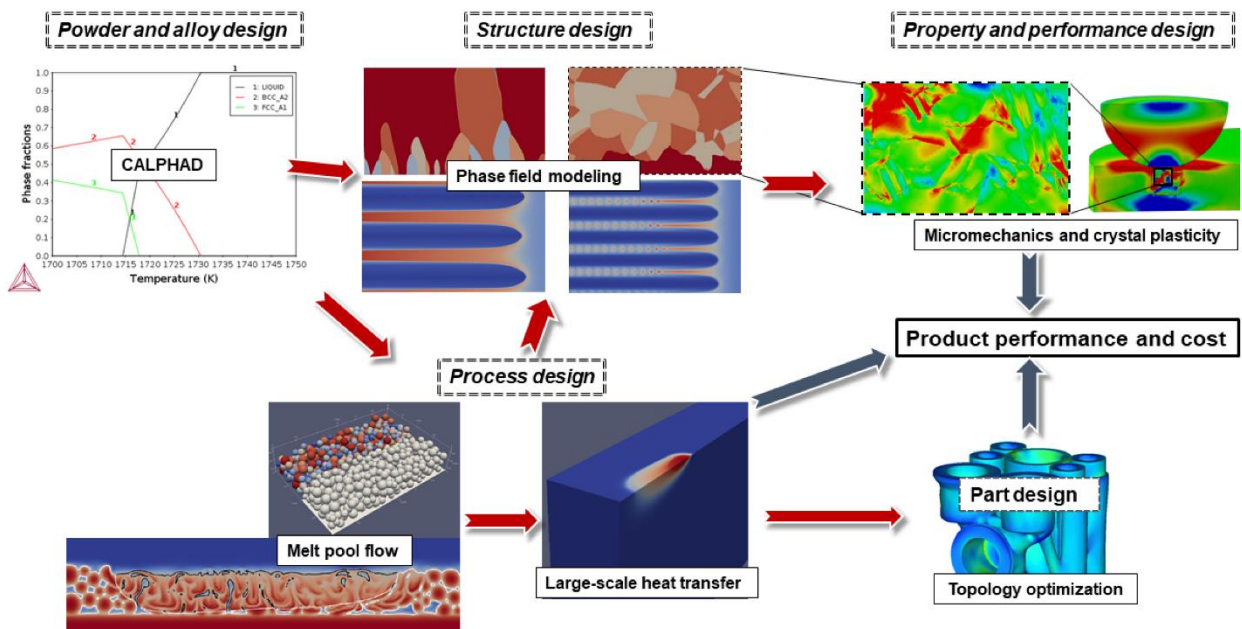


Figure 3: The interaction between process, part, and materials design in the context of powder-based additive manufacturing; examples of computational techniques used for each stage of product design [3]. Figure from T. Pinomaa et al., "Process-Structure-Properties-Performance Modeling for Selective Laser Melting" licensed under CC BY 4.0.

ICME has experienced a tremendous growth within the past few decades as computational resources and tools have greatly advanced. It uses physics-based simulations, statistical models, and materials property databases to better understand the response of materials to certain stimuli while minimizing costly experiments. For NASA, ICME has the potential to effectively predict and solve challenges with using, producing, or processing materials in space-

relevant vacuum, cryogenic, or microgravity conditions while reducing the investment in cost, time, and risk associated with performing experiments [2]. Its methodology can be used at any stage of the material's life span, from material design to process simulation to property & performance simulation to recycling [2]. This flexibility is foundational to the "integrated" piece of ICME. ICME is a collection of tools with more than one that is often utilized to answer a specific question. A particular ICME tool may focus on a specific length scale: nanoscale (atoms), micro-scale (microns), or the meso-scale (centimeters). In addition, the time scales accessible with each approach vary widely, with atomistic methods on the pico- to nano-second timescales, to mesoscale methods on the microsecond to multi-year scale, to a timescale of years representing service life of components. Unfortunately, today's computing resources constrain and limit in-built integration from the nanoscale to the macro-scale. Rather, ICME often employs an information passing strategy – wherein information on lower length scales and shorter time scales are passed to tools at the next higher levels [6].

Three illustrative applications of ICME tools follow:

1. Soto-Medina et al. connected several ICME techniques to guide investigation of the stabilizing effect of manganese additions on a desirable intermetallic phase in the lightweight aluminum-iron-silicon alloy system [7]. First, the compositional range of the intermetallic phase was predicted using the Thermo-Calc® calculation of phase diagrams (CALPHAD) tool, narrowing the experimental range [8]. They then used density functional theory (DFT), a nano-scale ICME tool, to calculate the Gibbs free energy of various amounts of Mn additions and how manganese atoms substitute for aluminum, iron, and silicon atoms within the desired intermetallic phase. The crystal structures necessary for DFT were taken from open databases such as the Materials Project Database [9], highlighting the integration between accessible data and simulation. Thus, alloy compositions that increased stability of the desirable intermetallic were selected via data and simulation and then experimentally verified. The narrowing of the experimental range by CALPHAD and DFT tools allowed optimization of a lightweight, high-temperature alloy suitable for highly efficient combustion engines under an accelerated development cycle.
2. A study by Keller et al. utilized a combination of phase field (PF), CALPHAD, and thermal predictions using finite element analysis (FEA) to assess the additive manufacturability of nickel-base superalloys [10]. A CALPHAD database was used to obtain the thermal properties of one such alloy, Inconel 625. These properties were fed into a thermal FEA model to predict the melt pool shape in an additive manufacturing process. A PF model was then used to simulate the microstructural evolution, with validation by comparing the simulated microstructure to the as-built microstructure. As such, multiple physical phenomena and length scales were bridged via ICME to understand the response of a certain superalloy to a novel additive manufacturing application.
3. Prithvirajan et al. used crystal plasticity finite element (CPFE) simulations to study crack initiation at a surface-connected pore in an additively manufactured IN718 alloy [11]. The 3D microstructure of the alloy (at the gage section of the fatigue test coupon) was extracted by overlaying the multi-modal datasets obtained from near-field high-energy X-Ray diffraction (nf-HEDM) and X-Ray computed tomography (XCT) datasets. The dataset obtained from nf-HEDM experiment consists of the 3D microstructure of the gage-section of the coupon, whereas the dataset from XCT measurement consists of the location of process-specific pores within the gage section. The high-fidelity microstructure obtained by overlaying the datasets is meshed/discretized and input into the CPFE solver to solve for the heterogeneous stress and strain fields within the high-fidelity microstructure. The location of failure predicted using the extreme values of failure metrics (plastic strain accumulation and plastic energy density) correlated one-to-one with the experimentally observed location of crack-initiation for the models.

The key to making these connections for efforts such as materials design and performance predictions are the ICME methods that greatly reduce the need for lengthy and costly experiments. Capturing physics within verified and validated computational models will still require experimentation but with fewer overall experiments and experiments that focus on revealing fundamental mechanisms instead of rote data generation. Thus, no longer is materials research largely performed with conventional experiments and simplified mathematical models, but with experimentally informed computational models that accurately capture the underlying materials physics and interactions. The mechanisms involved in the processing and structural evolution of a material from the atomistic to macroscale levels can be represented by a virtual toolbox of data-anchored – validated against experimental data and

the uncertainties in both data and model quantified – models suitable for each length scale (Figure 4). Thus, a material may be virtually evaluated first and then experimentally demonstrated.

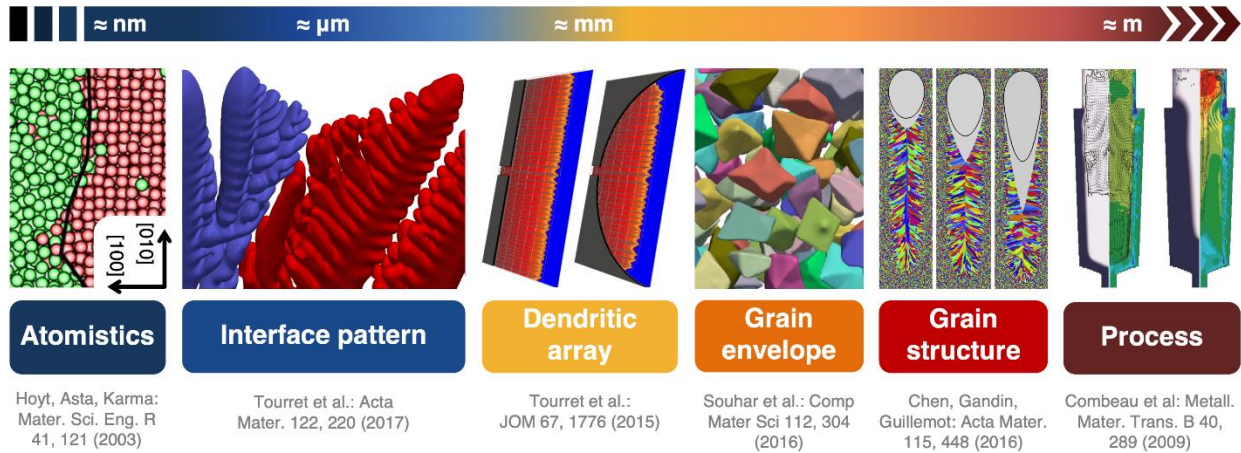


Figure 4: The continuum of computational material modeling organized by length scale [12]. Used with permission.

1.2. Microgravity materials science

With gaps in capability and validation of ICME tools, there is room for BPS to develop a niche vital to ICME using copious codes, expertise, and experimental data obtained historically and currently. The seminal 2008 report on ICME by the National Academies recognized a governmental role in ICME development and implementation as sources of unique datasets and as coordinating entities with long-term visions [13]. BPS is uniquely poised to champion and to spur progress in ICME approaches in microgravity materials science. BPS has both the datasets and the expertise to answer the questions pertinent to ICME topics such as thermophysical properties, alloy solidification morphology and kinetics, coupled fluid-solidification, and other structural evolutions such as coarsening. Throughout its history of flight experiments, BPS has consistently been a leader in atomistic to meso-scale microgravity materials research. Lacking appreciable gravitational forcing and therefore buoyancy and sedimentation within a liquid or solid-liquid mixture, flight experiments provide a clearer view of fluid-solidification coupling. The greatly reduced gravity also enables higher quality and more materials viable for containerless processing for thermophysical property measurements.

BPS historical data are housed in Physical Science Informatics (PSI) and are still relevant today to further scientific understanding. For example, a recent PSI grant re-analyzed Pore Formation and Mobility Investigation (PFMI) data housed on PSI. Two associated papers used PFMI data to validate the simulations [14], [15]. Despite these advances supported by historical data, the authors' limited computational resources only allowed a two-dimensional phase field model without fluid flow coupling. It is possible that available high-performance computing (HPC) resources at NASA, such as the Pleiades supercomputer at NASA Ames Research Center, could further help ICME investigations and allow BPS to meet the needs of researchers in this field. Beyond re-analyzing historical data, gaps in data needed to validate computational models motivate future flight experiments. However, guidance in which experiments and datasets to focus on is needed.

1.3. BPS Decadal Survey

The BPS Decadal Survey re-imagined fundamental materials science as both supporting and being supported by space exploration efforts [16]. Historically, experiments were the dominant if not the only method employed to evaluate materials and processes in space environments. However, the adoption of ICME approaches across academia, government, and industry simultaneously with burgeoning computational resources allows prediction of the response of materials to conditions unique to space [2], [17], [18]. Understanding how the unique environmental conditions in space affect the “fundamental physics controlling material structure and properties” will allow us to “better predict and control material behavior for both terrestrial and space applications” [16]. One of the most promising areas in microgravity materials science is deepening understandings of “microstructure formation during

freezing or solidification of metals and metallic alloys, with space providing the necessary long duration, purely diffusive environment” [16]. This area increasingly leverages ICME tools in a bid to “shorten development time, optimize designs and reduce costs relative to more traditional strategies involving building prototypes, testing and redesigning philosophies” [16]. **The BPS Decadal survey deemed “access to computational tools and databases” as critical to answer Key Scientific Questions** such as “What are the fundamental principles that organize the structure and functionality of materials...?” and “What principles enable identification, extraction, processing, and use of materials found in extraterrestrial environments to enable long-term, sustained human and robotic space exploration?” [16]. The routes to answer these questions are, in one form, embodied by the Manufacturing Materials and Processes for Sustainability in Space (MATRICES) research campaign, which seeks to “to understand and harness the physical processes by which materials and complex fluids can be repeatably utilized in space, to enable sustainable exploration and circular lifecycles for the built environment on Earth and in space” [16]. This aligns well with the In-Space Manufacturing and Computational Materials Roadmaps being developed by NASA’s Space Technology Mission Directorate (STMD), where ICME tools are applied to enable further space exploration by enhancing structures and our ability to repair them in space along with *in situ* resource utilization.



Figure 5: Description of the MATRICES research campaign proposed in the BPS Decadal Survey [16]

One emerging field requiring deeper understanding of physical phenomena and more mature computational tools is in-space manufacturing (ISM), which includes a large focus on rapidly solidified metal alloys in additively manufactured parts, welds, solders, etc. ISM and repair will require the development and maturation of alloy solidification processes such as welding, brazing, and additive manufacturing. Physical processes governing the thermophysical properties, solidification, and microstructural evolution of these key terrestrial manufacturing processes are poorly understood in the space environment. Indeed, this incomplete understanding limits the utility of ICME tools and hinders the transition to a sustainable in-space materials ecosystem [16]. Fluid-solidification modeling accounting for thermophysical properties and scale bridging to process modeling length scales will improve our ability to predict the complex structure-property-processing relationships of solidification processes used in space for manufacturing. This study will consider the state-of-the-art solidification and related ICME modeling for space environments, providing guidance for future efforts.

1.4. What has been done, what remains to be done, and where does BPS fit in?

BPS has access to unique datasets and unparalleled expertise in microgravity materials science after decades of innovative flight experiments [14], [19], [20], [21], [22]. NASA-managed open data repositories, such as PSI [23], provide publicly available datasets from materials science ground and flight experiments, which allows for validation of increasingly complex and realistic computational modeling and aids deeper understandings of material processing in microgravity [16]. As such, it is well positioned to continue engagement within the ICME community by, for instance, refining thermophysical and solidification simulations – especially elucidating fundamental studies under microgravity conditions where convective and sedimentary forces are negligible. To achieve this, BPS must first explore the state-of-the-art with respect to thermophysical, solidification, and additional validation dataset-relevant modeling within ICME and then identify opportunities to continue contributing to the field.

This report will address several examples BPS-relevant & BPS-supported experimental datasets and modeling efforts within the ICME ecosystem ranging from the atomistic to the mesoscale along with the application to the macroscale and eventual performance of materials systems. The unique contribution of microgravity conditions to generating useful data and models for ICME will be indicated by several examples. Engagement with the broader ICME community will be shown. Motivation for continued BPS involvement in the ICME space will be reinforced by the concept of uncertainty quantification & reduction as vital to industrial operations on Earth and in-space sustainability as noted by the MATRICES campaign. Finally, accomplishments, findings, and recommendations will be shared. This effort was, by necessity of limited labor and time, a non-exhaustive review of the state-of-the-art and potential future paths for BPS in ICME. The activities were deliberately focused on a few relatively tractable examples to illustrate how detailed future work could be conducted with an appropriately broader focus on computational and experimental techniques and are not intended to limit future ICME explorations by BPS.

First, atomistic simulations and experimental vignettes of thermophysical properties will be presented (Section 2) to demonstrate their criticality to longer length scale modeling. Then solidification flight experiments useful as validation datasets will be reviewed along with a survey of the state-of-the-art in computational modeling of micro-scale solidification processes (Section 3) via an example comparison of several academic and community codes. The required computational architecture to enable these simulations will also be discussed. Coupling of fluid flow to solidification is then reviewed and exercised using a benchmark case. Meso-scale models (Section 4) useful for scale bridging from atomistic and micro-scale to macro-scale lengths are discussed. Following, uncertainty quantification is described (Section 5) with its importance to all ICME efforts emphasized and paths to closure indicated. Finally, the report concludes (Section 6) with accomplishments, findings, and recommendations for future work.

2. Thermophysical properties

Atomic-scale thermophysical properties are foundational inputs to almost every type of computational materials simulation. Properties such as thermal conductivity, specific heat capacity, surface tension, and mass diffusivity have a critical influence during phenomena such as solidification that can lead to drastic changes in the final performance of large, bulk scale parts. As such, thermophysical properties are needed during the engineering design process, and substantial effort, cost, and time is spent determining them. However, measuring thermophysical properties with high accuracy and at a sufficient range of temperatures for engineering alloys is difficult. For computational materials simulations of engineering-relevant materials, it is crucial to characterize thermophysical properties from room temperature to beyond the melting temperature. Metallic engineering alloys typically melt at temperatures well above 1000 K and can be highly reactive. These high melting temperatures and high reactivity necessitate specialized equipment such as containerless levitation processing to measure relevant thermophysical properties. There are also additional effects that must be considered for their characterization, especially beyond the melting temperature. For example, melt pool convection due to gravity-driven effects such as buoyancy can significantly impact the measurements of the thermophysical properties. In addition to specialized experiments, atomic-scale simulations of interatomic interactions using techniques such as density functional theory (DFT), molecular dynamics (MD), and data-driven machine learning (ML) approaches provide substantial value supplementing traditional experimentation.

The engineering-design process requires accurate measurements of thermophysical properties with well understood and characterized uncertainty. There is a need for well-integrated and well-designed experiments and atomic-scale simulations to correctly characterize thermophysical properties and account for confounding factors such as gravity. Gravity itself can be used to elucidate relevant phenomena by comparing the difference between gravity-bound

ground experiments on Earth and microgravity flight experiments in space. NASA has unique experimental and simulation capabilities to support the need for accurate thermophysical property measurements. There is also value provided to on-going NASA projects with acquiring accurate thermophysical properties, particularly for materials such as aluminum, nickel, titanium, and ferrous alloys. These materials are well suited to support space exploration and provide structural components for in-use space technology that can be applied to ISM, commercial space station construction, Lunar infrastructure for Artemis, and even prolonged operations in cislunar space. Accurate thermophysical properties may enable future in-space manufacturing opportunities such as in-space welding supported by ICME efforts.

2.1. Experimental - Vignettes showcasing past BPS successes in thermophysical properties measurements and associated existing facilities

Alloy solidification is a complex process where a liquified material under cooling experiences a transition to one or several crystalline phases with a subsequent rapid structure evolution in terms of crystal nucleation and growth at elevated temperature. The system behavior is governed by the thermodynamics and kinetics of the undergoing processes. While thermodynamic forces drive and direct the transition, kinetics define the outcome depending on the cooling rate, diffusivity, viscosity, and various interface energies of the newly developed solid-liquid and solid-solid interfaces. Modeling of consolidation processes and prediction of solidification phase selection relies on having accurate thermophysical properties such as surface tension and viscosity – especially to support modeling of additive manufacturing operations. A series of vignettes is presented to illustrate the broad range of thermophysical properties that are being evaluated to support the ICME community’s efforts to understand metallic alloy solidification, grain evolution, and other property/performance relationships. Examples include titanium alloys, nickel-based superalloys, structural ferrous alloys, and selected pure elements and intermetallic compounds. Various facilities exist to conduct experiments both on the ground and in space. This section concentrates on the use of containerless levitation processing techniques to minimize contamination of the highly reactive molten samples. Key parameters that are reported from each test include recording of the time-temperature profile using non-contact radiation pyrometry and monitoring of sample reaction to an applied stimulus using either high-speed digital imaging or observation of excitation electronics control parameters. These properties are of particular importance in that fluid flow during processing has a profound impact on microstructural evolution – this includes induced flows during welding, mold filling during casting, and surface tension driven Marangoni convection during additive manufacturing. A lack of understanding of the influence of property uncertainty directly transfers into errors in the predictive capability of flow modeling and results in an inability to properly control the manufacturing process. Titanium alloys, including the commercial titanium-6wt%aluminum-4wt%vanadium (Ti64) and the intermetallic gamma titanium aluminide (γ -TiAl) compound, belong to a family of materials that are used in high temperature aerospace applications. They are lightweight and exhibit good creep behavior while being resistant to high temperature oxidation. Not only are these alloys important for in-space manufacturing applications such as repair operations on damaged or worn space hardware but they are potential candidates for on-orbit or Lunar recycling activities. As such, it is important to further understand these materials and their properties. However, it is difficult to conduct thermophysical property evaluations due to the chemical reactivity of the constituents and the potential for shifting of composition due to preferential evaporation of volatile components [24]. A key success for measurement programs in space is the evaluation of the specific heat capacity of liquid and solid phases using a technique known as modulation calorimetry [25], [26]. Modulation calorimetry involves applying a sinusoidally modulating magnetic field which causes the sample to actively heat and then passively cool. The phase lag between application of the excitation field and the thermal response of the sample allows measurement of the specific heat capacity and thermal diffusivity of solid and liquid samples. These experiments are best conducted in an ultra-high vacuum to control heat transfer, and in space to minimize energy input to the sample, using the electromagnetic levitation facility on the ISS (ISS-EML). This facility [27] can position a conductive metallic sample using a quadrupole electromagnetic field while simultaneously controlling temperature using a dipole heating field. The two fields are selected from dramatically different alternating current radio frequencies and thus the total power input to the sample can be independently selected and measured by monitoring the heater oscillating circuit current. Non-contact temperature measurement techniques are employed through use of calibrated infra-red radiation pyrometry and an example of testing results leading to analysis of measurement uncertainty in both solid and liquid phases can be seen in Figure 6 (left) [28]. Here, the red line represents a section of the time-temperature profile where the sample has been successfully melted and then cooled to an undercooled condition where the liquid exists at a

temperature below its equilibrium melting point. The blue line represents the induced thermal excitation power imposed by the heater field. After modulation is complete, the sample undercools an additional small amount and then there is a rapid temperature rise associated with the release of the heat of fusion during the formation of a metastable solid. A second rise is then seen during transformation to the stable phase. In Figure 6 (right), the specific heat for undercooled liquids and for the solid phase is shown. Of particular importance is the small measurement uncertainty shown in the data scatter.

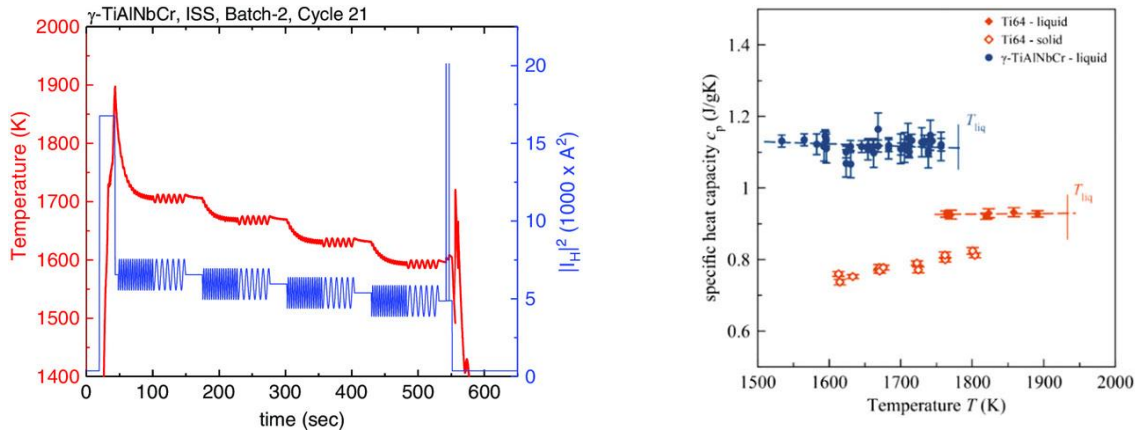


Figure 6: Specific heat measurements in space (left) thermal profile for a typical modulation calorimetry experiment using the ISS-EML facility [27]; (right) results for the specific heat of Ti-6-4 in the solid and undercooled liquid phase, as well as for γ -Ti4Al48N [28]. Figure (left) from M. Mohr and H.-J. Fecht, “[Investigating Thermophysical Properties Under Microgravity: A Review](#),” licensed under [CC BY 4.0](#) and Figure (right) from M. Mohr et al., “[Electromagnetic levitation containerless processing of metallic materials in microgravity: thermophysical properties](#),” licensed under [CC BY 4.0](#).

Measurement of properties of structural alloys used in aerospace applications often is complicated by the complex multicomponent nature of commercial alloy formulations. For example, the nickel-based Inconel superalloys have chemical specifications that control over ten elements; ferrochromium-based stainless steels often have up to nine elemental constituents. In both cases, the composition is specified as a limited range of each element in solution. Conducting measurements over the entire span of the range of possible compositions is economically infeasible. Thus, it is essential that ICME techniques are utilized. The approach employed is to conduct ground-based experiments, allowing rapid investigation of multiple samples to bound behavior, and then progress to space processing, to validate performance and quantify uncertainty for select compositions. By conducting multiple experiments over a range of temperatures, investigation of properties as a function of temperature and phase may be accomplished. Atomistic computational techniques can guide this experimentation as discussed in the following subsection.

Nickel-based superalloys are heat-resistant materials used in the fabrication of turbomachinery and aerospace structural elements. They retain superior properties at high temperatures and are under investigation for use in the production of transformative propulsion technology components using additive manufacturing techniques. In this capacity, preferential evaporation of volatile components from the melt pool is of high importance. Evaporation can be modeled using the Langmuir equation, but key thermophysical properties such as species-specific chemical activity and surface segregation must be known as a function of temperature to accurately predict preferential evaporation. Computational thermodynamic calculations may be accomplished with commercial software such as Thermo-Calc, but these predictions need to be validated through experimentation [24].

There is a need for both ground-based and space-based containerless processing facilities that use levitation. On ground, the weight of the sample must be counteracted, and metal alloy testing is typically accomplished in vacuum to prevent arcing - thus maximizing evaporation. In space, because gravity does not need to be countered, the field strength can be reduced, and testing can be accomplished using a protective inert gas shielding environment - thus minimizing evaporation. The combination of these two extremes provides experimenters with a powerful comparative perspective on system behavior.

Ground-based testing can be accomplished at the NASA Marshall Space Flight Center using the electrostatic levitator (MSFC-ESL). Electrostatic levitation (ESL) uses Coulomb forces acting on an electrically charged sample to levitate it between two electrodes [29]. The electrostatic field is generated by six electrodes, which are positioned in pairs along three mutually orthogonal lines. This geometry provides an unobstructed view of the levitated sample

from all directions in the horizontal plane of the sample. Heating is typically done by a laser, which decouples the heating from the position control. For metallic samples, the environment is high vacuum, and the system can also be run pressurized, which is useful for glass and ceramic samples. The environment of the ESL chamber can either be high vacuum or gaseous provided that the gas can withstand the electric field. The breakdown voltage is the voltage necessary for an electric arc to form between two electrodes in a gas - as a function of pressure and gap length. Arcing needs to be avoided, because it causes the sample to drop out of levitation and it can damage system hardware.

An example of telemetry from space testing using the JAXA Electrostatic Levitation Furnace (ELF) facility is shown in Figure 7. In the first part of the figure, the live video feed for monitoring levitation stability and facility health is seen; the glowing molten sample is easily seen positioned between the top and bottom electrodes. In the second, there are three graphs showing, respectively, the raw oscillation amplitude during excitation, a plot of the filtered signal showing viscous damping where the decay constant is used to evaluate sample viscosity, and a Fourier transform used to identify the frequency spectrum obtained from sample response to external stimulation for surface tension analysis. In the third part of the figure, high-speed digital imaging is used to record a projected image of the sample for density and thermal expansion measurement. Finally, the location of the pyrometer target is shown on the sample surface in conjunction with a display of sample processing time.

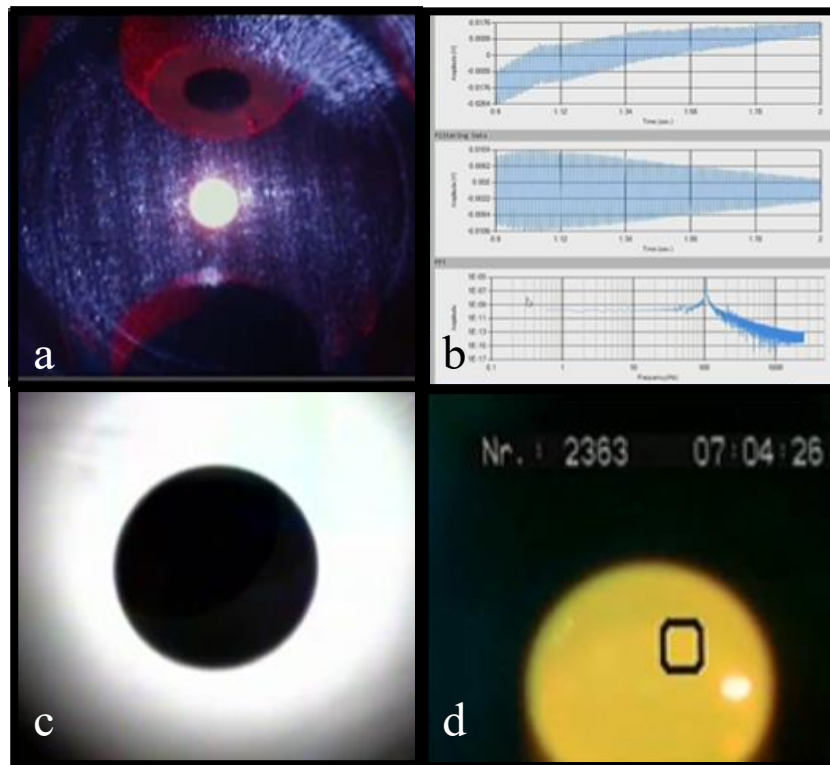


Figure 7: Electrostatic Levitation processing in space using the JAXA ELF facility (a) real-time video, (b) sample oscillation excitation, (c) high-speed digital video, and (d) image of the location of temperature measurement.

Given that future transformational ground-based industrial and space manufacturing processes will rely on the development of new alloy systems, one powerful technique used in alloy design is to bound the compositional space with a series of analog alloys – compositions which contain a reduced set of alloying elements to define the influence of specific minor constituents. ICME techniques can then be used to predict behavior of any mixture at any composition within the family. After conducting extensive ground-based experiments using the MSFC-ESL at a variety of temperatures and at different compositions, on-orbit tests are used to validate results using the ISS-EML electromagnetic levitation facility and the space-based ELF [30].

In a similar manner, commercial ferrous alloys, with their complex mixture of multiple elemental constituents, and ferrous analogs are tested to support ICME modeling of behavior. Since the stainless steel family of alloys contains a significant quantity of chromium, they are highly reactive and require containerless levitation processing methods.

In addition to evaluation of thermophysical properties, testing of phase selection and transformation kinetics may be accomplished for use in developing isothermal time-temperature transformation (TTT) and continuous cooling transformation (CCT) diagrams used to control microstructural evolution and subsequent mechanical properties or limit development of defect structures. Behavior under far-from-equilibrium conditions may be investigated in a unique manner – using convection as a controlled experimental parameter. For example, during rapid solidification a metastable ferrite phase can form with subsequent transformation to the stable austenite. While investigating the kinetics of this transformation on a sample in microgravity, the thermophysical properties of that same sample may be measured simultaneously [31]. With the knowledge of the properties at the time of the test, magnetohydrodynamic modeling [32] can be used to predict sample stirring in order to accurately predict the dynamic changes in induced sample convection during the actual test as a function of time [33]. This approach avoids the problem of using generic values and introducing significant errors in predicting flow and its effect on solidification microstructural evolution.

An important aspect of ICME is the need to quantify uncertainty in measurement accuracy (how close a value comes to the true value) and precision (evaluation of the reproducibility, or measurement scatter, of the results). Pure elements such as zirconium [34], an important material for development of space nuclear propulsion, are tested on ground and in space to provide a benchmark dataset for validation of analysis techniques and modeling activities. Binary systems are tested in order to support validation of computational thermodynamics predictions of functions such as excess volume in the prediction of density [35] and excess free energy in the prediction of surface tension [36].

These vignettes illustrate how thermophysical property experimentation is used to address several of the key themes identified in the Decadal Survey. First, modeling of far-from-equilibrium behavior such as process control during rapid solidification from an undercooled liquid often require an understanding of metastable phase thermophysical properties which are best evaluated using containerless levitation techniques. Second, benchmark solidification and phase selection experiments can be run to anchor subsequent computational solidification modeling; in parallel with these experiments the thermophysical property measurements of that sample at that time can be measured to select the level of convection as a controlled experimental parameter. Third, with the potential for developing simplified analog systems, investigations may focus on the contribution of minor alloying species in solution within the complex multi-component commercial alloy and enable use of computational thermophysical property predictions across a wide range of compositions without the need for a protracted experimental program. The approach employed is a progression from ground testing to space testing. On ground, multiple tests may be conducted over a wide range of compositions and test conditions to leverage the ability to achieve high turnaround while accepting the potential for gravity-interference and the associated measurement uncertainty. Then space testing is used to validate the results with a selected few high-fidelity microgravity experiments to anchor predictions from computational simulations.

2.2. Computational thermophysical properties

Modeling thermophysical properties and their interrelations is not always possible at continuum level as they could be strongly affected by the discrete atomistic nature of the materials. Theoretically, thermodynamics and kinetics of large atomic system are well understood, but practical calculations for a specific alloy system are still challenging mostly due to the complex interatomic force fields, governed by quantum mechanics, and the limited time and size scales accessible in these calculations. What follows is an explanation of several computational techniques that may be used to predict thermophysical properties, which can be anchored to validation datasets collected using the facilities and methods of the previous subsection.

Multiscale approaches help bridge the time and size scale gaps between modeling and experiment. Capturing quantum mechanics complexity in feasible computations requires different approaches as quantum fields have been found to be too complex to approximate satisfactorily with analytical semiempirical relations, such as the embedded atom method (EAM) force field [37], [38], that are suitable for fast computations. Instead, machine learning methods are becoming more widespread in representing atomic force fields that can closely follow quantum mechanics-based calculations [39], [40], [41], [42]. At NASA Langley Research Center (NASA/LaRC), in collaboration with George Mason University, a novel machine-learning force field method has been developed and successfully tested. The approach is based on the so called physically informed neural network (PINN) [43] interatomic potential. In this approach, a neural network is extensively trained on a sufficiently large atomistic database solved by the quantum mechanics-based density functional theory (DFT) method. The trained neural

network is used to accurately tune the parameters of a selected functional form, which represents different aspects of the interatomic behavior, such as the nucleus repulsion and chemical bond formation. The resultant interatomic potential, tested on a pure aluminum system, was found to reproduce very closely both, the solid-state crystalline material properties, such as elastic constants, phonon spectrum, various types of defect energies, as well as the melt's thermophysical properties, such as melting temperature, density, diffusivity, viscosity, and surface tension. Figure 8 shows comparison of predicted properties versus those experimentally measured, indicating relative agreement between PINN and experiment compared with much poorer agreement for a conventional EAM potential.

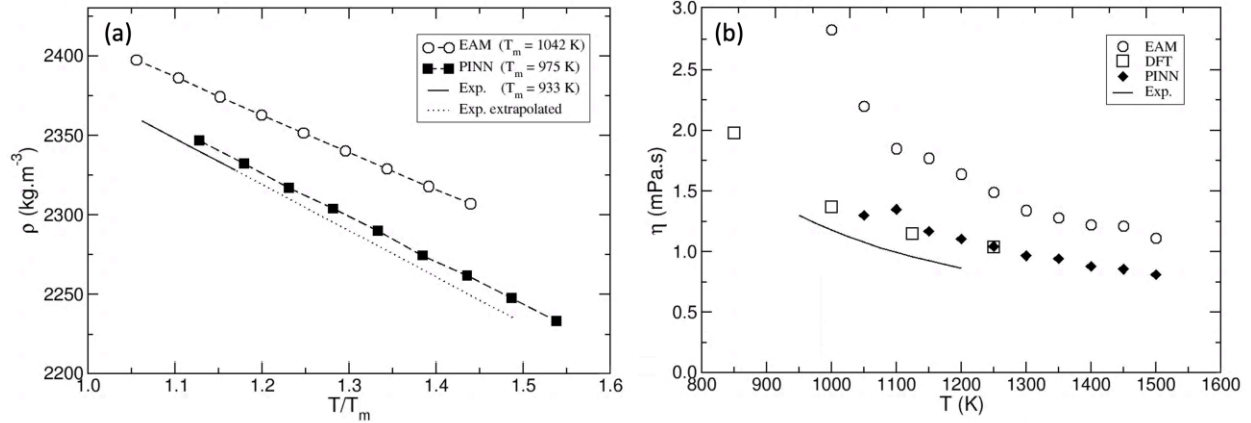


Figure 8: (a) PINN calculated melt density at a range of temperatures above the melting point, T_m , compared to experimental data, and with a semi-empirical potential based on the embedded atom method (EAM); (b) PINN calculated melt viscosity compared to experimental, DFT, and EAM data [43]. Used with permission.

The close overlap between the PINN and the DFT values on Figure 8 demonstrates the efficiency of the DFT training of the neural network. In addition, the PINN derived potential allowed the calculation of the energy of the liquid-solid interface, which has never been measured experimentally or calculated through the DFT method. Precise estimation of the melt properties through molecular dynamics, based on a neural network machine learning potential, allows for their use in a PF model of solidification at grain scale in a hierarchical multiscale approach. The described above approach reduces the need of highly computationally expensive and time-consuming DFT calculations to only calculating the energies of a prebuilt training database of atomic structures of limited size of no more than few hundred atoms each. After this database is used to develop an accurate PINN force field, classical MD simulations can replace *ab-initio* MD simulations without a noticeable loss of accuracy (of less than 5 meV per atom potential energy). A comparison between a DFT-MD and a classical MD using both PINN and EAM force fields, given on Figure 9, shows that the ML-based PINN force field, while being 150 times slower than the semiempirical EAM force field is much faster than the DFT-MD, which becomes impractical to use for systems of more than few hundred atoms. While there is still a need for a large amount of DFT calculations to create the training database, containing tens of thousands of atomic clusters and crystal structures, this is a one-time effort. After that classical MD and atomistic MC simulations can be used to predict the thermophysical properties of materials in solid and liquid state using advances statistical mechanics and thermodynamic integration methods on large systems (of 10^4 to 10^6 atoms) unachievable by DFT, but essential in modeling highly disordered systems, such as alloy melt, liquid-solid interfaces, phase-boundaries and grain-boundaries formed during solidification in multicomponent alloy systems. Apart from training ML-based force fields, DFT calculations could be restricted only to calculating properties unobtainable by classical MD methods, such as electronic properties and bandgaps.

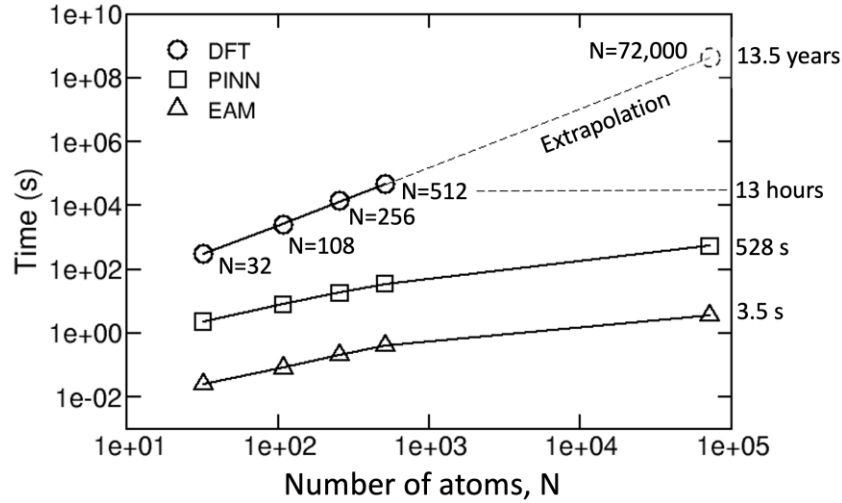


Figure 9: Time comparison between DFT, PINN, and EAM MD simulations on a single crystal of aluminum performing 100 integration steps. The DFT was used for up to 512 atoms and extrapolated for 72,000 atoms.

In atomistic simulations, using either DFT-MD or classical MD, estimating melt properties requires special techniques based on statistical mechanics and thermodynamics. For example, obtaining the melting temperature of a material requires finding the system state where the two phase, liquid and solid, coexist in thermodynamic equilibrium (Figure 10). This requires performing either a series of simulations at various temperatures to get the temperature where the interface boundary is stationary or simulating the system under the so-called constant enthalpy thermodynamic ensemble, where the enthalpy of the system is fixed, and the system acquires by its own the temperature where the two phases are in equilibrium. The later method resembles putting a cube of ice in an isolated thermos full of water and measuring the temperature approaching 0°C as the ice melts.

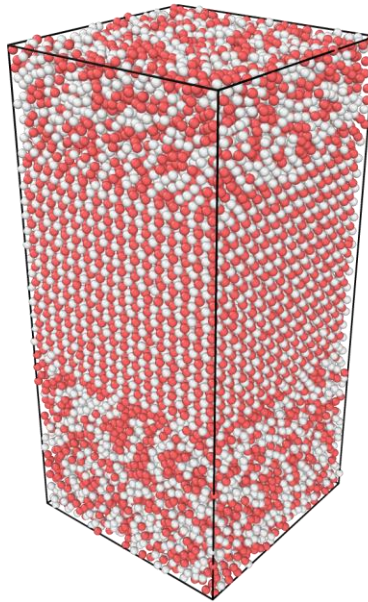


Figure 10: Molecular dynamics simulation of crystal-liquid interface for γ -TiAl.

Finding the excess free energy of the liquid-solid interface, or the liquid-vacuum interface (equivalent to the surface tension of the liquid) is best done by the capillary fluctuation method (CFM) [43], [44], [45], [46], [47]. The CFM is an accurate method to compute the weak anisotropy of the interface free-energy (same 4 refs) that plays a crucial role in dendritic microstructure formation and is a key input parameter in PF simulations (corresponding to ϵ_4 in Table 1 of Section 3.2). In this method, one uses the capillary fluctuations of the interface position during a sufficiently long simulation under equilibrium conditions. The power spectrum of these fluctuations, obtained

through a Fourier transform for different crystal orientations, can be related through the equipartition theorem of statistical mechanics to the interface free-energy for each orientation, thereby enabling to calculate both its magnitude and anisotropy. The CFM can also be successfully applied to grain boundaries where experimental measurements are notoriously difficult [48]. By use of the fluctuation-dissipation theorem, the CFM can also be used to extract non-equilibrium properties of interfaces such as the atomic attachment kinetics coefficient for solid-liquid interfaces, which influences microstructure formation at high solidification rate (Hoyt et al 2003 in 4 refs above) or the grain-boundary mobility (Karma et al, PRL 2012). The same fluctuation-dissipation theorem is also used to estimate viscosity of the melt by using the fluctuations of the stress tensor (or the internal pressure variations) of the liquid in equilibrium at a given temperature. One code, for instance, is the combined molecular-dynamics Monte Carlo code, ParaGrandMC, developed at NASA/LaRC [49]. Exquisitely understanding and modeling these interfaces will be vital to proper ICME workflows of processes involving tightly coupled interactions between various phases, such as additive manufacturing and welding especially in the keyholing regime that involves gas-liquid-solid interactions and in the vacuum of the space environment. Employing the CALPHAD method, Thermo-Calc is another ICME tool that can predict thermodynamic parameters relevant to solidification; its DICTRA module can predict solute rejection and segregation effects [50], [51]. The PRISMA component of Thermo-Calc can also use Kampmann-Wagner Numerical (KWN) models to predict precipitate kinetics [52]. A challenge in using PF methods in ICME is that most alloys of engineering importance are multicomponent. Thus, it is necessary to couple PF methods to CALPHAD databases. While the multi-order parameter approach is designed to accommodate multicomponent alloys, the challenge is to determine the virtual compositions at all points in the system. This requires many calls to a CALPHAD database that are needed to determine the free energies and chemical potentials, as well as solving a nonlinear set of equations at each mesh point. This remains a challenge for widely available community-based CALPHAD codes such as pycalphad. The advantage of CALPHAD is that a more readily accessible database can be called to instead of a more computationally intensive and complex atomistic simulation, thus demonstrating scale bridging between atomistic and micro-scale solidification.

2.3. Future

Experimental

To support the future needs of the ICME community, ground-based and space testing facilities will be needed to continue the ongoing work to establish benchmark experimental verification of process modeling and computational prediction of how thermophysical properties vary with temperature and composition. It is not feasible to test all possible alloying element combinations and ICME techniques will be required to fill in the knowledge gaps and guide selection of profitable future research activities. Since the systems of interest are often highly reactive and sensitive to oxidation, containerless levitation techniques will need to be employed.

To validate computational thermodynamic predictions for both liquid and solid complex multi-component alloy systems using computational thermodynamics tools, a two-step approach is envisioned. First, a series of experiments are run on simplified analog alloy systems to define binary and then ternary interactions. Once model inputs are defined, the thermodynamic predictions can be refined and used to predict multi-component behavior. Second, experiments can be run on a limited series of commercial multicomponent mixtures to validate predictions and quantify uncertainty. These results can then be employed to simulate real-world processes based on results of benchmark microgravity demonstrations.

Supporting these testing activities requires access to a variety of experimental platforms. Ground-based facilities allow rapid screening of behavior. Space facilities enable researchers to eliminate the confounding impact of gravity-driven phenomena. ESL techniques can decouple the electrostatic positioning and laser heating of a sample. Thus, processing can be accomplished on quiescent liquids. They also have the added advantage of being able to process non-conductive materials, including oxides and ceramics, thus expanding the envelope of materials that may be investigated. Levitation using EML techniques involves application of a dynamic magnetic field which induces some limited amount of liquid flow. A major advantage of this technique is the ability to independently apply simultaneous heater-induced flows to allow investigation of the influence of convection on solidification phenomena. Together, these two techniques enable investigations spanning the range of behavior across the laminar to turbulent regimes. These techniques are particularly attractive in that current investigations on – for example – light-weight titanium alloys, structural nickel-based superalloys, steels, metallic glasses, and novel high entropy

alloys have shown that researchers are able to evaluate properties for deeply undercooled molten metal alloys and properties of metastable phases to allow modeling of far-from-equilibrium conditions.

Computational

Computational resources required to perform PINN development for simulating multicomponent alloy systems will still be substantial despite lower than conventional techniques. This includes DFT calculations on the order of 10^5 atomic configurations containing between 2 and 200 atoms, training the ML-based PINN force field, and using it to predict the thermophysical material properties. This would likely be a multi-year effort.

2.4. BPS role in future

Historical datasets

Historical thermophysical property measurement datasets may be useful not only to provide validation data for traditional, deterministic ICME tools but also to provide training data for ML-based models like PINN. Thus, the investment in open-science repositories such as PSI is vital.

Support existing ground and flight facilities

Existing ground and flight facilities are still producing critical data on thermophysical properties needed for ICME tools, so their continued support will continue providing valuable validation datasets and will also bridge the gap to future flight facilities.

Advocate for new flight facilities on commercial LEO destinations

With the impending close-out of science on the ISS and decommissioning of its containerless processing facilities – ISS-EML and ELF – there will be no permanent facilities to perform thermophysical property measurements in the high-quality microgravity environment of space. To provide benchmark data for thermophysical properties modeling efforts and to support uncertainty reduction in longer length scale models by reducing that uncertainty inherent in thermophysical property data, permanent facilities for containerless processing in space should be design, developed, fabricated, and manifested for post-ISS space station. For instance, commercial LEO destinations (CLDs) would be suitable platforms for evolved versions of the ISS-EML or ELF, perhaps with enhancements or improvements learned over their decades of productive operations on the ISS.

Invest in HECC via SMD allocations to support PINN/DFT of thermophysical properties

Advancing the high-end computing of thermophysical properties will require sustained efforts over several years with at least a small, focused team consisting of ideally postdoctoral scholars and established technical experts. A substantial allotment of compute time on a supercomputer would be required. If one were to use the NASA Advanced Supercomputing (NAS) resources at NASA Ames Research Center, this would approach 400,000 Standard Billing Units (SBU) per year. These are rough estimates to give a sense of the scale and investment required.

3. Solidification & fluids

Solidification processes in metal alloys are highly relevant to both in-space sustainability efforts encompassed by the MATRICES campaign and to industrial manufacturing on Earth. However, even with fully determined thermophysical properties, modeling microstructures formed on the part scale remains extremely challenging due to the geometrically complex evolution of the solid-liquid interface shape during the solidification process. This evolution is controlled by a delicate balance between the stabilizing effect of surface tension and the destabilizing effect of solute transport in the liquid. This modeling challenge is compounded by the large disparity of length scales associated with these competing effects, from surface tension acting on the nanometer width of the solid-liquid

interface to solute transport taking place on the diffusion length $\sim D/V$ (where D is the solute diffusivity in the liquid and V is the solidification rate), which varies from ten to hundred microns for typical low solidification rates. Overcoming this challenge is a central goal of ICME to accurately predict PSP/P. As noted in the BPS Decadal Survey, NASA has unique infrastructure to cope with this challenge by generating benchmark data sets that can serve to validate ICME tools while, at the same time, dissecting the effects of gravity-driven fluid flow and surface-tension-driven fluid flow that persists in a microgravity environment in the presence of free surfaces.

BPS has already supported several flight experiments that have generated important datasets, from historical flights such as IDGE that focused on the dendrite tip operating state to more recent flight experiments (such as DECLIC, CETSOL, and PFMI) studying larger-scale dendritic array and grain structures more directly relevant to PSP/P prediction. While existing data sets have already played a key role in helping to validate ICME computational tools, they span a very limited set of binary alloys, growth conditions, and geometries. Therefore, there is a critical need for future experiments that investigate both, the same alloys (with already well-characterized thermophysical properties) under a broader range of conditions and geometries, and that investigate both binary and more complex alloys under rapid solidification conditions relevant for additive manufacturing. In addition, while ICME tool development and validation for alloy solidification has advanced considerably, it is still in relative infancy in comparison to CFD. For example, while PF tools have often been used in microgravity solidification simulations [14], [22], [53], a 3D open-source code to model directional solidification flight experiments (such as DECLIC, CETSOL, or PFMI) has just become available. Moreover, the predictions of this open-source code are compared quantitatively to a well-developed academic research code for the first time as part of the present study (cf., Section 3.b). In parallel to making codes more broadly available, further work is also needed to extend PF code capability to larger length and time scales in a purely diffusive growth regime, to couple interface dynamics to fluid flow, and to bridge PF predictions to more coarse-grained approaches such as cellular automaton and the dendritic needle network to make predictions on the part scale [54].

Importantly, ICME computational tools can now model more practically relevant transient growth conditions that require shorter flight experiments in comparison to historical studies that focused on testing analytical theories limited to steady-state growth conditions. This creates a positive iterative feedback loop in which computational models can help design shorter flight experiments that can in turn serve to validate the predictions of these models and improve their accuracy.

3.1. Experimental

Historical flight datasets

Dendritic growth patterns and solidification kinetics can be evaluated in pure substances where compositional differences are negligible, simplifying the analysis. These are benchmark experiments, where the experimental space is purposely reduced to focus on investigating a particular mechanism in detail while reducing confounders. A series of landmark flight experiments, the Isothermal Dendritic Growth Experiment (IDGE), studied pure succinonitrile (SCN) and pivalic acid (PVA) dendritic evolution aboard Shuttle flights in the 1990s and on early ISS expeditions [55], [56]. These optically transparent organic materials allowed *in situ* imaging of dendrite tip velocity (Figure 11) for conditions representative of ferrous and non-ferrous alloys, respectively. It is apparent how the microgravity condition more closely tracks the ideal, theoretic case – especially for low supercooling (proxy for solidification rate) and tip velocity – than the ground condition. Ostensibly, the reduction in gravity-driven buoyant and sedimentation convective flows leads to a sufficiently quiescent environment where the underlying principles of slower solidification can be investigated less the confounding influence of gravity. IDGE gives a basis for understanding the complexity of previous computational benchmark cases.

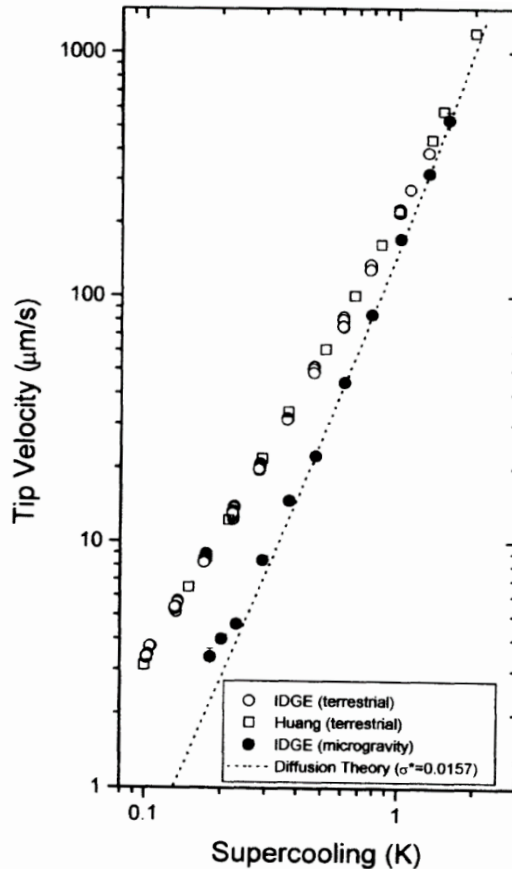


Figure 11: SCN dendrite tip velocity by supercooling in terrestrial and microgravity conditions [55]. Used with permission from M. E. Glicksman, M. B. Koss, L. T. Bushnell, J. C. Lacombe, and E. A. Winsa, "Dendritic Growth in Terrestrial and Microgravity Conditions," *MRS Proc.*, vol. 367, p. 13, 1994, Springer Nature, doi: [10.1557/PROC-367-13](https://doi.org/10.1557/PROC-367-13).

Previous computational benchmarks can be used to assess the accuracy and efficiency of publicly available codes to simulate the dendritic solidification of a pure substance [57], [58], [59], [60]. For example, a quantitative PF approach for pure substances employed the thin-interface limit [58]. This analysis enables quantitative simulations of the experimentally relevant limit of local thermodynamic equilibrium at the solid-liquid interface (*i.e.* negligible kinetic undercooling) with a computationally tractable width of the spatially diffuse solid-liquid interface region. This study contains both 2D and 3D steady-state growth results for the dendrite tip operating state and tip shapes. The dimensionless undercooling range is typically larger than the range studied experimentally in IDGE, but the benchmark results can be used to test 2D and 3D dendritic growth simulations. A second set of benchmarks [57], [59] modeled the transient growth regime of equiaxed growth in 3D – specially, the case when primary branches emerge from a crystal seed but have not yet reached a steady-state growth regime where the tip velocity and tip radius are constant. In this transient growth regime, the tip velocity and tip radius follow power laws in time and the interface shape also follows a scaling law. The undercooling range can overlap with that of IDGE experiments and can also be used to test modeling codes in the transient regime. A third set of benchmarks provides results for steady-state growth over an undercooling range corresponding to the upper range of IDGE experiments and provides a detailed characterization of the non-axisymmetric 3D dendrite tip shape that can also be used to benchmark dendritic growth simulations in a steady-state growth regime [60]. These will give initial indications of the capabilities and V&V of a code.

Modern benchmark cases using flight experimental data

Several recent flight experiments have datasets and processing parameters suitable for use as benchmark cases to test various ICME tools, especially the PF approach. One such flight experiment, DEvice for the study of Critical

Liquids and Crystallization - Directional Solidification Insert (DECLIC-DSI), used a transparent organic alloy analogue of SCN-0.46wt% camphor to study directional solidification, specifically dendrite spacing and local drift, under microgravity conditions [21]. Pulling velocity is varied to study how interface curvature affects primary dendrite spacing, local drift, and invasion by stray grains during the experiment. A 3D PF research code was used to simulate primary dendrite spacing, drifting, and pattern evolution over time using temperature, curvature, and composition as inputs [61]. Figure 12 summarizes these results.

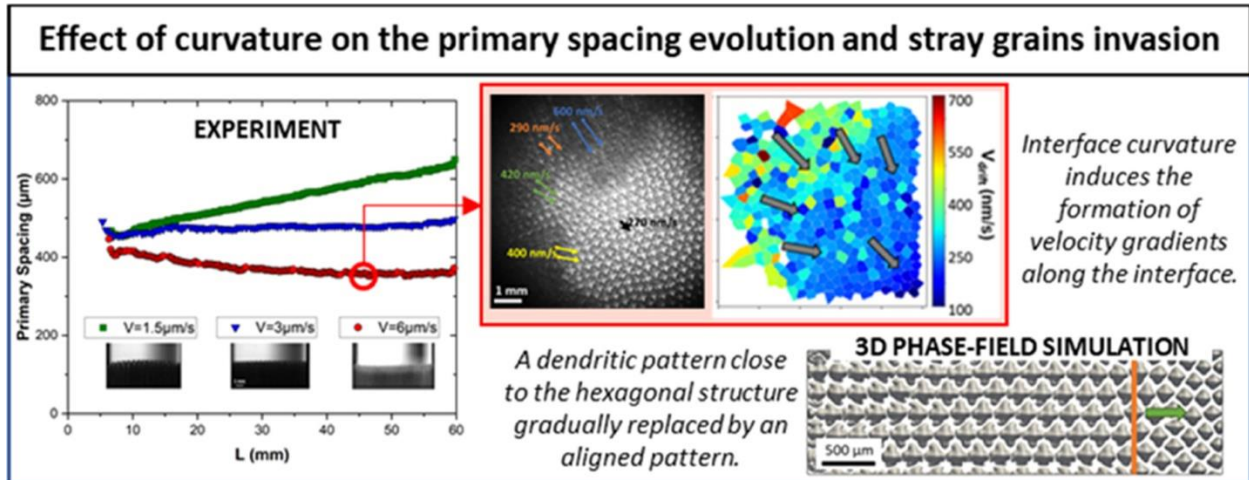


Figure 12: Graphical abstract of a combined experimental and PF simulation study of SCN-camphor dendritic solidification under microgravity [61]. Figure from F. L. Mota, K. Ji, L. S. Little, R. Trivedi, A. Karma, and N. Bergeon, "[Influence of macroscopic interface curvature on dendritic patterns during directional solidification of bulk samples: Experimental and phase-field studies.](#)" licensed under [CC BY-NC-ND 4.0](#).

The ongoing international NASA-ESA collaboration in the framework of the Columnar-to-Equiaxed Transition in Alloy Solidification (CETSOL) project has produced several benchmark datasets for modeling the ubiquitous transition from columnar to equiaxed grain structures, which is of well-recognized practical importance for controlling the mechanical behavior of structural alloys produced by a wide range of solidification processes. An example dataset in aluminum-(4,10,18)wt% copper was obtained in microgravity by the (SUBSA-CETSOL) experiment Effect of Convection on the Columnar-to-Equiaxed Transition in Alloy Solidification. The solidified microstructure has been correlated to the experimental thermal history for ground and flight-based samples with a CET obtained only in the ground based samples for the conditions attained [20]. Grain structure (Figure 13), eutectic fraction, and macrosegregation were all reported as a function of gravitational forcing and associated thermal profile. This case is important for scale bridging as the overall grain structure can be analyzed at a larger scale than individual dendrites.

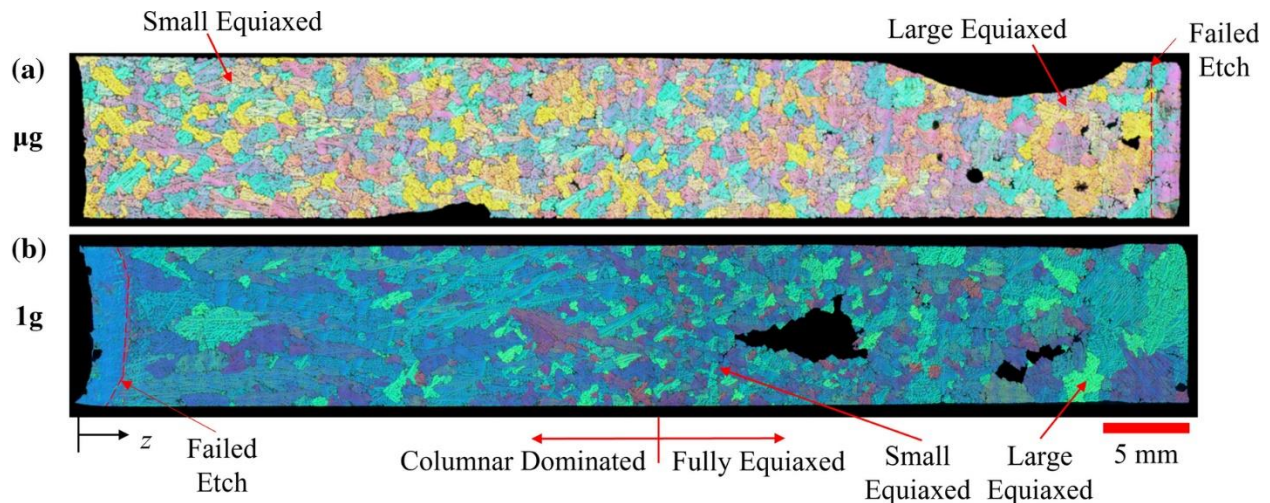


Figure 13: Optical micrographs of etched aluminum-4wt%Cu specimens solidified under a) microgravity and b) 1 g in SUBSA-CETSOL [20]. Used with permission from T. J. Williams and C. Beckermann, "Benchmark Al-Cu Solidification Experiments in Microgravity and on Earth," *Metall Mater Trans A*, vol. 54, no. 2, pp. 405–422, Feb. 2023, Springer Nature, doi: [10.1007/s11661-022-06909-6](https://doi.org/10.1007/s11661-022-06909-6).

Resolving dendritic microstructures within individual grains is currently at the limit of the computational capability of the PF method in 3D for dilute binary alloys [61]. As a result, scale-bridging computational strategies based on cellular automata (CA) [62], [63], dendritic needle network (DNN) [64], [65], [66], [67], or other mesoscale methods are needed to resolve dendritic microstructures within individual grains in concentrated alloys as well as to resolve the large scale multi-grain structure in both dilute and concentrated alloys. Both DNN [66] and CA [63] approaches have already been used to predict grain structures in a related set of CETSOL directional experiments in the MSL aboard the ISS, which used aluminum-7wt%Si alloys without and with grain refiners [68]. Those approaches have proven successful in predicting basic characteristics of grain structures such as grain size and elongation factor and the character of the columnar-to-equiaxed transition (CET), whether abrupt or progressive. However, they need to be further validated by comparison with more recent MSL CETSOL data sets in aluminum-copper alloys. In addition, recent studies have highlighted the need of selecting the cell size in CA simulations based on the results of PF simulations to correctly resolve the growth competition of dendritic grains and the large-scale grain structure [69], [70]. The rich variety of CETSOL experimental data sets in metallic aluminum-Si and aluminum-Cu alloys and transparent Neopentyl Glycol (NPG)-D-Camphor (DC) alloys [71], [72] (Figure 14) provide a valuable resource for validating the predictions of ongoing computational studies using PF, CA, and DNN methods.

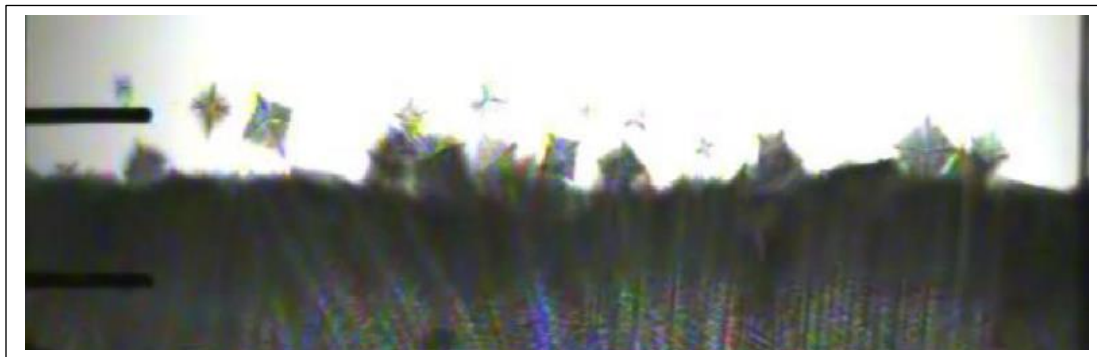


Figure 14: Experimental observation of the CET from the low-gravity experiment "TRACE" (TRANSPARENT Alloys in Columnar and Equiaxed Solidification) for a transparent organic model system Neopentylglycol (NPG)-37.5 wt.-%(d)Camphor (DC), executed on the sounding rocket mission TEXUS-47 in 2009 with about 7 minutes of low-gravity time [72]. Figure from L. Sturz, M. Wu, G. Zimmermann, A. Ludwig, and M. Ahmadein, "Benchmark experiments and numerical modelling of the columnar-equiaxed dendritic growth in the transparent alloy Neopentylglycol-(d)Camphor" licensed under CC BY 3.0.

The fragmentation of dendrites also has important consequences during the solidification of alloys. These fragments can be transported by convection ahead of the tips of columnar dendrites into the undercooled liquid region, and form equiaxed grains (CET). Dendrite fragments can lead also to misoriented grains (freckles) within the columnar region, an important casting defect in single crystal turbine blades, and result in equiaxed grains, and thus more homogeneous mechanical properties, during additive manufacturing. The fragmentation process has been studied under isothermal conditions in the microgravity environment, thus ensuring that the fragmentation process is driven solely by interfacial curvature. The experiments were performed using a binary Pb-Sn alloy on the ISS as part of the Coarsening in Solid-Liquid Mixtures (CSLM) experiment [22]. The Pb-Sn alloy system is ideal since the interfacial energy and solute diffusion coefficient have been measured accurately, and thus quantitative comparison between PF computations and experiment are possible. To determine the fragmentation rate, three-dimensional reconstructions of the microstructure were employed. These three-dimensional reconstructions provide unambiguous initial conditions for calculations of the evolution of the dendritic two-phase mixtures, see Figure 15. In this case the Echebarria et al., 2004 [73] PF model was employed. Reasonable agreement between simulation and experiments were obtained. However, since the Pb-Sn alloys are not dilute solutions, the role of non-dilute non-ideal thermodynamics remains to be investigated.

PF calculations of the evolution of these structures can be challenging. They must be performed in three dimensions, since an important fragmentation mechanism, the Rayleigh instability, does not occur in two dimensions. Moreover, the representative volumes used in the calculations must be sufficiently large to reduce the influence of boundary conditions. However, since the evolution of the structure is driven by composition gradients in the liquid induced by interfacial energy, the velocities of the solid-liquid interfaces are typically slow, and thus the computationally time-consuming interface anti-trapping term is not needed for coarsening simulations [74].

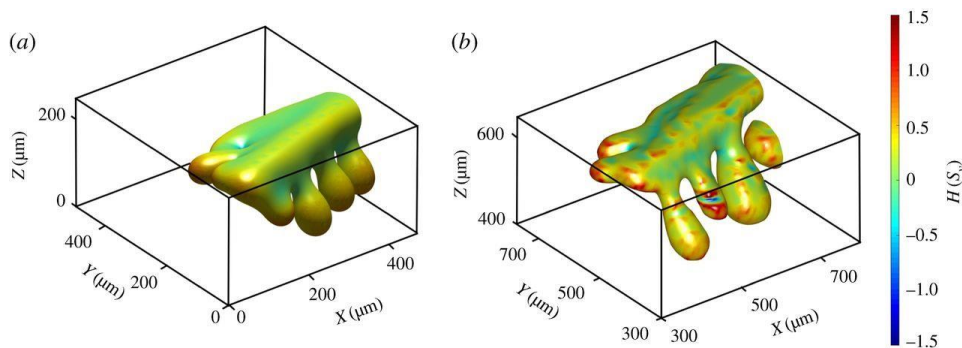


Figure 15: Dendritic structure after 1.6 hours of coarsening seen a) as simulated and b) as measured experimentally.

Another potential dataset comes from the Pore Formation and Mobility Investigation (PFMI) flight experiment, which investigated dendritic growth and solidification in the microgravity environment of the ISS. A SCN-0.24wt% water binary alloy analogue was remelted and then allowed to re-solidify with negligible convective forcing. Since the alloy is transparent, direct visualization of the solidification process is possible. A key feature of this experiment was intentional injection of nitrogen bubbles into the sample tube, to investigate the influence of such defect sources on the resulting solidified microstructure. Examination of video recordings of the solidification process has shown clear indication of small ‘tracer’ bubble movement due to Marangoni-driven convection within the liquid alloy, which is still active in a microgravity environment and becomes dominant in the absence of buoyancy-driven convection. Video recordings have also revealed the appearance of larger bubbles pinned to the solidifying dendrites and movement of dendrite fragments within the melt. Although direct observation of such convection was not possible in the microstructure formation in casting (MICAST) microgravity experiments, misoriented “spurious” grains and surface pores resulting from the sample detaching from the tube have been observed. Recently, publicly available data from PFMI was analyzed and simulated via CA and PF models [14]. Experimental findings on dendrite morphological evolution and tip velocity were compared against the same from simulations, which are shown in Figure 16.

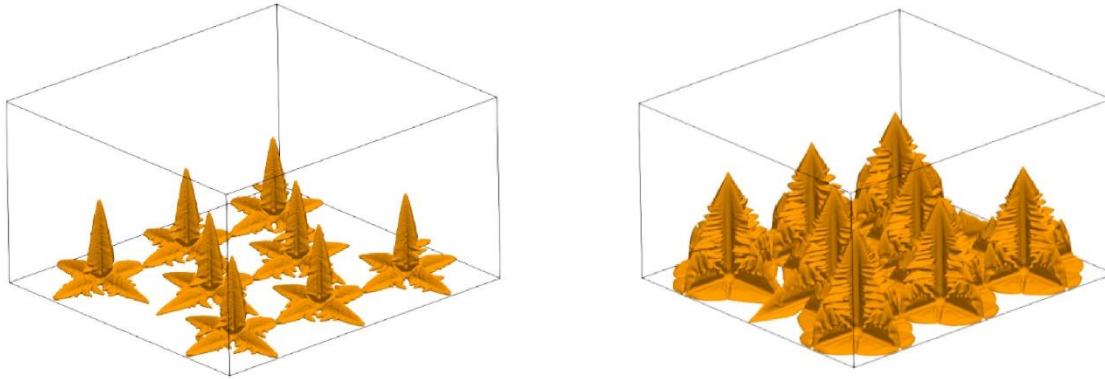


Figure 16: Dendrite evolution of SCN-0.24wt%water in microgravity simulated at the same time step by CA (left) and PF (right) models [14]. Figure from S. A. Nabavizadeh, R. Lenart, M. Eshraghi, S. D. Felicelli, S. N. Tewari, and R. N. Grugel, “[Dendritic solidification of Succinonitrile-0.24 wt% water alloy: A comparison with microgravity experiments for validating dendrite tip velocity](#)” licensed under [CC BY-NC-ND 4.0](#).

With buoyant and sedimentation convective forces being negligible in microgravity, mass transport phenomena such as Marangoni and Soret effects dominate and thus influence fluid flows in solidifying material systems. Such flows can dramatically alter the morphology and kinetics of dendritic solidification. A gradient in surface tension such as due to chemical or compositional gradients can drive mass transport, the Marangoni effect, and has been observed to alter dendritic and solidification structures in microgravity [15]. The thermophoretic, also known as Soret, effect additionally alters solidification dynamics in the presence of a thermal gradient [75], [76] and is also pronounced in microgravity [77]. These effects can be captured with solidification dynamics combined with Computational Fluid Dynamics (CFD) approaches. Combined PF – Lattice Boltzmann (PF-LB) coupled models have been recently employed to capture fluid effects on dendritic growth including solute ejection and subsequent transport [78], [79], [80], [81]. CA techniques have also been combined with Lattice Boltzmann (CA-LB) to model dendritic growth [82]. Results from these coupled models indicate the drastic influence of microgravity on convection and thus dendritic morphology during solidification [83].

There is also a need to understand the influence of convection on the evolution of rapid solidification microstructures, phase selection, and the kinetics of metastable phase transformations such as in AM and welding. One such investigation is using the ISS-EML facility in a NASA/ESA/DLR interagency collaboration. Testing under microgravity conditions focuses on a wide range of metallic alloys including binary alloys, pure elements, and complex industrial alloys such as stainless steel, nickel-based superalloys, high-entropy alloys, and glass forming alloys. These experimental datasets may be used to anchor magnetohydrodynamic (MHD) melt flow modeling, PF models, and evaluation of dendrite growth theory. One key component of this work is the ability to conduct concurrent solidification and melt flow experiments in parallel with thermophysical property measurements [28]. The BPS Decadal Survey notes that property measurements in microgravity are vital to understanding fundamental processes, including solidification, and may be combined *in situ* with an accurate measurement of the sample itself using the same apparatus [16].

On earth, gravity-related phenomena dominate with sedimentation and buoyancy-driven flow and severe thermomechanical deformation. In contrast, during directional solidification on-orbit the deformation shrinkage is dominated by surface tension forces allowing investigation of behavior relevant to modeling of additive manufacturing process optimization. A recent flight experiment looked at producing benchmark experiments for the analysis of continuous casting operations by conducting chill casting experiments on steel alloys [84]. Experiments conducted on the ISS complement both ground-based experiments and other microgravity platforms such as parabolic flight and sounding rocket experiments. Figure 17 [85] shows how a steel sample solidifies when intentionally put into contact with a chill plate affixed to the top of the sample holder in experiments conducted using the ISS-EML.

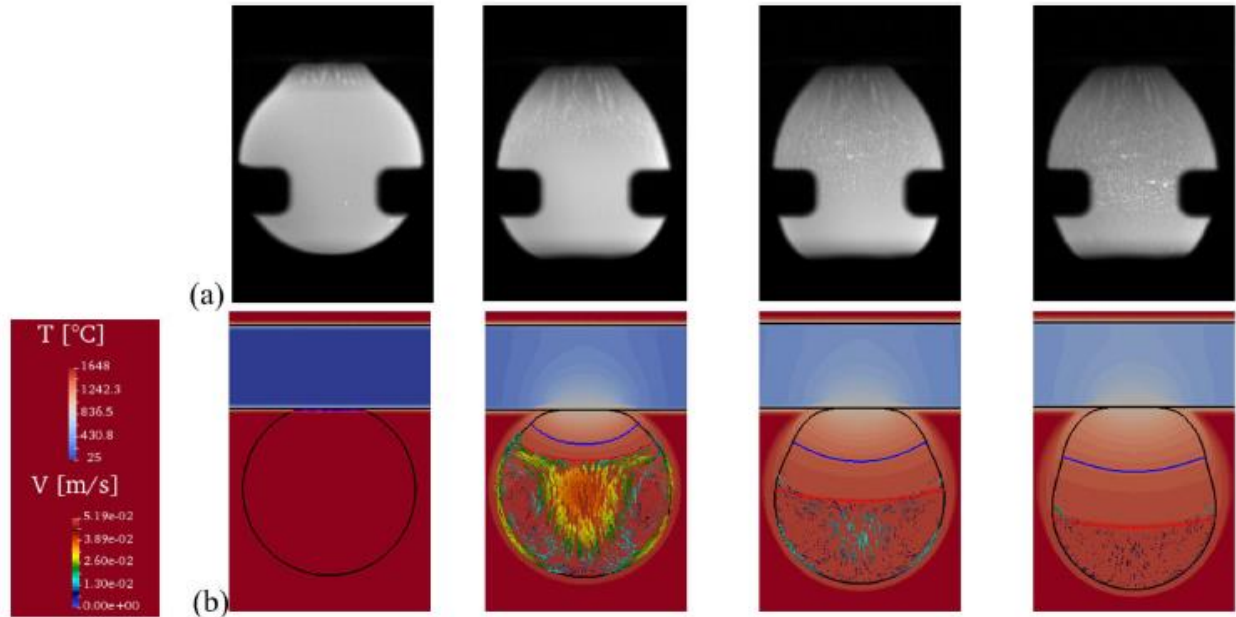


Figure 17: Evolution of structure during chill casting showing (a) a sequence of images of a Fe-0.9C-0.2Si steel solidifying in microgravity and (b) modeling of the fluid dynamics and thermal history of the resulting solidification front. [85]. Figure from D. M. Matson et al., “[Electromagnetic levitation containerless processing of metallic materials in microgravity: rapid solidification](#)” licensed under [CC BY 4.0](#).

3.2. Computational

Modeling microgravity experiments, especially those pertaining to solidification, requires computational tools capable of describing phenomena on extremely varied length and time scales from the microscale of the dendrite tip radius (Figure 15) to the intermediate micro/macro scale of dendritic arrays (Figure 16) to the macroscale of a casting processed by directional solidification (Figure 17). These computational tools are currently in use in parameter selection to control and select convective experimental conditions during electrostatic levitation (Figure 7) and electromagnetic levitation (Figure 17) [85]. There are almost no validated open-source tools available for macroscale modelling of coupled solidification and fluid flow, while a few tools described in what follows are actively being developed for microscale modeling. As a result, modeling of simultaneous fluid flow with solidification is an active area for ICME research to optimize processing conditions and control microstructural evolution. For example, surface tension-driven Marangoni convection can be seen to influence chill casting dynamics in the electromagnetic droplet example of Figure 17 based on linking a level-set diffuse-interface macroscale solidification model to a coupled solute segregation and heat transfer model [84], [86], [87]. An unexplored potential opportunity to refine these predictions is to merge magnetohydrodynamic modeling (MHD) of the levitation field-induced convection [88] with predictions from surface tension driven flow. This requires linking microscopic and macroscopic modeling approaches.

Before modeling coupled solidification-fluid flow, solidification alone must be properly described and refined in a computational model. This report focuses on BPS-supported academic research codes and free, open-source community codes due to their accessibility and the open science drive embodied by the Transform to Open Science (TOPS) initiative at SMD. There are multiple open-source tools available for PF modeling. One under active development is PRISMS-PF, which is a parallel matrix-free finite element code that performs PF modeling and microstructural evolution, including solidification, grain growth, and solid-state phase transformations [89], [90]. It is currently formulated to solve 2D problems, and a 3D version is under development. PRISMS-PF is developed by the PRedictive Integrated Structural Materials Science (PRISMS) Center, supported by the Department of Energy (DOE) and University of Michigan. It can run on multiple CPUs, with GPU-based development underway by the PRISMS team.

The Multiphysics Object-Oriented Simulation Environment (MOOSE) tool is another actively developed open-source multi-physics finite element code primarily developed by Idaho National Laboratory (INL) with over a

hundred contributors [91], [92]. The framework is scalable to over 300,000 cores, and has seen recent development for GPU capabilities [93]. MOOSE consists of many modules, including chemical reactions, fluid-structure interaction, peridynamics, optimization, heat conduction, tensor mechanics, and others. The PF module has capabilities for two-phase models, the Kim-Kim-Suzuki model, the Sublattice KKS model, multiphase models for N phases, and the Grand Potential Multi-Phase, Multi-Order Parameter Model [94], [95], [96]. It also includes multi-physics coupling to mechanics and can solve some 3D problems.

The equations governing linear elasticity and the flow of Newtonian fluids are well accepted. By comparison, PF methods for solidification are still under active development. Thus, the challenge in using PF models is two-fold: choosing a particular PF model, and then ensuring that the equations are solved to a desired accuracy. Benchmark experimental data sets are essential in determining both the proper PF method for a given application, and the fidelity of the simulation. It is then not surprising that two of the publicly available community-based PF codes, PRISMS-PF and MOOSE, employ different PF formulations.

One of the principal challenges with the PF method is the need to employ diffuse interfaces that are much thicker than those in reality; this is necessary to have a computationally tractable model. This can be a challenge when the interfacial free energy is coupled to both the interfacial thickness employed in the simulation and the bulk free energies. The Kim, Kim, and Suzuki multiorder parameter model [94], that builds upon the work of Tiaden et al. [97], assumes that the interface is composed of a mixture of two phases with a volume fraction that varies across the interface. This decouples the magnitude of the interfacial energy from the interface thickness and the free energies of the bulk phases. However, the approach employs fictitious compositions whose values are fixed by requiring local equilibrium at every point in the system. These local equilibrium conditions must be determined at each mesh point and every timestep, a considerable computational burden. An advantage of this approach is that it has been extended to model multiple phases, multicomponent alloys, and many grains [98]. Thus, it is a very flexible model and is incorporated in MOOSE. An approach that also addresses the need to use larger than realistic interface thicknesses is the grand-potential model by Plapp [99]. In this case the evolution of the chemical potential, not the concentration, is computed, removing the need for fictitious compositions. The grand potential formulation has also been incorporated in MOOSE.

Aside from the accurate description of the interfacial free-energy, the choice of a computationally tractable interface width on the micron scale generates solute trapping in the solid phase at low solidification rate, an effect that only occurs physically at high solidification rate with a physical nanometer scale interface width. Historically, this difficulty was overcome in one formulation by the introduction of an “anti-trapping” solute flux to ensure that the PF equations capture the well-accepted sharp interface formulation for solidification in the limit where the solid-liquid interface is in local equilibrium and the solute diffusivity in the solid is vanishingly small [100]. This approach has been used for directional solidification of dilute binary alloys [53]. An “anti-trapping” solute flux is not typically employed in the multiorder parameter models, but they are in the MOOSE code. However, this approach employs a dilute solution model for a binary alloy, unlike the previously mentioned approaches that can employ general free energy functions and cannot treat multiple grains. Nevertheless, the dilute solution assumption is satisfied by the DECLIC experiments, and thus this model can be tested against this benchmark dataset. The model of Echebarria et al. is used in the PRISMS-PF code.

Thus, the two major community codes do not use the same PF formulation for solidification of alloys. The MOOSE code uses the grand potential and multiorder parameter models, but it has not employed the asymptotic method of Echebarria et al. whereas the PRISMS-PF includes the Echebarria et al. model but not the grand potential or multiorder parameter models. In view of the highly nonlinear nature of interfacial evolution during solidification, the different formulations may diverge if the underlying physics is not exquisitely captured, thus indicating where gaps remain in the codes or formulations and intimating the need for validation datasets to provide anchoring views of the underlying physical phenomena.

PRISMS-PF

As a demonstration of the possibility of BPS-supported and validated research codes finding utility in the context of the broader ICME community, the Northeastern University Karma group worked closely with the PRISMS-PF code developers to assess to what extent graphics-processing-unit (GPU) based research codes (developed in the Karma group) and publicly available codes for binary alloy solidification such as PRISMS-PF can be used to model flight experiments such as IDGE, PFMI, CETSOL, and DECLIC-DSI. These experiments provide unique benchmark data for validating currently available and future codes under well-controlled diffusive growth conditions with negligible buoyancy-driven convection. The Karma group’s GPU-PF code was both supported in development by BPS and

used BPS-funded and -relevant datasets from microgravity materials science flight experiments for validation. The question was then whether this code could converge with an open-source, community code – PRISMS-PF in this demonstration. This establishes a verification approach that could be extended to other codes as well.

Publicly available 2D “alloySolidification” test case

As a first step, a direct comparison was made between the results of a 2D research code in the Karma group and the PRISMS-PF code for the publicly available “alloySolidification” application in PRISMS-PF corresponding to the 2D directional solidification of an aluminum-3wt% copper alloy under additive manufacturing conditions (i.e., large isothermal velocity $V=188$ mm/s and large thermal gradient $G=265$ K/cm). This example uses a very small 2D system size of $\sim 10 \mu m \times 30 \mu m$ and total physical simulated time of ~ 0.02 seconds with a width $W=0.098 \mu m$ of the spatially diffuse interface thickness in the PF model. It was chosen for public release by PRISMS-PF developers to enable users to run this example with a typical execution time less than about 15 minutes with a limited number of cores as in a common desktop or laptop workstation. The 2D research code (referred to hereafter for brevity as GPU-PF code) uses a finite-difference discretization on a regular square mesh [1] of the partial differential equations (PDEs) corresponding to the quantitative PF model of directional solidification with anti-trapping [20]. This discretization is ideally suited to take advantage of the massively parallel capability of GPUs but does not provide adaptive meshing to dynamically reduce the number of grid points. The PRISMS-PF code uses a finite element method (FEM) discretization of the identical partial differential equations parallelized with Message Passing Interface (a parallelization framework) on a more traditional multicore architecture but enables adaptive meshing. The comparison of the GPU-PF and PRISMS-PF codes shows that the two codes yield essentially the same dynamical evolution of the solid-liquid interface starting from a small circular crystal seed to an almost completely solidified sample (top of Figure 18). Performance wise, with a 1.24 sec wall time on a single V100 GPU, the GPU-PF code is about 30 times faster than the PRISMS-PF code with adaptive meshing executed on all 128 cores of a compute node at 2.45 GHz on a 3rd Gen AMD EPYC CPUs (AMD EPYC 7763) architecture (bottom of Figure 18). The deviation from ideal scaling behavior is due to the overhead in communication between cores, which is expected in simulations with a small number of degrees of freedom. The deviation is more pronounced as the number of degrees of freedom per core decreases, which occurs when more cores are used.

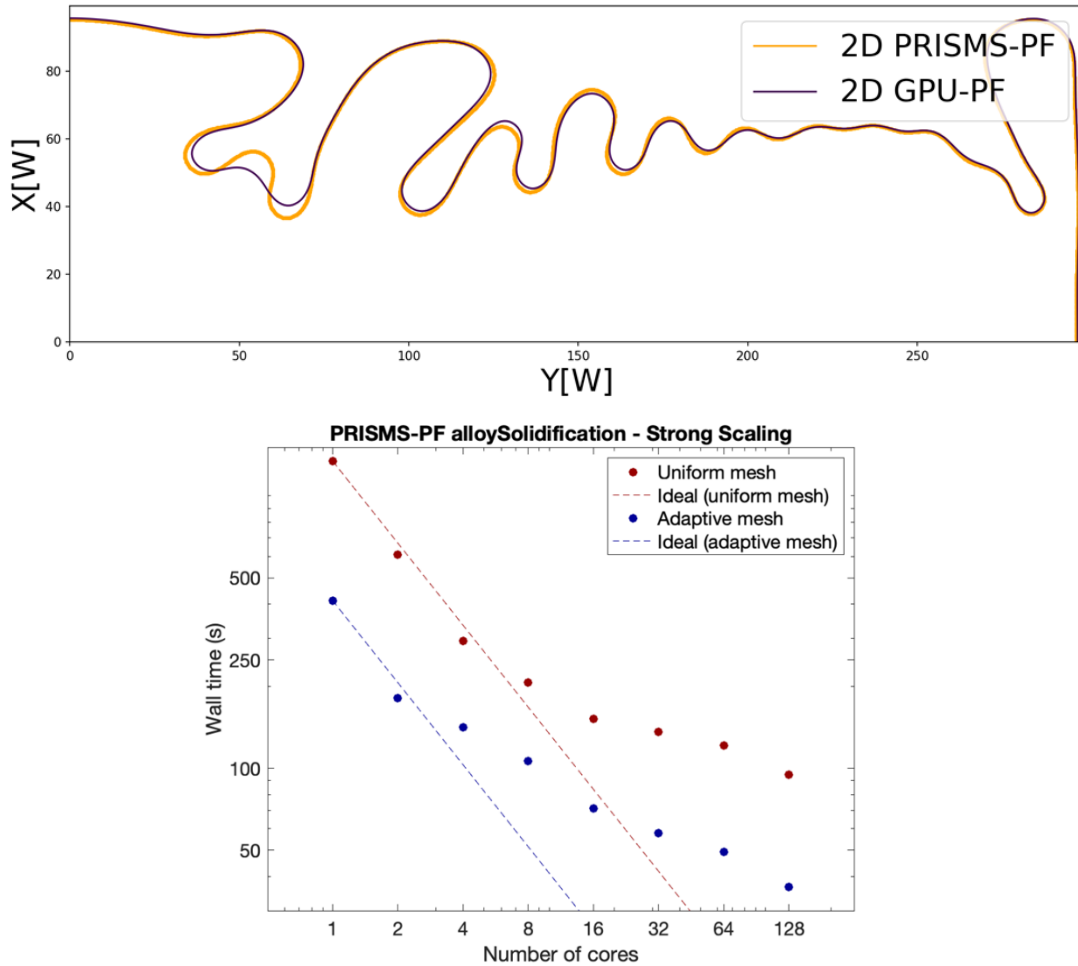


Figure 18: Top: comparison of solid-liquid interfaces ($\phi = 0$ PF contours) at the late stage of solidification predicted by GPU-PF and PRISMS-PF codes for the 2D directional solidification of an aluminum-3wt% copper alloy under additive manufacturing conditions. Bottom: execution time vs. number of cores of the PRISMS-PF code using uniform (red) and adaptive (blue) meshes and running on 3rd Gen AMD EPYC CPUs (AMD EPYC 7763) compute nodes at 2.45 GHz. The dotted lines represent ideal scaling behavior. Both PRISMS-PF and GPU-PF use a mesh spacing $dx = 0.78125$ W and time step $dt = 2 \cdot 10^{-3} \tau_0$ with interface thickness $W = 0.0524 \mu\text{m}$ and time constant $\tau_0 = 2.7 \cdot 10^{-3} \text{s}$ in the PF model.

DECLIC DSI-R flight experiment in 2D

In a second step, the above comparison was extended to parameters of the DECLIC DSI-R flight experiments (Table 1) corresponding to a transparent succinonitrile (SCN)-0.46wt% camphor alloy directionally solidified at a low isotherm velocity ($V = 6 \mu\text{m/s}$) and thermal gradient ($G = 12 \text{ K/cm}$). Modeling this second case is computationally more demanding due to the considerably larger system size of $\sim 0.648 \text{ mm} \times 3.89 \text{ mm}$ and total physical simulated time of 500 s. The computational cost of simulating larger length and time scales is partially mitigated by using the quantitatively efficient PF formulation with anti-trapping referenced above. This formulation makes it possible to choose the width of the spatially diffuse interface thickness ($W = 1.265 \mu\text{m}$) as a fraction of the dendrite tip radius and the characteristic time scale of the PF evolution ($\tau_0 = 0.363$ second) on an experimentally relevant time scale. The comparison of GPU-PF and PRISMS-PF results (Figure 19) shows that the solid-liquid interfaces overlap perfectly at $t = 500$ s, except deep in the liquid groove region. This difference reflects a transient sidebranching instability during the initial destabilization of the perturbed planar interface that is seen to have a negligible influence on the subsequent morphological development of the interface that is controlled by the growth kinetics of the dendrite tips. This kinetics is well-resolved by both codes and, as a result, the interfaces overlap perfectly at later stages of solidification as shown in Figure 19.

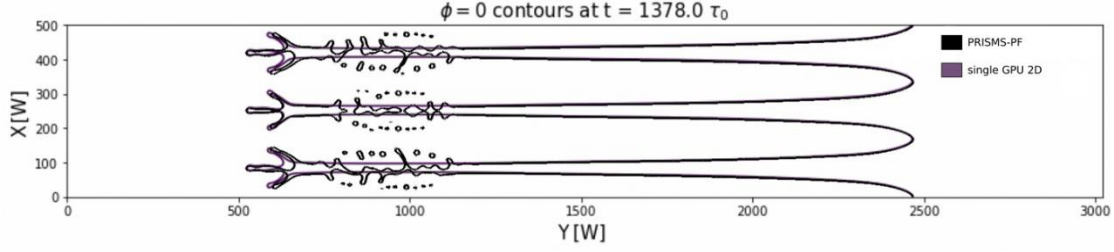


Figure 19: Comparison of solid-liquid interfaces ($\phi = 0$ PF contours) predicted by 2D GPU-PF and PRISMS-PF codes for DECLIC DSI-R parameters of Table 1 (SCN-0.46wt% camphor alloy, $V=6 \mu\text{m/s}$, and $G=12 \text{ K/cm}$) and with mesh spacing $dx = 0.984375 \text{ W}$ and time step $dt=5 \cdot 10^{-4} \tau_0$.

Table 1: Parameters of 2D and 3D PF simulations for DECLIC DSI-R flight experiments.

Symbol	Value	Unit
c_0 camphor concentration	0.46	wt%
D_L diffusion constant	2.7×10^{-10}	m^2/s
k partition coefficient	0.1	-
m liquidus slope	-1.365	$\text{K}/\text{wt}\%$
Γ Gibbs-Thomson coefficient	6.478×10^{-8}	K m
ϵ_4 crystalline anisotropy	0.011	-
G temperature gradient	12	K/cm
V isotherm velocity	6	$\mu\text{m}/\text{s}$
W PF interface thickness	1.265	μm
τ_0 PF time constant	0.363	s

DECLIC DSI-R flight experiment in 3D.

The above 2D simulation study was extended to the 3D case of direct experimental relevance using the same parameters listed in Table 1. The 3D study was aimed at i) evaluating the convergence of the GPU-PF and PRISMS-PF codes as a function of grid spacing and time step, and ii) assessing their performance as a basis to estimate the computational resources needed to model flight experiments on a full sample scale as will be discussed further below. The PRISMS-PF developer team graciously agreed to accelerate the development of their 3D binary alloy solidification code for the purpose of this report. This 3D code will soon become publicly available and has already been made available to NASA scientists. The simulations were carried out in a $0.194 \text{ mm} \times 0.194 \text{ mm} \times 2.332 \text{ mm}$ domain size with two different mesh spacings, $dx=0.8 \text{ W}$ and $dx=1.2 \text{ W}$ with W listed in Table 1, corresponding to $128 \times 128 \times 1536$ and $192 \times 192 \times 2304$ grid points, respectively, on the fixed regular mesh used in the GPU code. In the PRISMS-PF code, which uses adaptive meshing and second-order elements, those same dx values represent the minimum mesh spacings used to resolve the rapid variation of the PF in the spatially diffuse solid-liquid interface region.

The results pertaining to the convergence of the GPU-PF and PRISMS-PF codes are shown in Figure 20. The results show that the two codes converged as a function of grid spacing and yield essentially identical results. Small differences in the results can only be resolved by superimposing 2D cross-sections of the 3D results at a higher magnification on the scale of the dendrite tip radius as shown in Figure 21.

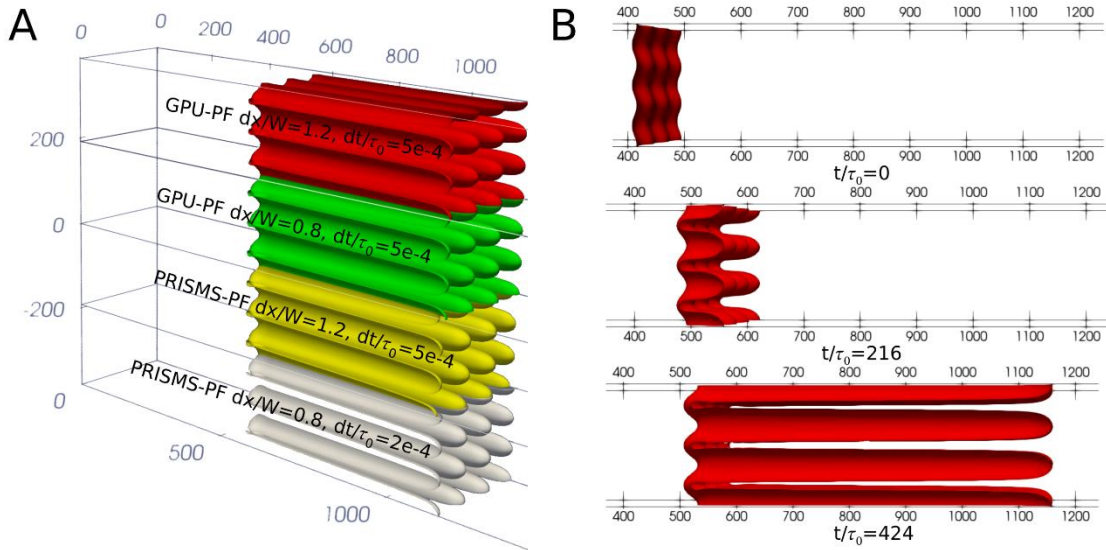


Figure 20: A) Comparison of solid-liquid interfaces ($\phi = 0$ contours) predicted by 3D GPU-PF and PRISMS-PF codes for DECLIC DSI-R parameters of Table 1 in a $0.194 \text{ mm} \times 0.194 \text{ mm} \times 2.332 \text{ mm}$ computational domain at time $t = 424 \tau_0$ ($\sim 154 \text{ s}$). B) Interfaces at different times for the same red GPU-PF simulation of A).

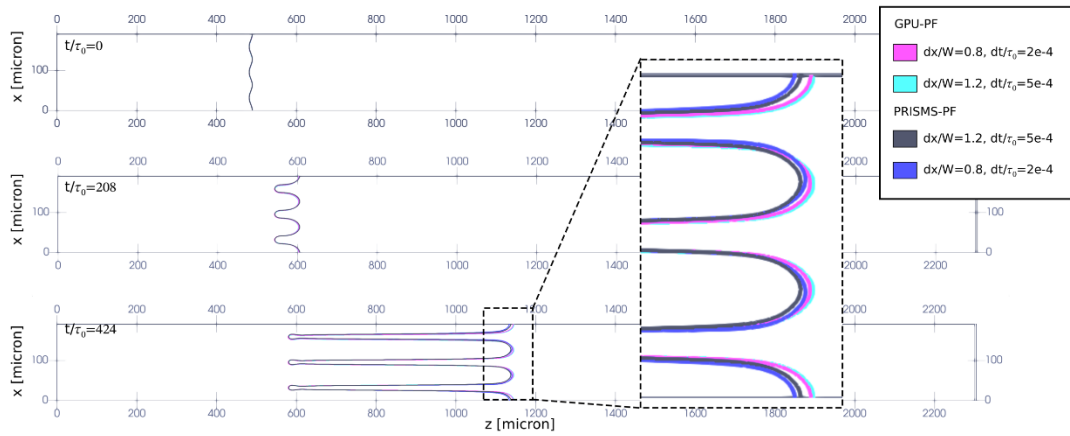


Figure 21: Comparison of 2D cross-sections of 3D PRISMS-PF and GPU-PF interfaces shown in Figure 20. Small differences on the tip scale are only visible at higher magnification.

The results pertaining to the performance of the two codes are shown in Figure 22.. The GPU-PF simulations were carried out with 1 and 2 V100-SXM2 GPUs. The PRISMS-PF simulations were carried out with 128, 256, 512 and 1024 cores (corresponding to 1, 2, 3 and 4 3rd Gen AMD EPYC CPUs AMD EPYC 7763 compute nodes at 2.45 GHz with 128 cores per node). The performance was assessed by comparing the wall time to execute the 3D simulation of Figure 20. Optimizing the performance (i.e., minimizing the total number of computations that determines the wall time) is generally achieved by choosing the mesh spacing and the time step as large as possible. Performances tests were carried out with $dx=1.2 W$ that was found to be the largest mesh spacing that provides adequate resolution (Figure 20). GPU-PF uses a finite-difference discretization with an explicit time-stepping scheme that makes it possible to use a larger time step than PRISMS-PF that also uses an explicit time stepping scheme, but second order elements that impose a more stringent constraint on the time step. Therefore, the GPU-PF simulations were carried out both with the same time step $dt = dt_0$ used in PRISMS-PF and with a seven times larger time step $dt = 7dt_0$, which is below the limit of numerical stability of the explicit scheme and still provides a good resolution of the 3D solution as shown in Figure 23. Choosing a larger time step is made possible in the GPU-PF code using a preconditioner that enables to resolve the variation of the PF in the spatially diffuse interface region with a grid spacing ($dx/W=1.2$) that is comparable to the mesh size with second order elements in PRISMS-

PF. Performance of PRISMS-PF was optimized by adjusting the remeshing frequency and thickness of the region of maximum refinement around the interface while ensuring solution accuracy, as shown in Figure 24.

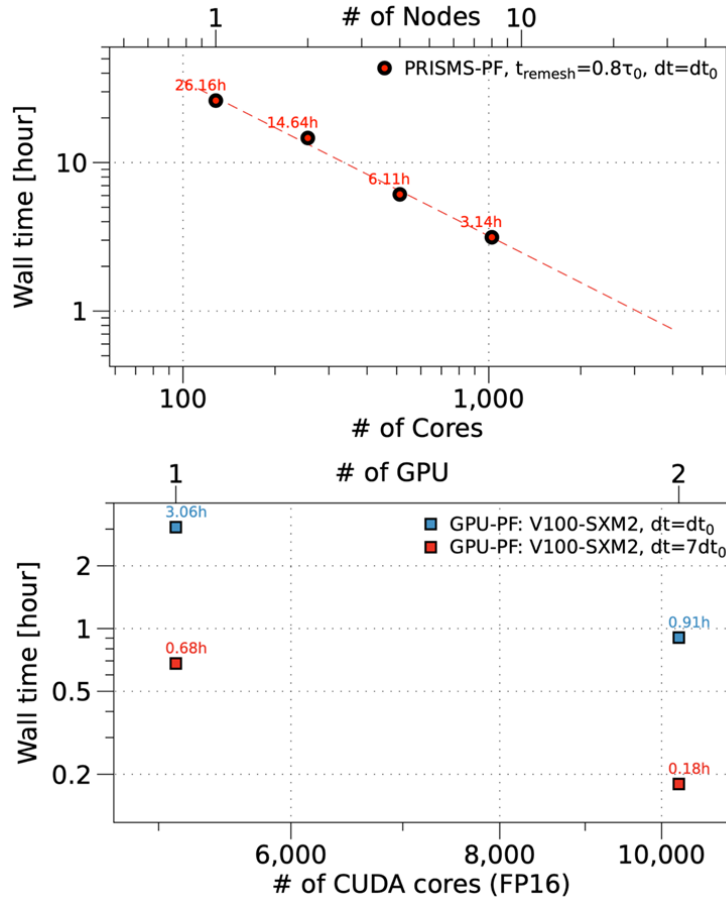


Figure 22: Comparison of wall times of GPU-PF code (bottom: filled squares for 1 or 2 GPUs) and PRISMS-PF code (top: filled circles for 128, 256, 512, and 1024 cores) for the DECLIC-DSI-R simulations of Fig. #3 with the largest grid spacing $dx/W=1.2$ and a time step dt in units of $dt_0=5 \cdot 10^{-4} \tau_0$. The fitted red dashed line in the top plot has a slope of -1.04 that is very close to ideal scaling behavior. The performance of GPU-PF is improved by increasing the time step.

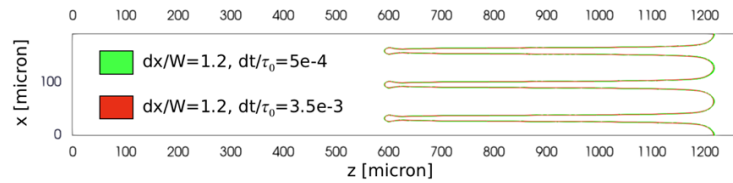


Figure 23: Comparison of GPU-PF interfaces showing convergence as a function of time step (2D cross-sections of 3D for $dt = dt_0$ and $dt = 7dt_0$).

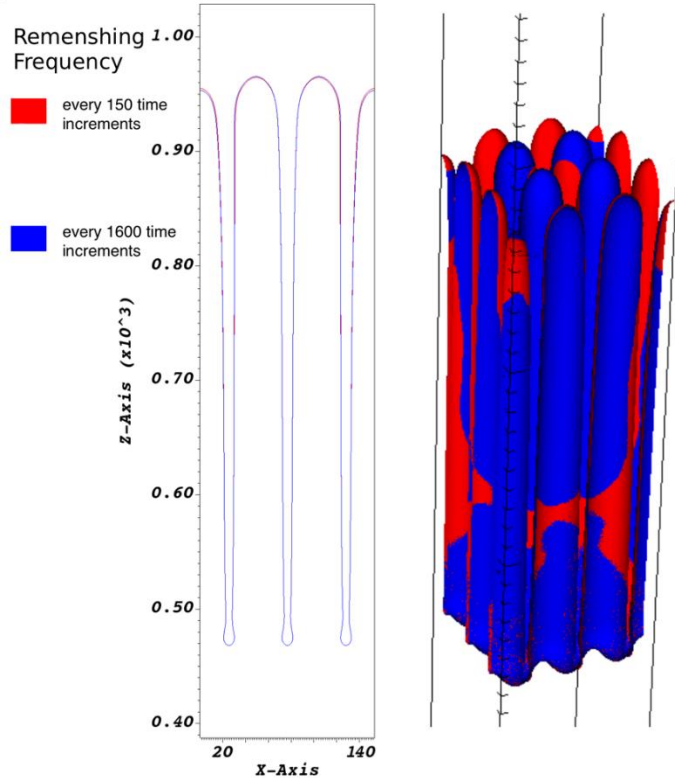


Figure 24: Comparison of PRISMS-PF interfaces showing convergence as a function of remeshing frequency.

The comparison in Figure 22 shows that, for the same time step $dt = dt_0$, GPU-PF with a single GPU has a wall time (3.06 h) comparable to PRISMS-PF with reduced remeshing frequency using 8 nodes (1024 cores) (3.14 h). GPU-PF wall time can be further reduced by a factor of 7 using larger time step (0.68 h) and a factor of ~ 17 using both a larger time step and 2 GPUs (0.18 h). It is worth noting that PRISMS-PF wall time could be potentially further reduced by the implementation of a preconditioner to enable a use of a larger time step or by porting the code onto a GPU architecture, which is currently being pursued by PRISMS-PF developers.

MOOSE

To further understand how open-source, community codes relate to BPS-supported research codes, the Multiphysics Object Oriented Simulation Environment (MOOSE) non-linear solver developed by Idaho National Laboratory was compared in its phase field implementation to that of PRISMS-PF. The example problem chosen was an alloy solidification simulation. While exploring the fundamental equations used in each framework, it was established that PRISMS-PF and MOOSE use different PF formulations, as previously described. Thus, the comparison may indicate how the different formulations capture the same undergirding physics and point the way to further refinements of the codes and formulations.

In PRISMS-PF, the alloySolidification example was solved, using the parameters provided in Table 6 and Table 7 of the Supplementary Material. These values were chosen based on the DECLIC-DSI-R experiments. This PRISMS-PF alloySolidification case was used as the basis for MOOSE exploration. The initial MOOSE example chosen was called GrandPotentialSolidification, located in the PF module example directory anisotropic_interfaces. Results from that example problem given by the MOOSE documentation can be seen in Figure 25, where again blue represents the liquid region and red the solid.

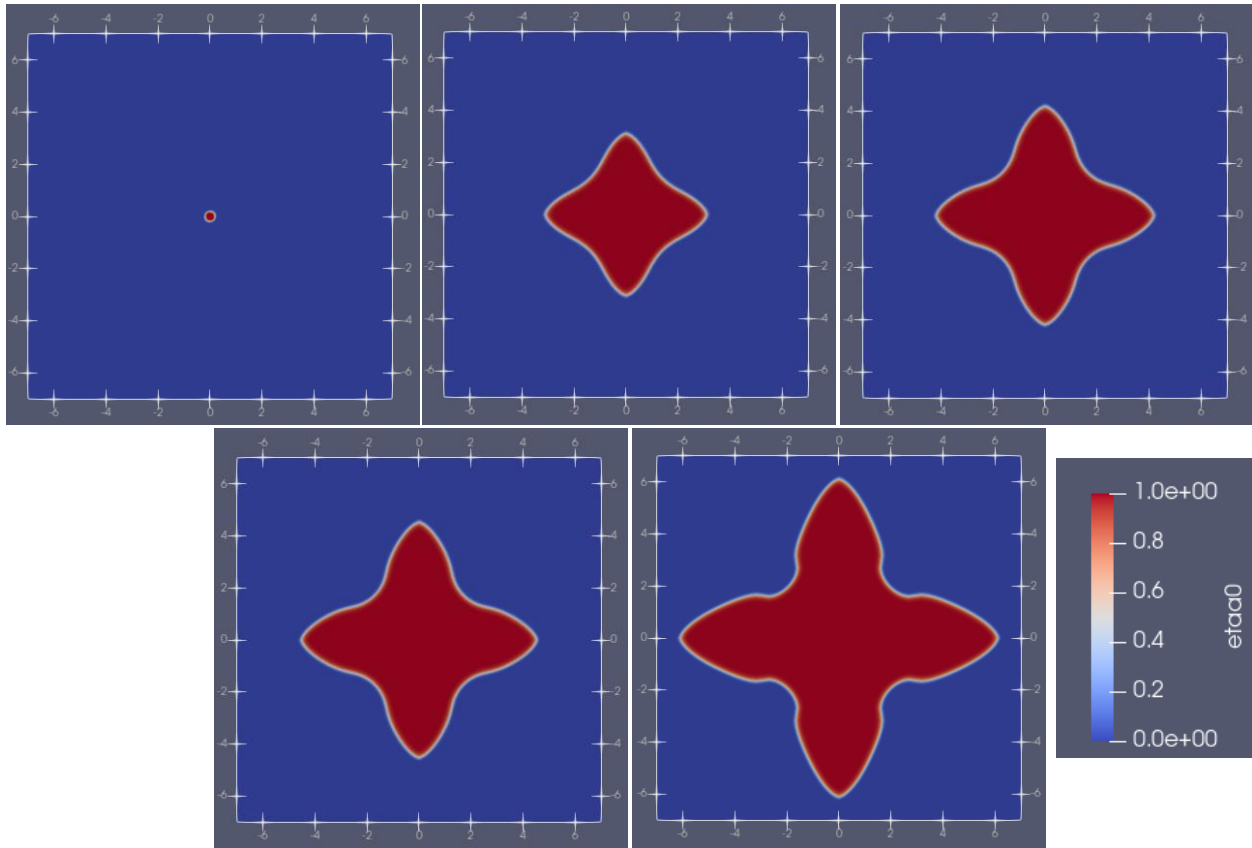


Figure 25. Results from initial MOOSE solidification example over time, where red represents solid and blue is liquid.

This problem was gradually changed to mirror more closely the PRISMS-PF example. First, the initial condition, a circle representing an initial solid region, was moved from the middle of the domain to the bottom left corner. Then, the dimensions were adjusted such that the x-y aspect ratio and relative initial condition radius matched. Multiple other configurations were simulated, including significantly shrinking the height (y-dimension) to force a different behavior at the corner. With each change, results remained essentially the same. Figure 26 shows a comparison of the final PRISMS-PF phase contour versus various MOOSE results. MOOSE and PRISMS-PF results diverge, showing opportunity for further investigation and enhancement of either or both via V&V supported by flight experimental datasets.

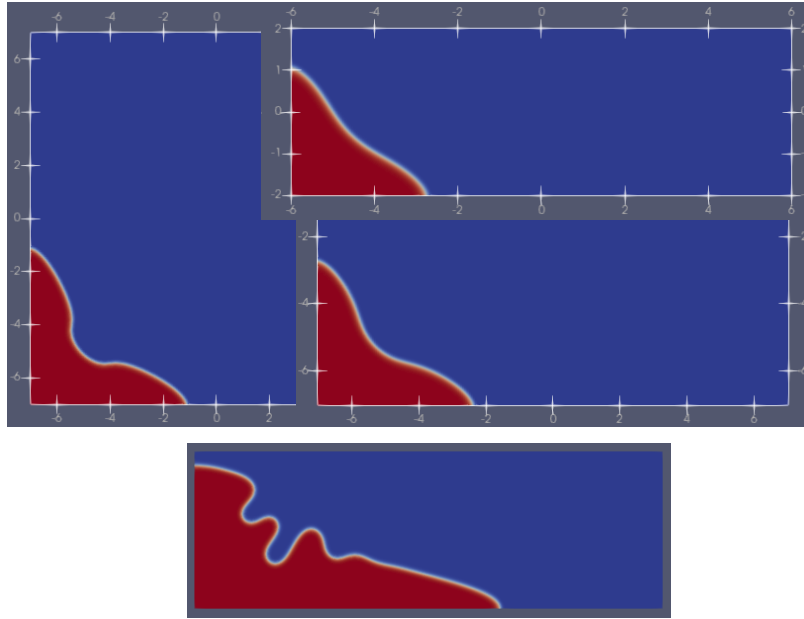


Figure 26. Summary comparison of MOOSE (top three images) and PRISMS-PF (bottom image) solidification results.

Next, focus shifted to the simulation parameters. Assessment of the parameters in the PRISMS-PF and MOOSE simulations found few similarities, which was unsurprising, given the difference in formulations. There was little elaboration in the MOOSE documentation to explain the meaning of most of these parameters. The known overlap can be seen in Table 2. Further simulations were run in MOOSE to ensure parameters were the same in both cases, but this did not result in meaningful progress toward like comparison.

Table 2. Equivalent simulation parameters in PRISMS-PF and MOOSE.

Parameter	Prisms PF	MOOSE
Anisotropy strength	epsilon	anisotropy_strength
Dimensionless diffusivity	Dtilde	D
Solubility partition coefficient	k	caeq / cbeq

Other considerations regarding simulation differences included the reference phase diagram being used by each tool, the interface width (between solid and liquid), and again, the formulation itself. As mentioned, a significant problem when trying to compare the two cases is the lack of MOOSE parameter documentation. Information about the formulation is available via MOOSE provided documentation but the parameters used in input files do not correlate in any predictable way to the variables in the listed equations. Members of the team were in contact with the MOOSE developers, but there was no time to follow up for more details before the writing of this report. This work indicated that tight coordination is required with the developers of open-source, community codes to ensure their convergence with validated, BPS-supported codes and other open-source codes.

Other codes can also be compared to PRISMS-PF similarly to MOOSE. One intercomparison is the community benchmark 3a.1 from PFHub, which models dendritic morphology and evolution in a 2D space [101], [102]. This benchmark was developed with input from multiple ICME community sources, including the influential Center for Hierarchical Materials Design (CHiMaD) and the MGI. As seen in Figure 27, various popular codes show general agreement in this simplistic case. However, divergence in this simplistic case is likely magnified in more complex, realistic cases as with the DSI-R parameters as seen for PRISMS-PF and MOOSE previously. This is an opportunity

for BPS to provide validation datasets that can anchor these models beyond the inter-code comparison that only provides verification as demonstrated here.

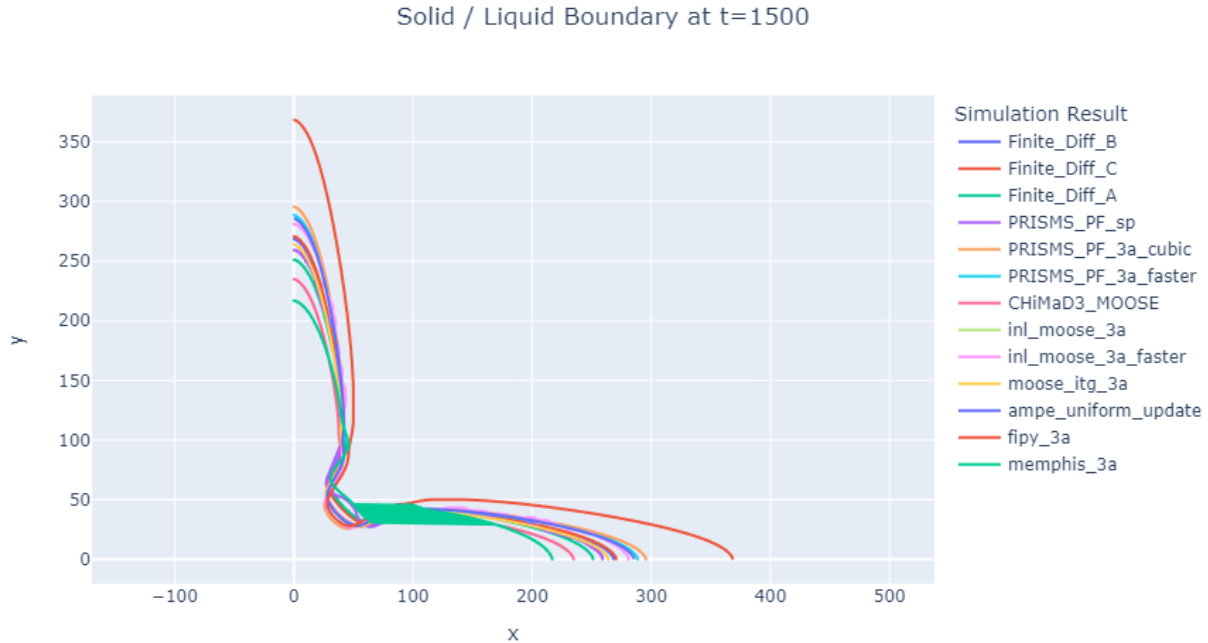


Figure 27: Intercomparison of various PF codes against the PFHub 3a.1 benchmark case [102]. Figure generated from [PFHUB 3a.1 benchmark results](#) under the [NIST License](#).

An example case of fluids-solidification coupling using historical datasets from BPS-funded flight experiments

As aforementioned, fluid flows in solid-liquid mixtures like those seen during solidification influence the micro- and meso-scale structures and thus final properties of the material. Previous work has used BPS-funded flight experiments to understand the coupling between fluid flow and solidification.

The Marangoni force has been hypothesized as a potential source of the observed convection in the PFMI experiment and the spurious grains near surface pores in the MICAST samples. This force arises from temperature-dependent surface tension in conjunction with the temperature gradient driving the solidification process and would induce convective flow across the surface of any bubbles. An initial analysis of the strength of the Marangoni convection [15] supported the Marangoni force as the source of the convection observed in the PFMI experiments. That analysis did include several simplifying approximations, most significantly fixing the location of the bubble within the computational domain and neglecting flow within the bubble itself. Here, the feasibility of simulating a more realistic representation with the initial bubble free to move within the domain was evaluated.

The schematic of the two-dimensional model domain for the PFMI experiment used by Nabavizadeh et al. is shown in Figure 28 below [15]. The 1.3 mm diameter bubble was partially surrounded by solidified dendrites, which were modeled as a porous continuum material with low permeability to reduce fluid flow via Darcy drag. The fluid flow was solved using the continuum Navier-Stokes equations, with the Marangoni force applied through an additional source for the total stress at the bubble-fluid interface. Other boundary conditions were not specified, although they can be inferred to be no-slip at the boundaries of the computational domain and an imposed temperature gradient from the solidus to liquidus. The right-hand boundary was treated as a wall. (*n.b.* this is an imposed temperature gradient and should not be taken as entirely physical; it is imposed to assist in fluid flow modeling)

With a free boundary, the bubble simply moved completely out of the model due to the initial acceleration from the Marangoni forces. Realistic simulation of similar effects requires a more rigorous treatment of coupled fluid dynamics, heat transfer, and solidification. Coupling with a solidification model is necessary for a realistic representation of the initial transients as the gases trapped in solidified alloy are freed during melting, move and merge to form the observed voids, then are trapped by solidifying material. Although approximate models such as

these are adequate to screen for the possibility of physical effects such as Marangoni forces inducing observed defects in solidification experiments, a more fully coupled model with appropriate boundary conditions is necessary for predictive analyses. Finally, the model must be extended to three-dimensional space. Only with a truly volumetric fluids analysis that extends from solid to solid within the evolving dendritic structure can coupled effects be fully shown.

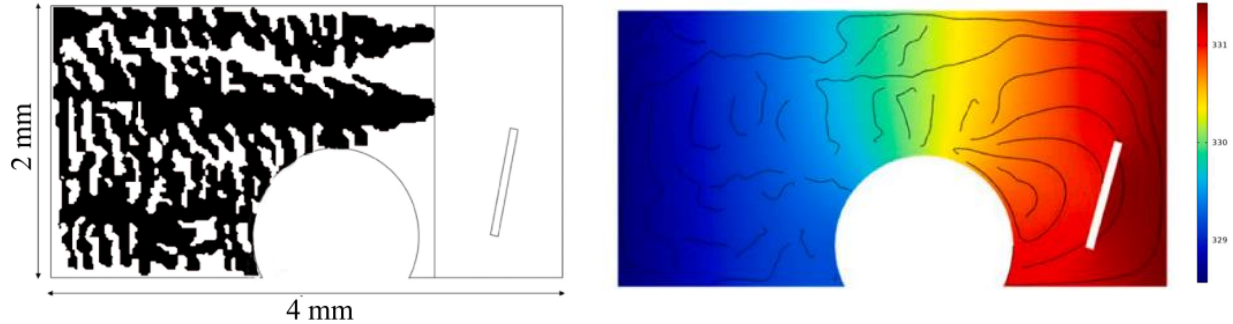


Figure 28. Schematic of Model Domain for Bubble and Marangoni Effects on PFMI Experiment SCN-H₂O Alloy Solidification, left, and Simulated Temperature Distribution with Stream Traces at 6.6 secs, right [15]. Figure from S. A. Nabavizadeh, S. Upadhyay, M. Eshraghi, S. D. Felicelli, S. N. Tewari, and R. N. Grugel, “[Spurious grain formation due to Marangoni convection during directional solidification of alloys in \$\mu\$ -g environment of International Space Station](#)” licensed under [CC BY-NC-ND 4.0](#).

An equivalent computational domain was used for this study, with the region inside the bubble also discretized. The alloy properties were reported by Nabavizadeh et al. were used, and bubble thermophysical properties were taken as nitrogen. The CFD-ACE+ Multiphysics software used for the simulation, with the following key distinctions in the model formulation: solution of fluid dynamics and heat transfer within the bubble, and incorporation of surface tension and Marangoni effects via a local (to each computational cell) surface integral of the forces due to the surface tension-curvature product. As seen in Figure 29, during the early stages of the simulation the presence of the solidified dendrites minimized motion of the bubble but there was sufficient distortion of the bubble shape for surface tension and the Marangoni force to drive more complex flow distributions to occur than predicted in the simplified analysis. As a result, the temperature profiles are also more distorted than seen in the simpler analysis. At 5 seconds simulated time, Figure 30, the solution has stabilized to be like the prior work with the fixed bubble location.

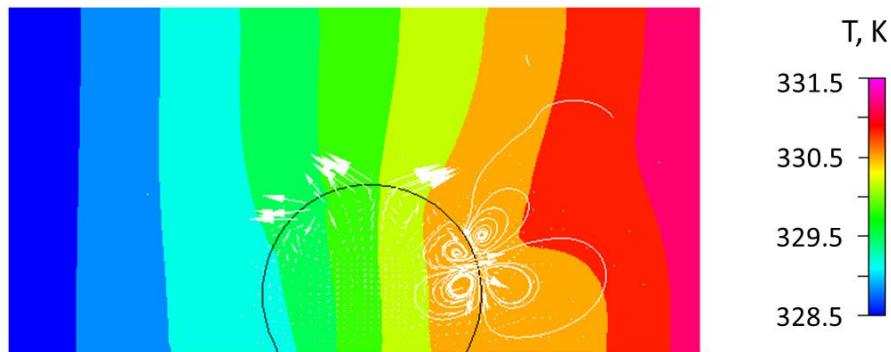


Figure 29. Predicted Streamlines and Temperature Distribution at 3 secs for Bubble and Marangoni Force Effects on SCN-H₂O Solidification. Bubble-Alloy Interface Location shown as black Curve, Stream Traces and Velocity Vectors in white.

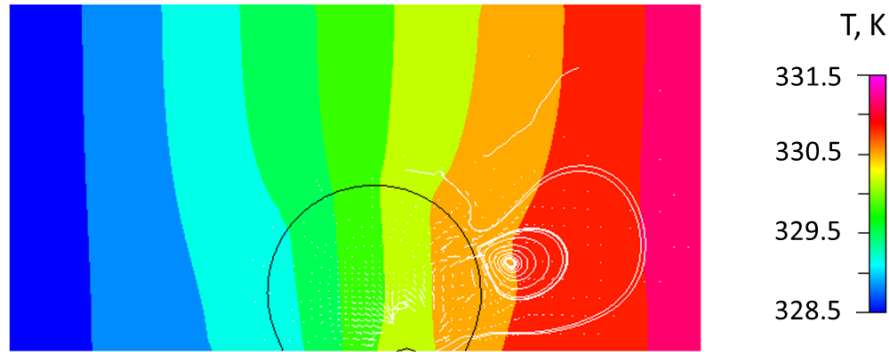


Figure 30. Predicted Streamlines and Temperature Distribution at 5 secs for Bubble and Marangoni Force Effects on SCN-H20 Solidification. Bubble-Alloy Interface Location shown as black Curve, Stream Traces and Velocity Vectors in white.

The schematic of the model domain for the MICAST samples and the predicted temperature distribution at 2 seconds simulated time from Nabavizadeh et al. are shown in Figure 31 below. Although the bubbles and dendrite fragment recirculation could not be visualized, as this is an opaque alloy, the experimental samples included several surface voids with nearby misoriented grains that could be caused by dendrite fragments being transported in the melt. For this model, the fixed bubble began 1 mm from the solidified dendrites ahead of the mush zone and fully within the liquid. As the surface tension flow developed, the predicted streamlines transitioned from a single large recirculation zone to a large primary recirculation above the bubble and a smaller induced secondary cell. Due to the larger Marangoni number, relative to the PFMI simulation with a smaller bubble, the predicted convection is sufficiently strong to distort the temperature profiles in the melt.

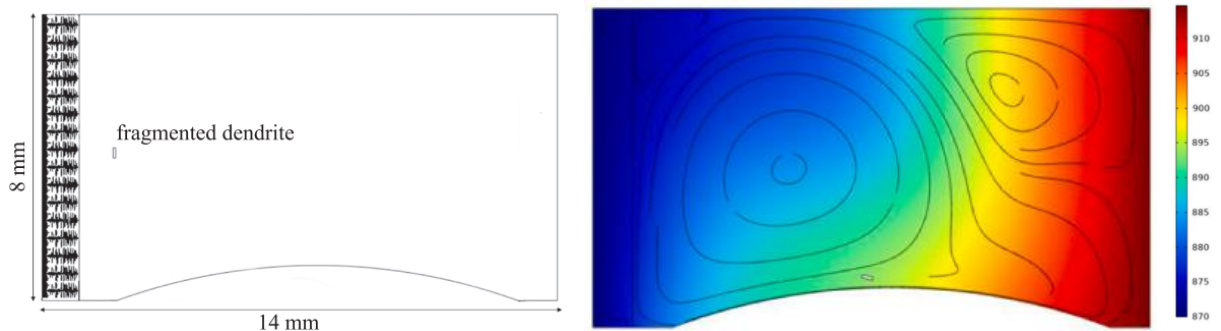


Figure 31. Schematic of Model Domain for Bubble and Marangoni Effects on MICAST2-12 Experiment aluminum-Si 7wt% Alloy Solidification, left, and Simulated Temperature Distribution with Stream Traces at 2 secs, right [15]. Figure from S. A. Nabavizadeh, S. Upadhyay, M. Eshraghi, S. D. Felicelli, S. N. Tewari, and R. N. Grugel, "[Spurious grain formation due to Marangoni convection during directional solidification of alloys in \$\mu\$ -g environment of International Space Station](#)" licensed under [CC BY-NC-ND 4.0](#).

The equivalent model with solution of the gas bubble velocity field and free movement of the bubble within the domain demonstrates the importance of bubble movement in these analyses. As anticipated, the Marangoni force drives a relatively large velocity at the bubble-liquid alloy interface in the early stages of the simulation, Figure 32. With the bubble free to move, it is rapidly transported across the domain to the right-most boundary where it stops due to the wall (zero velocity) boundary condition, Figure 33. After 5 seconds, Figure 34, the bubble shape has relaxed to match the specified contact angle and a flow field like the simplified model has emerged. The main recirculation cell is in approximately the same relative position with respect to the bubble, however it is clearly several millimeters farther from the original bubble location. The temperature field is distorted near the bubble, although not as severely as in the referenced model that fixes the bubble location farther from the solidified alloy and the right-most boundary.

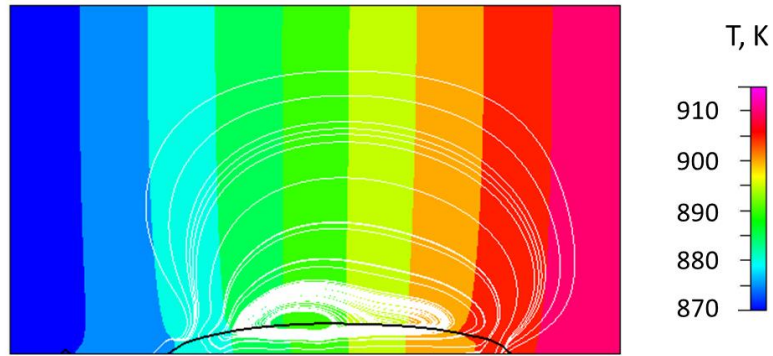


Figure 32. Predicted Streamlines and Temperature Distribution at 0.1 secs for Bubble and Marangoni Force Effects in MICAST2-12 aluminum-Si Solidification. Bubble-Alloy Interface Location shown as black Curve, Stream Traces in white.

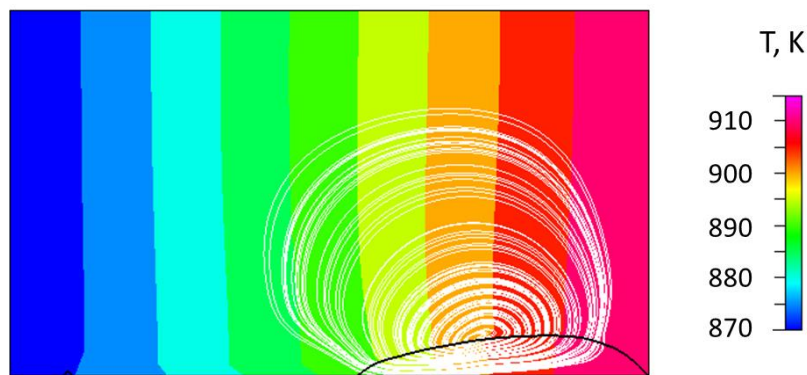


Figure 33. Predicted Streamlines and Temperature Distribution at 0.4 secs for Bubble and Marangoni Force Effects in MICAST2-12 aluminum-Si Solidification. Bubble-Alloy Interface Location shown as black Curve, Stream Traces in white.

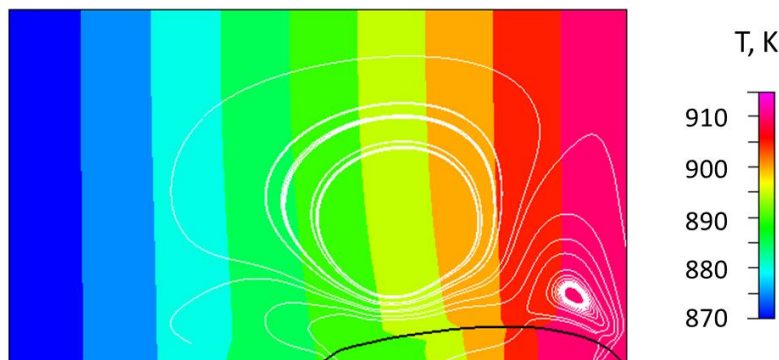


Figure 34. Predicted Streamlines and Temperature Distribution at 0.4 secs for Bubble and Marangoni Force Effects in MICAST2-12 aluminum-Si Solidification. Bubble-Alloy Interface Location shown as black Curve, Stream Traces in white.

This demonstration shows how both temperature fields and fluid flow – even motion of entrapped bubbles – can be different when simulated using more complex computational tools. The changes in temperature, fluid flow, and even physical location will influence the solidification process.

Computational architectures and infrastructure currently available

The performance benchmarks of Figure 22 provide a useful basis for evaluating the computational resources needed to model a flight experiment such as DECLIC DSI on a full sample scale. The crucible diameter is $d=5$ mm and the solidification length L that needs to be simulated to follow the full morphological development of the interface is

typically tens of mm as illustrated in Figure 35. Using $L=50$ mm as a guide, the computational domain volume is $\sim \pi d^2 L/4 \sim 10^3$ mm³ and the physical time $\sim 5 \cdot 10^3$ s. In contrast, the computational domain used for the benchmark of Figure 20 is ~ 0.1 mm³, or 10^4 times smaller, and the total simulation duration (500 s) is 10 times smaller. For a wall time in the range of hours to several days, this would require a massively parallel multi-GPU platform with $\sim 10^3$ to 10^4 GPUs assuming an optimal linear scaling with the number of GPUs. This estimate is supported by the result of a previous study demonstrating the feasibility to simulate directional solidification of a dendritic aluminum-3wt% copper alloy in a ~ 1 mm³ domain size with older 144 K20X GPUs that are at least an order of magnitude slower than current V100 or A100 GPUs [103]. With PRISMS-PF, $\sim 10^6$ to 10^7 cores ($\sim 10^4$ to 10^5 compute nodes) would be required if the red dashed line of Figure 22 is extrapolated to more cores. The above estimates are upper bounds of computational resources needed to simulate an entire sample domain, which are not currently available. It should be emphasized, however, that microstructure formation is predominantly controlled by the growth competition of cells and dendrites that are unaffected by the slow evolution of the mushy zone far behind the solidification front. Hence, in the frame of the moving isotherms, microstructure formation can be studied in a computational domain with a solidification length L comparable to a few times the primary cellular/dendritic array spacing [103] or approximately 1 mm or less [104]. This reduces by a factor of 50 the estimate of the computational domain size, which could then be simulated with 10 to 100 GPUs. This is achievable but still requires a large dedicated multi-GPU computational infrastructure.

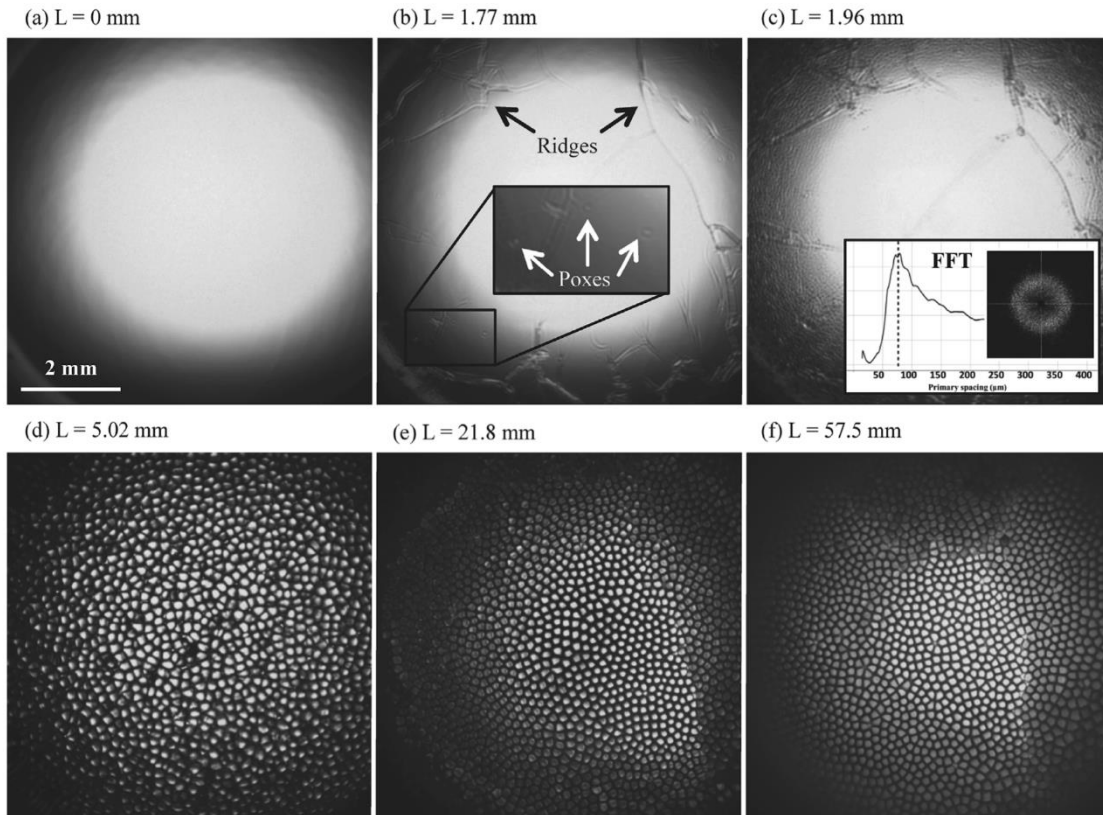


Figure 35: In situ observation of microstructure formation in DECLIC DSI over a cylindrical volume 5 mm in diameter and ~ 50 mm in length.

The PRISMS-PF software was compiled using the included instructions along with the default GNU compiler (version 8.5.0) and MPI library supplied by the NAS facility. The benchmark application was executed using the standard methods recommended by the NAS facility. Seven different CPU architectures, six Intel-based and one AMD-based, were evaluated for performance as a function of CPU core count; PRISMS-PF did not require recompilation to execute on these different architectures. The different architectures assessed along with their performance are shown in Figure 36. Consistent speed-ups with increasing core count are evident, even when the job begins to span multiple nodes. This contrasts with the fall-off seen in Figure 36 when the job spans across more than

one Core Complex (8 CPU cores) in that architecture; further attention should be paid to variation by compute architecture, especially that of interconnects within and between nodes, on the performance of ICME tools such as PRISMS-PF. On the NAS compute architectures, attempts to use OpenMP for parallelism were noticeably slower than MPI and are not reflected in this figure; this difference is also seen in other applications such as production-mode finite volume CFD tools. Additional detail is available in the Supplementary material.

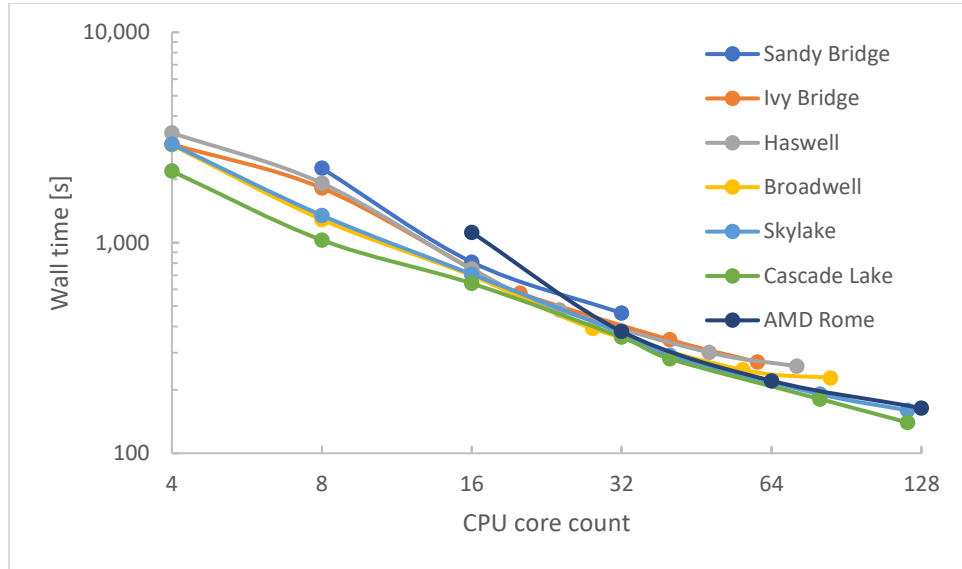


Figure 36: Wall clock time versus number of cores by compute architecture of NAS facilities for the PRISMS-PF benchmark case.

3.3. Future

Experimental

Similar to the future work described for thermophysical properties measurements, ground-based and reduced-gravity experimental facilities are needed to generate benchmark data sets that fill critical gaps in the basic understanding and the prediction of key solidification phenomena. The advent of additive manufacturing in metallic alloys and computationally informed alloy design have spurred a renewed interest in the fundamental underpinnings of solidification processing. The relatively quiescent microgravity environment affords a unique capability to rigorously interrogate physical phenomena providing validation datasets otherwise unavailable. Such data sets would enable the further development of a nascent ICME framework that iteratively utilizes unique data sets obtained for specific alloys to validate computational models that can in turn guide experimental design and make efficient and reliable predictions for a wide range of alloys and solidification processes.

Flight and ground experiments that provide in-situ observation of microstructural evolution continue to offer essential insight into the complex interplay of physical phenomena during solidification processing. Ground-based solidification experiments can be used to bridge flight experiment datasets to industrially relevant alloy systems and complex manufacturing environments. As well, manufacturing technology demonstrations in microgravity environments can be interpreted through invoking models anchored through these fundamental materials science investigations. Microstructure evolution phenomena are critically important for any metal manufacturing process including additive manufacturing and joining processes. In all these processes, a melt pool of metallic elements is transformed to a polycrystalline state by the advance of a solidification front in a positive temperature gradient, for example, when cooler crystalline grains nucleating on the outer walls of a casting or at the bottom of a weld or powder-bed-fusion melt pool grow toward a hotter molten zone. Microstructure formation in a positive temperature gradient is distinct from solidification dynamics of crystal growth from an undercooled melt.

The rarity of flight experiments necessitates complementary ground experiments with reduced convection in a positive temperature gradient to be performed prior to flight, during initial post-flight data analysis and even years later as experimental techniques and instrumentation as well as simulation capabilities generate additional insights

that were not possible at the time of the initial investigation. Historically, solidification flight experiment complexity was driven by the need to impose carefully constrained steady-state growth conditions to compare with analytical theories. This constraint dramatically reduced the cadence of solidification flight experiments. Significant recent advances in computational capabilities offer ever-increasing abilities to model complex dynamic processes such as coupled fluid-solidification and dynamical evolution of interface morphologies under highly transient and complex processing conditions. With advanced instrumentation capabilities such as infrared thermography, transient and complex boundary conditions can be recorded on-orbit and included in benchmark datasets used for validation of computational models. Leveraging these capabilities can dramatically increase the flight cadence and the experimental yield. Flexible small experimental platforms that offer in-situ observation of solidification in a positive temperature gradient such as MARVIN, PFMI, and ESA-TA can provide fast-turnaround access to validation datasets relevant to numerous processes involving solidification of a melt pool. Depending on the molten zone size, which can vary from meter-size castings to powder bed particles of tens of microns, the heat extraction rate can increase by several orders of magnitude resulting in temperature gradients G in the range of $1\text{--}10^6$ K/m and solidification velocities V spanning $\mu\text{m/s}$ in conventional to m/s or higher in rapid solidification processes. Rapid solidification experiments performed in parabolic and suborbital flights are critically needed to generate benchmark datasets in this high velocity range.

Computational

Major computational challenges in solidification modeling include accurate atomistic scale modeling of thermophysical alloy properties, scale bridging between microstructural and part scales, and coupling of solidification and fluid flow.

On the atomistic scale, further development of machine learning interatomic potentials (MLIP) using emerging methods such as PINN (see Section 2.2), the atomic cluster expansion (ACE) [105], and the Ultrafast Interpretable Machine Learning Potentials [106] are critically needed to predict thermophysical properties needed as input parameters in PF models for continuum scale simulations of alloy solidification microstructures, in particular the energetic and kinetic properties of the solid-liquid interface that have a crucial influence on microstructure formation but are notoriously difficult to determine experimentally.

Even armed with accurate atomistic-simulation-derived input parameters, PF codes are presently limited to running a small number of GPUs on a single CPU node, which significantly constrains the simulation domain size. Given the rapid increase in availability and utility of GPU parallelism, further developments are needed to implement PF codes on many CPU nodes each running multiple GPUs. Ultimately, such improvements would unlock orders of magnitude greater computational power than presently applied to solidification simulations – proffering the chance to simulate the entire flight experiment sample volume in three dimensions under diffusive growth conditions as a major first step towards bridging from the microstructural scale to the larger part scale. Such development requires close coordination between developers and users along with benchmark datasets to validate results.

In addition, significant further work remains in validating coupled fluid-solidification models that couple solidification methods appropriate to a given simulation domain size, ranging from PF to DNN to CA with increasing size, to a fluid dynamics method of appropriate accuracy such as LB or CFD.

3.4. BPS role in future

Historical datasets

As seen with the solidification modeling using DSI-R parameters and the coupled fluid-solidification modeling using PFMI & MICAST datasets, existing BPS-funded datasets remain highly relevant and useful in the modern context. In fact, these datasets represent untapped potential with advanced modeling tools and computational resources available now that were not available when originally conducted and analyzed. Considering BPS investments in open science data infrastructure such as PSI and the SMD's TOPS initiative coupled with recent upgrades of the high-end compute capabilities via NAS, there exists an immediate and continuing opportunity to fund re-analysis and extended analyses of historical flight datasets. Potential avenues include but are not limited to expanding the simulated volume through massive parallelism enabled by GPUs, three-dimensional studies enabled by recent improvements in research & community codes, and additional coupled fluid-solidification analyses via advanced fluids modeling tools.

Community, open-source codes

Continued engagement with developers of community, open-source codes will be highly fruitful considering the rapid advances during this study. Within months, interactions with the PRISMS-PF developers yielded substantial engagement with code capabilities relevant to BPS datasets such as DSI-R and enhanced capabilities. Verifying PRISMS-PF with the GPU-PF code using DSI-R parameters demonstrates how BPS involvement – including both expertise and providing validation datasets – is critical to the further development of PF solidification models within the broader ICME community.

Beyond verification, BPS engagement could also expand the capabilities of community codes. Since the link between the grand potential model and the Echebarria et al. model is clear [73], modifications necessary for the MOOSE code to use the Echebarria et al. model are known. After contacting one of the principal developers of the MOOSE PF code, Larry Aagesen, there is interest in modifying the MOOSE code to facilitate a comparison to the PRISMS-PF code. Some progress has been made. An isotropic, isothermal version of the Echebarria et al. formulation has recently been posted on GitHub. Given more time and funding both PRISMS-PF and MOOSE can be modified to incorporate the same PF formulation, allowing for intercomparison based on code architecture differences alone. This would indicate whether the divergences are arising from the formulations capturing different aspects of the physical phenomena or whether differences in the code architecture and execution are leading to differing results.

“Can Do” science with existing equipment and facilities

Previous experimental campaigns – including but not limited to the CSLM series, SUBSA-CETSOL, and DECLIC-DSI series for solidification and numerous uses of the MSFC-ESL, ELF, and ISS-EML – have demonstrated the utility of existing flight hardware to produce world-class science. Not only did these campaigns produce unique data and results but also they, explicitly or implicitly, indicated paths forward to resolve remaining uncertainties and unanswered questions for scientific questions relevant to ICME. There are still numerous materials science questions that can be answered using these existing, known facilities if the proposed experiments can be performed with minimal modifications to reduce expense and lead time. To leverage these existing equipment and facilities while they are still available, see RECOMMENDATION 1.B: Champion “Can Do” science with existing ground and flight facilities and hardware.

Fund further solidification investigations

One opportunity for further BPS involvement in ICME fluids & solidification work is a flight experiment that involves rapid solidification. Existing datasets from BPS-funded flight experiments mostly involve slower solidification rates representative of casting (and most affected by gravitational forces & effects). However, the increasing interest in both additive manufacturing (AM) and welding for in-space applications motivates flight experiments with high solidification rates. These could be dedicated solidification experiments or could be experiments-of-opportunity within technology demonstrations of AM and welding. Ultimately, the data collected would be highly relevant to improving the nascent computational models of rapid solidification processing methods like the AM Module in Thermo-Calc, which is just one example of a commercially available ICME tool that could benefit from V&V using validation datasets from flight experiments.

Another flight experiment opportunity would be expanding beyond binary alloys into engineering alloys. Most solidification flight experiments to date have been conducted with binary alloys with atomically rough solid-liquid interfaces. In contrast, most commercial alloys use several components. There is therefore a crucial need to carry out future flight experiments with well-characterized ternary metallic and transparent alloys that can provide benchmark data to validate the predictions of computational models of multicomponent alloys.

In addition, even within the realm of binary alloys, there is a critical need for flight experiments to generate benchmark data for a large class of alloys that solidify with faceted solid-liquid interfaces growing under far-from-equilibrium conditions, from structural Al-Si two-phase eutectic alloys [107] to templated structures formed by freeze casting [108]. Recently performed ground-based experiments for freeze casting have yielded promising results requiring further validation in a microgravity environment [109].

Fluids and coupling to solidification

In the MICAST investigation of coupled fluid-solidification evolution, different pore-wall contact angles were found. This could have been caused by minute changes in the sample holder material or the wall surface finish. More complex void-wall-material interactions may also be causing these alterations in angles, but it deserves further investigation to enable more repeatability between experimental runs. Updated design of the sample holder and sample loading process could reduce any unintended variability in sample holder, wall, and sample material initial conditions. If differences remain, then the tantalizing possibility of discovering new fluid-solidification physics is uncovered.

4. Meso-/macro-scale

There is also substantial value in scaling models to length-scales above solidification that approach the final part scale. By simulating representative volume elements of sub-regions of parts, the initial forming process can be linked to the mechanical performance of parts during realistic loading scenarios. Such approaches frequently utilize analytical or numerical solutions of the temperature field during processing and solidification and link those temperature fields to microstructure evolution models that can simulate the grain-scale microstructure during and after processing. Various approaches, including the cellular automata (CA), dendritic needle network (DNN), and kinetic Monte Carlo (kMC) methods enable the prediction of large-scale structure in feasible timescales [69], [110], [111], [112]. The DNN approach has been used to model practically relevant geometries such as a sudden change of sample cross-section perpendicular to the thermal axis, which can generate highly transient dendritic array structures [99]. Defects such as porosity also substantially impact the performance of parts and are important to predict. There are various methodologies capable of predicting porosity [113], [114] that can be linked alongside grain evolution techniques to simultaneously predict mesoscale microstructures and defects.

Once processing conditions are linked to mesoscale microstructures and defects from the models, computational methods, such as the finite element method, enable the simulation of local thermomechanical fields to determine part performance metrics; much work continues to link these to processing conditions. Accurate prediction of the mechanical performance of parts in space, under a variety of loading considerations, is critical to the viability of the manufacturing method. Space environments present unique challenges due to the environmental and loading considerations that drive mesoscale failure mechanisms. These space environment effects should be considered while developing microstructure-and-defect-dependent constitutive models. Crystal plasticity models are well established [115] and can take these factors into consideration when modeling the deformation and degradation of additively manufactured polycrystalline alloys.

4.1. Computational

Dendritic Needle Network (DNN)

A scale bridging alternative already discussed above is to use the DNN method that makes it possible to simulate microstructure formation on orders of magnitude longer length and time scales than the PF method but is restricted to growth conditions or alloy concentrations favoring the formation of highly branched dendritic microstructures. The ability of the DNN method to simulate DECLIC DSI-R on the full scale of the crucible is illustrated in Figure 37. Scale bridging is achieved by using PF simulations to characterize the dendrite tip operating state as a function of the strength of crystalline anisotropy, which is used as an input parameter in the DNN simulation. PF simulations are also used to validate DNN predictions of the minimum and maximum stable primary spacings. DNN simulations can then make predictions of microstructure formation and on the sample scale with several dendritic grains. The DNN method is therefore ideally suited to model flight experiments in concentrated alloys such as the CETSOL experiments using metallic aluminum-silicon and aluminum-copper alloys or transparent neopentyl-glycol – (D)Camphor (NPG-DC) alloys.

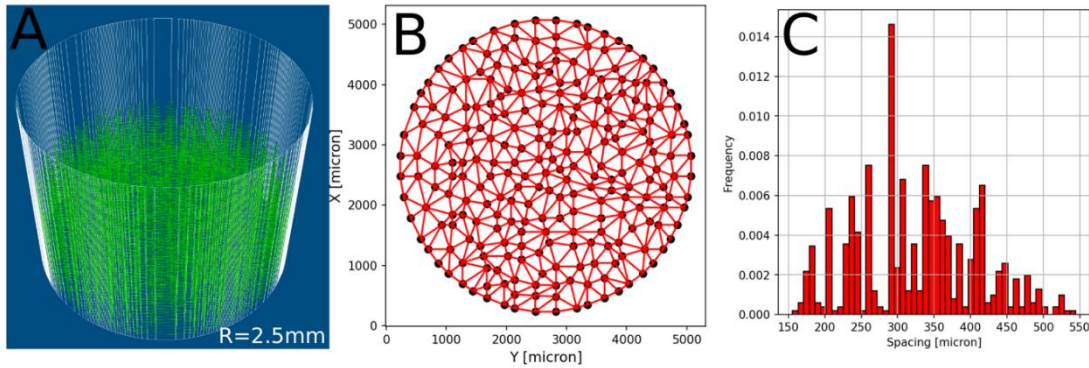


Figure 37: Results of Dendritic Needle Network (DNN) simulations of DECLIC DSI-R on the entire crucible scale of Fig. #8 for $V=3 \mu\text{m/s}$ and $G=19 \text{ K/cm}$. A) Simulation snapshot showing the dendritic array. B) Voronoi tessellation of the dendritic array with black nodes representing dendrite tips and red links between tips used to measure the distribution of primary dendrite spacings shown in C).

Cellular automata - finite element (CAFE)

Cellular automata-finite element (CAFE) simulation tools are widely used to model polycrystalline materials with reduced computational burden compared to PF methods but with increased fidelity compared to stochastic methods (although kinetic Monte Carlo has shown substantial interest in recent years) [62], [63], [69], [116], [117], [118], [119]. CAFE models work by simulating a homogenous voxel around advancing dendrites and applying a physical state (*e.g.* liquid, mushy, solid) to said voxel, terminating when all voxels are solid, and it readily applied to a number of solidification processes such as laser power bed fusion AM [120].

Hybrid Potts PF - kinetic Monte Carlo with SPPARKS

Another mesoscale tools to be considered is the open-source code SPPARKS developed by Sandia National Laboratory [121] which relies on atomistic diffusion calculations as well as coarse scales (voxels) kinetic Monte Carlo calculations in order to model grain growth during melt-solidification. The melt-pool is modeled in the Monte Carlo case via Potts spins indicative of fluid or solid and where randomized spins in region indicate the molten state whereas the aligned neighbor spins indicate a grain or solidified region. More detailed diffusion atomistic simulations and even Hybrid PF-Potts are available (Figure 38), and in the instances of diffusion the alloy may include both several elements/atom types as well as pinned particles, although these are not coupled to other modules such as welding. In the case of the hybrid PF and Potts module, the hybridization is made via the addition of limited PF via the gradient of the concentration in the liquid. This reduced order incorporation of PF does not approach the level of detail which can be obtained via 2D and 3D PF modeling as previously discussed. Any eventual truly hybrid model would have to delve deeper into the dendritic growth modeling – whether via PF or some other method – to truly couple such effects even to the scale bridging via the kinetic Monte Carlo modeling. Therefore the software is useful now or as-is for specific instances of solidification such as directional solidification and hybrid PF Monte Carlo solidification [122], [123], and for limited/approximate modeling of welding and additive manufacturing [119], [124], [125], [126], [127].

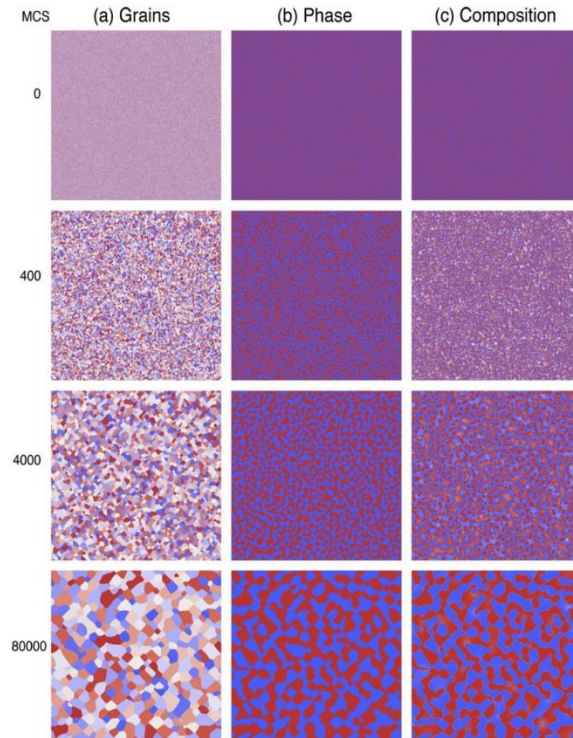


Figure 38: Grain growth and cellular structures are evident from the PF-MC solidification hybrid model [123]. Reprinted from E. R. Homer, V. Tikare, and E. A. Holm, “Hybrid Potts-phase field model for coupled microstructural–compositional evolution,” *Computational Materials Science*, vol. 69, pp. 414–423, Mar. 2013, doi: [10.1016/j.commatsci.2012.11.056](https://doi.org/10.1016/j.commatsci.2012.11.056) with permission from Elsevier.

Still, even the available software modules are limited in scope. For example, directional solidification is performed via a temperature or mobility gradient yet is limited to a single chemical species and only for those conditions. Welding modules relying on Potts Monte Carlo methods (and variations) also limit to a single chemical species and include no other boundary applied forces (gravity for instance), externally introduced mass (filler wire for example), or externally applied thermal or pressure and their gradients. The Additive Manufacturing Modules (Figure 39), however, have seen extensive modification by NASA scientists and have been applied to various complex super-alloys terrestrial AM [127]. A similar coupling approach for welding and directional solidification incorporating more detailed PF is now being sought.

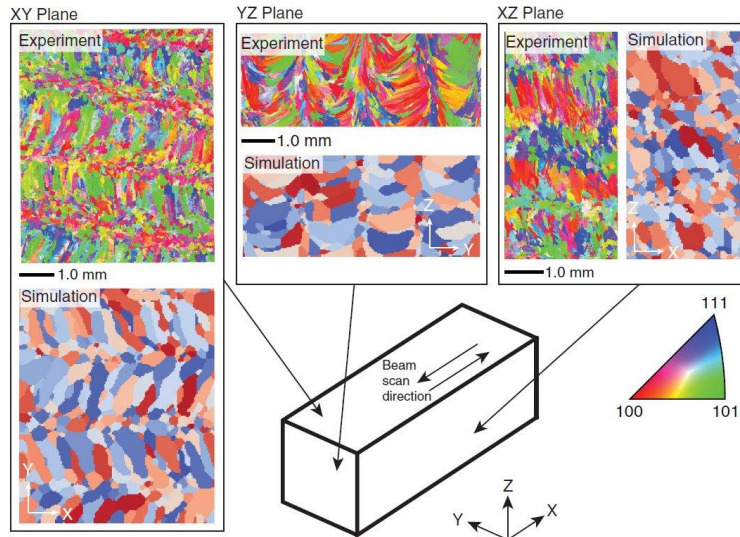


Figure 39: Additive Manufacturing (AM) Laser Powder Bed Fusion (L-PBF) is modeled with experimental and simulated results compared. [127]. Figure from T. M. Rodgers, J. D. Madison, and V. Tikare, “[Simulation of metal additive manufacturing microstructures using kinetic Monte Carlo](#)” licensed under [CC BY 4.0](#).

Crystal plasticity

Mesoscale (polycrystalline) plasticity models simulate the mechanical behavior of metallic materials with explicit representation of grain geometries and additional microstructural descriptors. Key micromechanical modeling tools in the ICME research community for polycrystals include molecular dynamics, discrete dislocation dynamics, continuum dislocation dynamics and crystal plasticity, where each method balances computational cost with the incorporation of the highest fidelity physics possible for the primary deformation mechanisms of interest. Crystal plasticity is one of the most widespread of these mesoscale modeling techniques and has demonstrated great success in capturing the effects of microscale phenomena while retaining the ability for one-to-one comparison to a vast set of experimental work performed at the *same* length and time scales. It has excellent versatility in simulating complex loading states, such as tensile, multi-axial, creep, and fatigue, over a range of thermal and corrosive environments [115], [128]. Crystal plasticity models determine the 3D micromechanical response by accounting for (either implicitly or explicitly) grain geometries, crystallographic orientations, phase content and evolution, annealing and deformation twinning, grain boundary motion, porosity configurations, surface roughness, crack nucleation and propagation phenomena, and more. Most of these features are either derived directly from mesoscale process simulations, e.g. from solidification modeling, [129] or measured from a combination of 2D and 3D characterization techniques, e.g. from electron backscatter diffraction and X-ray computed tomography. A typical example of output from a crystal plasticity simulation is provided in Figure 40 to demonstrate how the precise grain configuration and grain attributes play a critical role in the localization of mechanical fields, leading to precursors for crack nucleation events. From this example, it is observed that the accurate simulation of the polycrystalline microstructure through multi-scale process modeling pipelines, *i.e.* molecular dynamics to dendritic growth to solidification models, is critical for achieving accurate performance predictions from crystal plasticity simulations.

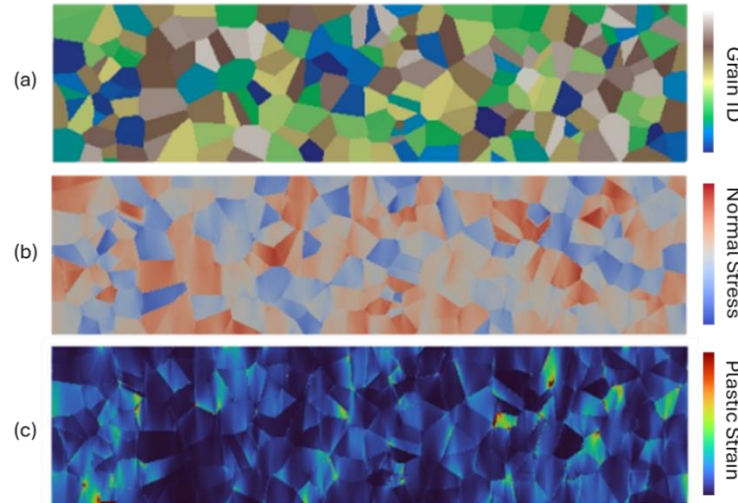


Figure 40: Crystal plasticity simulation results of (a) a polycrystalline microstructure with randomly assigned grain IDs loaded under uniaxial tension to demonstrate representative (b) normal stress fields and (c) plastic strain fields.

Depending on the computational resources available and the fidelity of the underlying material behavior desired, state-of-the-art crystal plasticity modeling can solve for the local micromechanical behavior of 3D microstructures that contain thousands of grains (millimeter scale), using finite element or spectral numerical methods [130], [131]. Out of numerous crystal plasticity codes, examples include that from Los Alamos National Laboratory using spectral solution methods [132] and that from NASA/LaRC that is an internal crystal plasticity finite element software such as the SCalable Implementation of Finite Elements by NASA (ScIFEN) [133]. There is a vast and active domain of research using crystal plasticity to bridge mesoscale microstructural information to higher macroscale (component / structural scale) simulations. The multi-scale approaches are typically categorized under the field of computational homogenization and use a combination of physics constraints and machine learning to upscale material behavior. Some examples of computational homogenization techniques include reduced order modeling, asymptotic homogenization methods, hierarchical methods, and concurrent modeling [134], [135]. This final homogenization stage completes the full multi-scale modeling pipeline to translate the rich information of the microstructural scale to relevant performance predictions of components in application.

4.2. BPS role in future

There are several NASA Centers with interest and experience towards the discussed aims of materials characterization modeling as well as, for instance, weld predictive modeling with an interest in microgravity and vacuum environments. For example, NASA/LaRC has extensively used SPPARKS for additive manufacturing simulations while NASA/MSFC is pursuing its use for welding simulations. Supporting flight experiments or experiments-of-opportunity and their analyses that include microstructural & mesostructural investigations will provide validation datasets to perform V&V on these types of models, especially those with high solidification rates such as AM and welding.

5. Uncertainty quantification

Successfully bridging length-scales also requires uncertainty quantification (UQ) in the models and their inputs, associated experiments, and model linkages. There are two major categories of uncertainty as applied to modeling and simulation: epistemic – associated with lack of knowledge or limited data for specifying model parameters, form, etc. – and aleatoric – associated with inherent randomness or natural variability [136]. Recent studies on UQ [78,79] show the need for an acknowledgement of both sources of variability. Uncertainty in model inputs (*e.g.* parameters of an interatomic potential) is often significant and can be quantified using probabilistic calibration approaches [80]. Also helpful is to vary model inputs and physical parameters to observe the impact of propagation of uncertainty and identify key parameter interrelationships. This guides prioritization of subsequent validation testing. Properties obtained by such numerical prediction may vary based on technique chosen – computational

thermodynamics or molecular dynamic simulation, for instance – and inherent randomness, which may be difficult to deconvolute. Property and other predictions need experimental validation, which introduces its own set of uncertainties that are reducible if carefully controlled but ultimately unavoidable. Figure 4 shows how different computational methods differ amongst themselves and against experimental results. Model linkages are a particular concern for uncertainty: assumptions must be made to homogenize material behavior across length- and timescales, resulting in uncertainty and model discrepancies [81]. Propagating this input uncertainty through the simulations using sampling methods enables model validation and sensitivity analysis, which cannot be accomplished using only best-fit parameters [82]. Finally, multi-fidelity UQ approaches can be useful for propagating uncertainty through high-fidelity ICME models, which are often computationally expensive. By including uncertainty in model predictive capability, appreciation of the potential for a range of possible outcomes allows process designers to quantify margins of safety and better assess reliability. Thus, models may find increasing use for real-world design and performance predictions, infusing into not only in-space sustainability as with the MATRICES campaign, but also industrial manufacturing optimization and development on Earth.

5.1. Typical UQ tasks

Common UQ tasks that will be useful for ICME models relevant to BPS include probabilistic calibration, uncertainty propagation, multi-fidelity UQ, and sensitivity analysis.

Probabilistic calibration generally involves solving an inverse problem for the probability density function of a set of input parameters given experimental measurements (*i.e.* the posterior distribution for the input parameters). The inverse problem is posed by Bayes' rule and is typically solved using Markov chain Monte Carlo, which produces samples from the posterior distribution. Implementations include PyMC [101] and the NASA/LaRC developed Sequential Monte Carlo with Python (SMCPy) [137]. Alternatively, likelihood-free inference (also known as simulation-based inference) methods are available for estimating the posterior in cases where a model is inherently stochastic [138], such as kinetic Monte Carlo-based solidification models. For models that are expensive to sample from, which is common in ICME, surrogate models (e.g., machine learning models built using a library like PyTorch [103]) can be used in the calibration procedure.

The workhorse method for uncertainty propagation is Monte Carlo simulation, in which simulations are completed with many samples from uncertain input parameters to build up distributions on one or more output quantities of interest (QoIs). Computational expense is again a significant concern and can be mitigated by using a more efficient surrogate model. However, surrogate models are less accurate than their high-fidelity counterparts, giving rise to multi-fidelity strategies that seek to balance the accuracy of high-fidelity models with the efficiency of low-fidelity models [139]. Dakota [102], a package developed by Sandia National Laboratories, includes both surrogate model training capabilities and multi-fidelity optimization. NASA/LaRC-developed Multi-model Monte Carlo with Python (MXMCPy) includes implementations of several multi-fidelity optimization strategies with an arbitrary number of models and QoIs [140].

Sensitivity study using PRISMS-PF (2D) and DSI-R parameters

A sensitivity analysis (SA) involves determining the most important input parameters to a model based on their influence on an output QoI. Local sensitivity analysis (LSA) methods are typically derivative-based and provide a deterministic measure of the influence of fluctuations around nominal input values [141]. Recently, LSA has been applied to a model of the columnar-to-equiaxed transition of an additively manufactured nickel-based superalloy [142]. On the other hand, global sensitivity analysis (GSA) methods are probabilistic and consider how the statistical distribution of each input parameter relates to a QoI distribution [141]. The QoI distribution is estimated by running the model with many input samples, like Monte Carlo simulation. The outputs are values like Sobol' indices that relate summary statistics for the QoI and the inputs. Several GSA methods are implemented in the Python package SALib [143], [144]. Example results for GSA carried out for an analytical solidification model are shown in Figure 41.

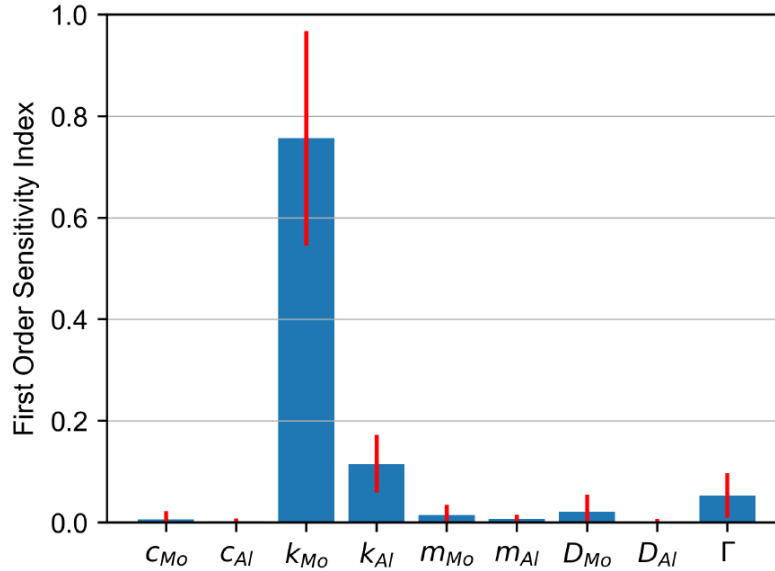


Figure 41: First-order Sobol' indices with uncertainty bounds (red lines) for the absolute stability limit in solidification of an aluminum-Mo alloy. The stability limit is found to be most sensitive to the Mo partition coefficient, k_{Mo} [145]. Used with permission.

Output QoIs for PF models like PRISMS-PF include primary and secondary dendrite morphology and spacing. SA would involve linking variations in these QoIs to variations in input parameters, including interfacial energy, thermophysical properties, and interface thickness. In the case of directional solidification, which is relevant to additive manufacturing, the thermal gradient and cooling rate can also be considered. LSA would require point estimates of each input, as well as a method for calculating appropriate perturbations. On the other hand, GSA would require distributions on the inputs determined from, for example, domain knowledge or a calibration procedure. A benefit of GSA is that the results can be used to target parameters for probabilistic calibration if they cause substantial uncertainty in the QoI estimates. The GSA can then be repeated with new posterior distributions on one or more parameters. However, before drawing quantitative conclusions from a PF SA, the model discrepancy issues addressed in previous sections should be more deeply understood.

Directed acyclic graphs

Directed acyclic graphs (DAGs) can be used to understand and visualize how uncertainty is characterized at different points and through a system [146], [147] and have been previously applied to materials science [148]. Examples are shown below for how a PF model using DECLIC-DSI-R-like parameters would be set up (Figure 42) and for overall uncertainty flow through a scale bridged system (Figure 43).

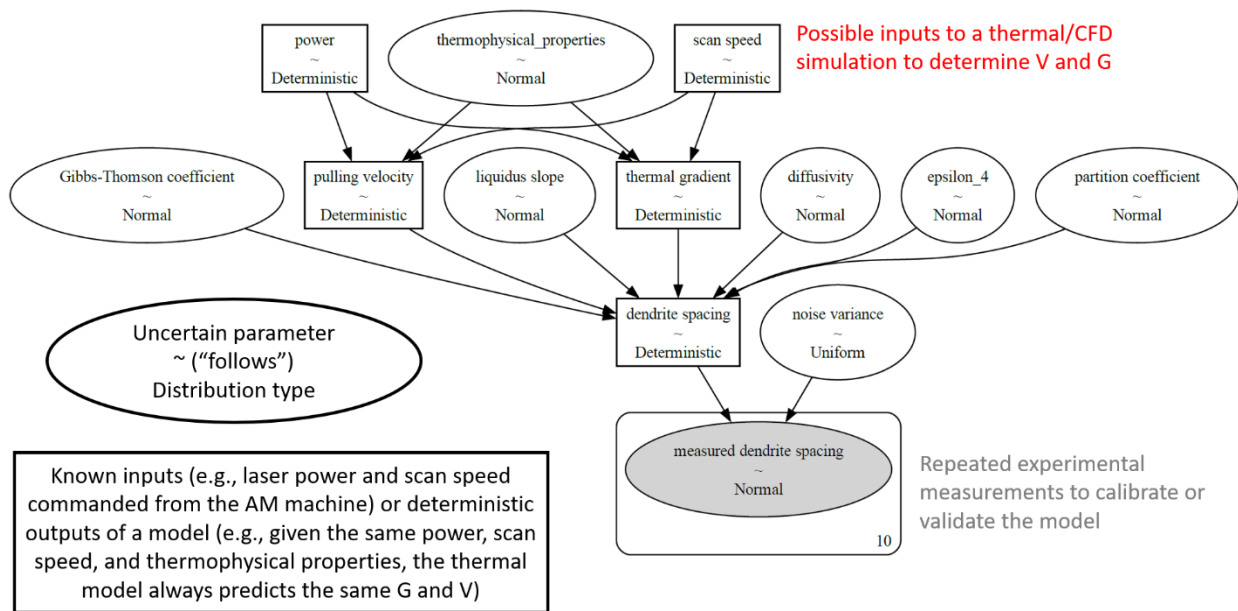


Figure 42: A notional directed acyclic graph for uncertainties in a PF model of dendritic solidification.

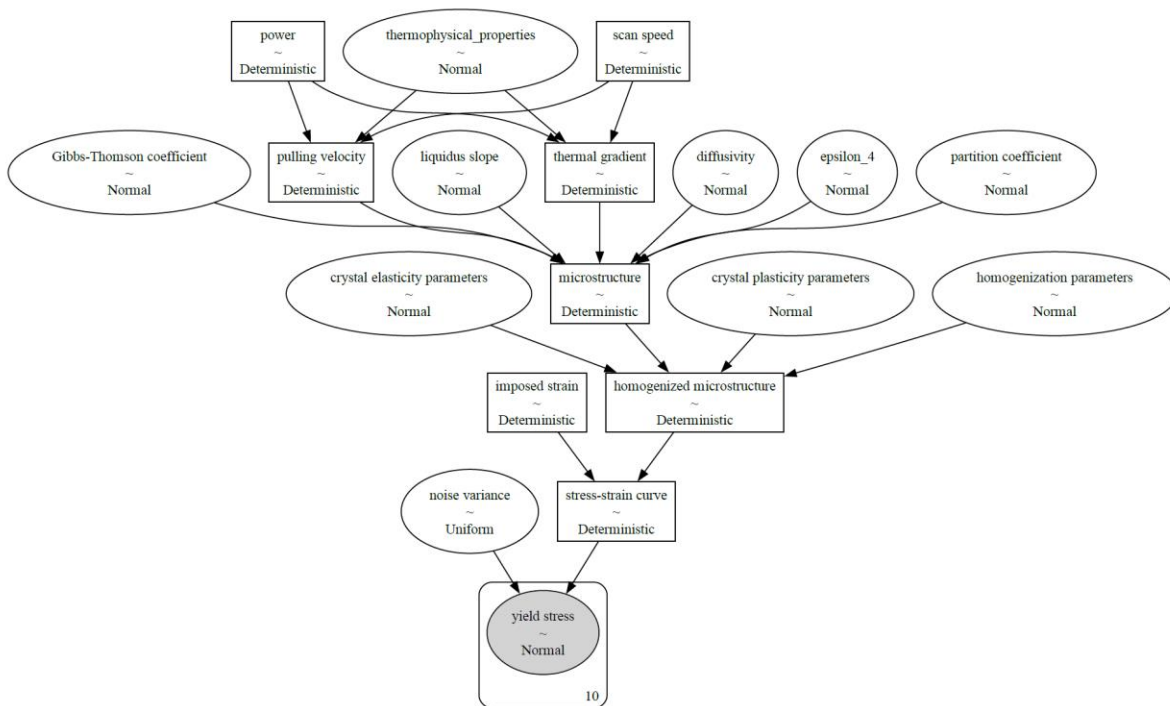


Figure 43: A notional directed acyclic graph showing uncertainty propagation for laser powder bed fusion from processing to mechanical properties.

CALPHAD as an example of a technique requiring UQ

Receiving more attention in the literature recently is UQ for CALPHAD techniques. While CALPHAD software often outputs phase diagram with defined lines and materials constants without uncertainty reported, this is ostensibly an incomplete understanding of the results from the method. Instead, recent work by CHiMaD and

NASA/JPL [149], [150] demonstrates, as in Figure 44, how uncertainty is truly present in CALPHAD results – for example, phase diagrams contain inherent uncertainty expressed graphically as “fuzziness” along the phase boundaries. Expressing such uncertainty reinforces the need for more accurate and precise thermophysical properties measurements and modeling, which can reduce the uncertainty in CALPHAD results and thus reduce the uncertainty propagated to longer length scales.

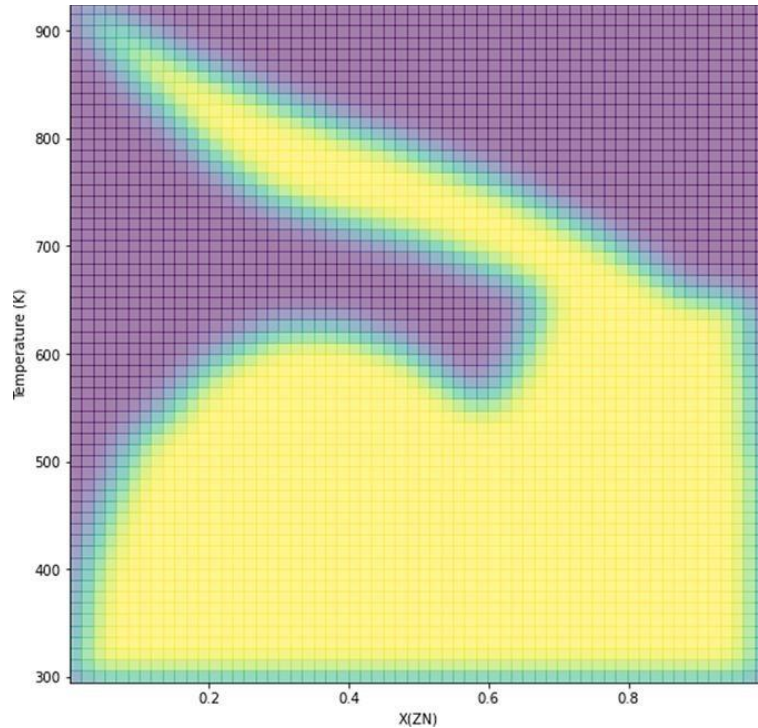


Figure 44: Probability map of the aluminum-Zn phase diagram based on likelihood of the FCC phase existing, where light represents likely and dark represents unlikely [150]. Reprinted from R. Otis, “Uncertainty reduction and quantification in computational thermodynamics,” *Computational Materials Science*, vol. 212, p. 111590, Sep. 2022, doi: [10.1016/j.commatsci.2022.111590](https://doi.org/10.1016/j.commatsci.2022.111590) with permission from Elsevier.

5.2. Future and BPS role

Modeling methods & tools across multiple length scales require quantification and reduction in uncertainty. BPS-funded flight experiments, both historical and current, can provide the benchmark datasets useful to not only reduce uncertainty in inputs to models but also the reduce the uncertainty in the models themselves by providing anchoring data points to refine model assumptions, formulations, and parameters. Two examples are now provided to indicate the value of thermophysical property measurements and solidification experiments to uncertainty quantification & reduction for ICME, which BPS historical and current datasets can support.

6. Conclusion: accomplishments, finding, and recommendations

This study was a beginning, necessarily limited by labor and time, and does not address all possible avenues or methods. The focused work is meant to convey a sense of what is and what can be done provided sufficient attention, effort, funding, and time. Despite these limitations, this study group was able to:

- explore the motivation for BPS to continue engagement within the ICME community with a focus on thermophysical properties and solidification dynamics in microgravity
- identify several experimental benchmark cases to compare modeling results against
- identify relevant modeling tools
- engage with the developers of such tools

- investigate required computing architectures and resources
- outline the means and necessity of uncertainty quantification and reduction
- discuss how thermophysical properties and solidification simulations are situated within the ICME ecosystem, and
- indicate how scale bridging using thermodynamical and mesoscale plasticity models offers a route to full-up computational simulation of realistic materials.

Initial results from comparisons of research and community PF codes along with their performance on various architectures have also been shared. This shows that a synergistic approach using computational methods combined with experimental validation provides valuable information on quantification of statistical variability in model predictions, thus reducing risk and assessing safety margins. This uncertainty reduction in both model inputs and modeling tools themselves will bring BPS-supported ICME datasets and models from investigational science to practical use in in-space exploration sustainability as with the MATRICES campaign and in industrial manufacturing on Earth.

6.1. Accomplishments arising from this study group

1. Convened experts from academia, Agency, & industry; across all length scales from atomistic to macroscale; computational and experimental backgrounds

This study converged experts from academia (Northeastern, Northwestern, and Tufts University), from the Agency (LaRC and MSFC), and industry (CFDRC). Experimentalists and modelers from the atomistic (thermophysical property measurements, density functional theory/DFT, etc.) to microscale (solidification, fluid coupling) to mesoscale (crystal plasticity) and more (calculation of phase diagrams/CALPHAD, uncertainty quantification, etc.) contributed to the technical content and recommendations. While not exhaustive, this represented a broad swathe of BPS-relevant experience and expertise in microgravity materials science and was suited to provide an overview of the ICME state-of-play and future path with respect to BPS.

2. Produced the present survey report describing flight experiments and BPS unique capabilities & role in the broader ICME context

In fiscal year 2023 (September 2023), a survey report highlighting several microgravity materials science experiments and computational tools relevant to ICME was released internally to BPS. The experiments reviewed were both heritage and current BPS-funded and BPS-relevant studies, mostly focused on solidification to demonstrate the need for benchmark experiments that provide validation datasets for those computational models. The computational tools reviewed included both BPS-supported academic, research codes and community, open-source codes. This survey report formed the basis for this final report.

3. Exercised BPS-supported academic research codes against BPS flight datasets and benchmarked against open-source or commercial codes widely used in ICME community

As extensively detailed in Section 3.2, BPS-supported academic research solidification codes using the PF method – previously validated against datasets from microgravity materials science flight experiments – were compared to two commonly used community open-source codes. The influences of differing code architecture (PRISMS-PF) and mathematical formulation (MOOSE) were shown, with the need for parameters taken from flight experiments and opportunities for future development indicated. Additional comparisons of academic research codes, community open-source codes, and validation datasets derived from flight experiments were briefly conducted for thermophysical properties in Section 2.2 and for fluid dynamics during solidification in Section 3.2.

4. Interacted with developers of open-source codes (PRISMS-PF, MOOSE); yielded extensions of codes – alternate formulations that support validation datasets, treadmill simulation, and 3-dimensional capability

Several of the academic and industry researchers in this study group leveraged their collegial relationships with the developers of two community, open-source PF codes, MOOSE and PRISMS-PF, to compare those codes against BPS-supported academic research codes and to benchmark against validation datasets from flight experiments

(Section 3.2). Beyond demonstrating the ability of community, open-source codes to converge with BPS-supported academic research codes, these interactions resulted in definite enhancements to said community, open-source codes. The MOOSE developers are looking to implement the dilute alloy solidification approach of Echebarria et al. [53] in addition to their existing Grand Potential formulation, which would enable more straightforward comparison with GPU-PF and PRISMS-PF. The PRISMS-PF developers were able to achieve convergence of their 3-dimensional version with GPU-PF, demonstrating the utility of BPS support of such PF codes for solidification modeling. Further interaction with the PRISMS-PF developers resulted in the addition of a treadmill mode, easing comparison with GPU-PF and other PF codes.

5. Implemented PRISMS-PF (CPU-bound) and GPU-PF (GPU-bound) on NASA supercomputer

As detailed in Section 3.2, the NASA Advanced Supercomputing (NAS) facility available through the NASA High-End Computing Capability Portfolio has both CPU and GPU compute resources available. Through an out-of-cycle allocation sponsored by the NASA Science Mission Directorate, the study group ran academic research codes (DNN and GPU-PF) and community, open-source codes (PRISMS-PF) on NAS hardware.

6.2. Findings

1. BPS datasets are *foundational* anchoring/benchmark datasets used to validate modeling efforts

The accomplishments would not have been feasible without validation datasets from microgravity materials science flight experiments. Thermophysical properties measurements and dendritic solidification experiments anchored computational models, while similar efforts are possible for coarsening, columnar-to-equiaxed transition, etc. The repository of high-quality microgravity materials science datasets supported by BPS and stored in PSI is an unparalleled resource for validating computational models now and into the future.

2. Interaction with code developers using BPS/microgravity datasets for validation *is critical* for continued progress

Within a few months, this study group had a substantial impact on enhancing and validating community, open-source codes such as MOOSE and PRISMS-PF. Besides making the validation datasets available, the two-way communication between code developer and scientific experts was necessary for rapidly iterating and demonstrating these new capabilities and validations. Understanding both the computational and experimental aspects of ICME is required to make best use of the flight experimental datasets and expertise that BPS supports.

3. Generation of useful meso/macro-scale property models via scale bridging *requires* accurate, precise thermophysical properties and solidification- & fluids-coupled data & models emphasized by the microgravity environment

As shown most acutely by a directed acyclic graph (Figure 43), longer length scale and higher order models depend on lower length scale models and data. Thus, any errors or uncertainties in the lower length scales will propagate up to the longer length scales, potentially invalidating them or causing a lack of convergence. Refining lower length scale data and models is thus needed to fully implement the highest fidelity property and performance models. Fortunately, the microgravity environment provides an ideal setting to perform such experiments and thus to provide validation datasets for more accurate and precise models.

4. Computational infrastructure is rapidly evolving from CPU-bound to GPU, increasing throughput and enabling increasingly useful modeling efforts.

The implementation of GPU-PF and PRISMS-PF on NAS hardware demonstrates that such codes can take advantage of world-class supercomputing resources, especially that of rapidly advancing GPU resources. Currently, multi-GPU academic research codes used to model BPS datasets have been developed for a single compute node, limiting the number of GPUs used. For example, the NASA Advanced Supercomputing facilities recently added the Cabeus cluster of one hundred Nvidia A100 GPUs which has either four or eight GPUs per node. If such multi-GPU

codes could run on multiple compute nodes, then this could enable simulating entire sample volumes or substantially increasing throughput.

5. Models can be made relevant to industry by reducing and reporting uncertainty

Uncertainty quantification requires knowledge of both the accuracy and precision of relevant model inputs and parameters, the identification of which requires flight experimental data. The same data can also validate said models. Once industry can be assured that a model is reliable and its uncertainty properly constrained, then it will be more straightforward for them to make greater use of ICME tools to enhance their productivity and to mitigate risk.

6.3. Recommendations

RECOMMENDATION 1: Accelerate flight experiments to collect critical validation datasets to:
RECOMMENDATION 1.A: Quantify and drive down uncertainty in inputs and models for engineering-relevant data to:

Perform validation assessments of specific computational models using available flight datasets, identifying gaps in said datasets and models. Follow-on work to identify where validation datasets are incomplete or could be improved will identify which flight experiments are most needed to provide anchoring data for computational models. The validation assessment is not a new process in the broader world of computational models & engineering; computational fluid dynamics formalized the process with the 1998 AIAA G-077 report [151] and NASA employs verification & validation processes through NASA-STD-7009 [152]. What is new would be the rigorous applications of these validation assessment to microgravity materials science, highlighting which gaps are most salient on a model-by-model and length-scale basis.

Specific to the BPS flight experiments described in this report, a combined theoretical-computational effort reviewing the results of previous experiments in coarsening, columnar-to-equiaxed transition, directional solidification, and measurement of thermophysical properties would yield a more precise understanding of remaining unknowns and uncertainties shown by these solidification and microstructural experiments. A similar effort could be made for thermophysical property models and experiments.

Conduct materials property and processing experiments unique to microgravity to collect validation datasets. Based on gaps identified in validation assessment, flight experiments can be developed and flown to collect the relevant data to be incorporated back into computational modeling efforts.

Enable progression of experiments from ground to parabolic to suborbital to on-orbit. At each step of increasing complexity and effort, the most representative data can be collected to ensure that computational models can properly incorporate said data. The fundamental materials science mechanisms involved can be finely tuned by each successive level of experimentation.

Validate materials property and processing computational and theoretical models. These new flight datasets based on specifically identified and well-defined gaps would be invaluable to achieving greater levels of model validation and thus confidence in their ability to represent materials processes, finally enabling a virtual toolbox to design and predict materials performance across all length scales.

RECOMMENDATION 1.B: Champion “Can Do” science with existing ground and flight facilities and hardware

To maximize scientific output from the rapidly closing window of opportunity for microgravity materials science on the ISS, BPS should implement an aggressive plan to use existing facilities and flight-qualified equipment to close discrete, clear gaps in the materials science domain indicated by previous experimentation. First, these gaps must be identified by the validation assessment of RECOMMENDATION 1.A. Then the currently available experimental resources can be mapped with gap closures. This activity is an ideal follow-on for the present study.

entities). For example, both LaRC and MSFC were heavily involved in this report. However, the well-established groups performing ICME work at Ames Research Center and Glenn Research Center should be more involved in a broader, follow-on effort. NASA opportunities may, for example, include harmonizing with the EPSCoR Research Infrastructure Improvement program to ensure ICME researchers are eligible for such awards. The recommendation of Vision 2040 [2] for an inter-agency ICME technical working group is repeated with added urgency as the need for useful computational models of materials increases. There is certainly a convergence of interests for ICME across the federal government, especially for additive manufacturing. For instance, the Department of Energy (DOE) has provided funding for PRISMS-PF. BPS could participate in a combined technical endeavor with the DOE, National Science Foundation, National Institute of Standards and Technology, and other interested parties, greatly advance ICME with BPS bringing valuable datasets, codes, and expertise. The Materials Genome Initiative is on the vanguard of ICME-relevant computational materials research [154] and is one route to further connecting with the ICME community. One early example of this is the Physical Science Informatics open-science database that publicly shares BPS flight datasets.

RECOMMENDATION 2.C: Support the transition of legacy codes to modern architectures with enhanced capabilities and ease-of-maintenance (e.g. CPU-bound to GPU-bound, multi-GPU multi-node)

Evident from the example of GPU-PF and PRISMS-PF during this report is that the transition from CPU-bound to GPU-bound computation drastically increases model throughput and speed. This will be especially needed as model domains and dimensionality increase – going from two to three dimensions and from simulating a cluster of dendrites to substantial volumes approaching that of an entire sample cartridge. While current GPU-bound codes are limited to one compute node controlling multiple GPUs, further development could see such codes expanded to allow multiple compute nodes to each control multiple GPUs, leading to nearly unlimited scaling of throughput. BPS should actively support the development of atomistic, solidification, and mesoscale codes – whether academic or community – that yield computational models relevant to microgravity materials science and can be transition to multi-node, multi-GPU capabilities.

RECOMMENDATION 2.D: Explore opportunities to employ cognitive (i.e. AI/ML) computing rather than traditional algorithmic (von Neumann) computing

Section 2.2 in this report described the use of a physically informed neural network that used training datasets from computationally intensive models like DFT. BPS should consider how datasets from computation and flight experiments could be used to train artificially intelligent or machine learning models, which could reduce the time and expense associated with predicting materials properties and the like from these datasets. However, BPS is not the lead on cognitive computing capabilities at NASA and will have to work in partnership with internal and external efforts to understand the benefits and drawbacks of this emerging technology.

RECOMMENDATION 2.E: Support/mentor research teams across multiple academic partners and NASA Centers

BPS should develop NRAs and other funding mechanisms to sustainably support and expand the BPS ICME community. This includes both internal and external research teams. One example already underway is the recruiting of a postdoctoral researcher funded by BPS through the NASA Postdoctoral Program. This postdoc will focus on exploring mesoscale (grain structure) models of welding, accounting for the unique space environment.

These recommendations have been categorized in Table 3 by the level of engagement any BPS-associated ICME effort should consider according to those categories suggested in the most recent Decadal Survey [16]. BPS ICME should *lead* in direct, actionable fundamental materials science investigations (1.A, 1.B, and 1.C) and in supporting intermural & extramural ICME teams (2.E) to collect, analyze, and implement computational models based on collected flight datasets. BPS ICME should *collaborate* on experiments-of-opportunity with other NASA Mission Directorates (1.D) and on maturing the ICME ecosystem using BPS heritage codes and datasets (2.A, 2.B, and 2.C). BPS ICME should *watch* the development of cognitive computing (2.D), recognizing that it is a rapidly developing arena offering substantial opportunities for accelerating materials science. BPS ICME should also *watch* detailed

studies of future flight facilities, including commercial LEO destinations, until more certainty in their timeframe and capabilities becomes available.

Table 3: Recommendations categorized by level of BPS engagement.

Recommendation	Brief description	Action
1.A	Validation assessment and conducting gap-closing fundamental microgravity material science	Lead
1.B	“Can Do” science	Lead
1.C	Next-generation materials science experiments	Lead & Collaborate
1.D	Experiments-of-opportunity	Collaborate
1.E	Future experimental platforms	Watch
2.A	Leverage open-source codes	Collaborate
2.B	Become visible partner in ICME community	Collaborate
2.C	Transitioning and enhancing legacy codes	Collaborate
2.D	Cognitive computing	Watch
2.E	Support multi-partner, multi-Center research teams	Lead

Bibliography

- [1] M. Kumar, R. Napolitano, and S. Pathak, “Structure and Properties of the Terrestrial vs. Microgravity Solders under Extremes of Elevated and Cryo Temperatures,” presented at the PSI User Group, Mar. 13, 2024.
- [2] X. Liu, D. Furrer, J. Kusters, and J. Holmes, “Vision 2040: A Roadmap for Integrated, Multiscale Modeling and Simulation of Materials and Systems,” Pratt & Whitney, East Hartford, CT, Contractor report NASA/CR--2018-219771, Mar. 2018. Accessed: Aug. 18, 2023. [Online]. Available: <https://ntrs.nasa.gov/citations/20180002010>
- [3] T. Pinomaa, I. Yashchuk, M. Lindroos, T. Andersson, N. Provatas, and A. Laukkanen, “Process-Structure-Properties-Performance Modeling for Selective Laser Melting,” *Metals*, vol. 9, no. 11, Art. no. 11, Nov. 2019, doi: 10.3390/met9111138.
- [4] J. J. de Pablo *et al.*, “New frontiers for the materials genome initiative,” *Npj Comput. Mater.*, vol. 5, no. 1, pp. 1–23, Apr. 2019, doi: 10.1038/s41524-019-0173-4.
- [5] M. S. James, S. Ghosh, E. Glaessgen, A. Rollett, and J. Vickers, “Accelerating Additive Manufacturing Certification with Model-Based Tools,” presented at the International Conference on Advanced Manufacturing 2023, Washington, DC, Oct. 2023. Accessed: Jun. 21, 2024. [Online]. Available: <https://ntrs.nasa.gov/citations/20230014537>
- [6] The Minerals, Metals & Materials Society, “Modeling Across Scales: A Roadmapping Study for Connecting Materials Models and Simulations Across Length and Time Scales,” The Minerals, Metals & Materials Society, 2015. doi: 10.7449/multiscale_1.
- [7] S. Soto-Medina, B. Rijal, A. K. Sachdev, R. G. Hennig, and M. V. Manuel, “Increasing the composition range of a novel τ 11-Al4Fe1.7Si alloy with additions of Mn,” *Intermetallics*, vol. 145, p. 107499, Jun. 2022, doi: 10.1016/j.intermet.2022.107499.
- [8] M. V. Manuel and R. Hennig, “Lightweight High-Temperature Alloys Based on the AlFeSi System,” University of Florida, Gainesville, FL, Final research performance progress report DOE-UF-0007742-1, Jun. 2021. doi: 10.2172/1806575.
- [9] A. Jain *et al.*, “Commentary: The Materials Project: A materials genome approach to accelerating materials innovation,” *APL Mater.*, vol. 1, no. 1, p. 011002, Jul. 2013, doi: 10.1063/1.4812323.
- [10] T. Keller *et al.*, “Application of finite element, phase-field, and CALPHAD-based methods to additive manufacturing of Ni-based superalloys,” *Acta Mater.*, vol. 139, pp. 244–253, Oct. 2017, doi: 10.1016/j.actamat.2017.05.003.
- [11] V. Prithivirajan and M. D. Sangid, “Examining metrics for fatigue life predictions of additively manufactured IN718 via crystal plasticity modeling including the role of simulation volume and microstructural constraints,” *Mater. Sci. Eng. A*, vol. 783, p. 139312, May 2020, doi: 10.1016/j.msea.2020.139312.
- [12] “White Paper #06: Materials Science,” European Space Agency, White paper #06, 2021.
- [13] Committee on Integrated Computational Materials Engineering, National Research Council of the National Academies, *Integrated Computational Materials Engineering: A Transformational Discipline for Improved Competitiveness and National Security*. Washington, DC: National Academies Press, 2008. doi: 10.17226/12199.
- [14] S. A. Nabavizadeh, R. Lenart, M. Eshraghi, S. D. Felicelli, S. N. Tewari, and R. N. Grugel, “Dendritic solidification of Succinonitrile-0.24 wt% water alloy: A comparison with microgravity experiments for validating dendrite tip velocity,” *Acta Astronaut.*, vol. 175, pp. 163–173, Oct. 2020, <https://doi.org/10.1016/j.actaastro.2020.05.059>.
- [15] S. A. Nabavizadeh, S. Upadhyay, M. Eshraghi, S. D. Felicelli, S. N. Tewari, and R. N. Grugel, “Spurious grain formation due to Marangoni convection during directional solidification of alloys in μ -g environment of International Space Station,” *J. Cryst. Growth*, vol. 574, p. 126334, Nov. 2021, <https://doi.org/10.1016/j.jcrysgro.2021.126334>.

- [16] E. National Academies of Sciences, *Thriving in Space: Ensuring the Future of Biological and Physical Sciences Research: A Decadal Survey for 2023-2032*. 2023. doi: 10.17226/26750.
- [17] G. B. Olson, “Beyond discovery: design for a new material world,” *Calphad*, vol. 25, no. 2, pp. 175–190, Jun. 2001, doi: 10.1016/S0364-5916(01)00041-4.
- [18] W. Xiong and G. B. Olson, “Cybermaterials: materials by design and accelerated insertion of materials,” *Npj Comput. Mater.*, vol. 2, no. 1, p. 15009, Feb. 2016, doi: 10.1038/npjcompumats.2015.9.
- [19] M. E. Glicksman, M. B. Koss, and E. A. Winsa, “The chronology of a microgravity spaoeflight experiment: IDGE,” *JOM*, vol. 47, no. 8, pp. 49–54, Aug. 1995, doi: 10.1007/BF03221460.
- [20] T. J. Williams and C. Beckermann, “Benchmark Al-Cu Solidification Experiments in Microgravity and on Earth,” *Metall. Mater. Trans. A*, vol. 54, no. 2, pp. 405–422, Feb. 2023, doi: 10.1007/s11661-022-06909-6.
- [21] F. L. Mota, M. Medjkoune, L. S. Littles, A. Karma, and N. Bergeon, “Solidification furnace for *in situ* observation of bulk transparent systems and image analysis methods,” *Rev. Sci. Instrum.*, vol. 94, no. 6, p. 065111, Jun. 2023, doi: 10.1063/5.0150391.
- [22] T. Cool and P. W. Voorhees, “Dendrite fragmentation: an experiment-driven simulation,” *Philos. Trans. R. Soc. Math. Phys. Eng. Sci.*, vol. 376, no. 2113, p. 20170213, Jan. 2018, doi: 10.1098/rsta.2017.0213.
- [23] National Aeronautics and Space Administration, “Physical Sciences Informatics (PSI).” PSI, <https://psi.ndc.nasa.gov/app/>, Apr. 29, 2020. Accessed: Sep. 06, 2023. [Online]. Available: <http://www.nasa.gov/PSI>
- [24] J. Nawer, S. Gossé, and D. M. Matson, “Tracking Evaporation During Levitation Processing of Nickel-Based Superalloys on the ISS,” *JOM*, vol. 72, no. 9, pp. 3132–3139, Sep. 2020, doi: 10.1007/s11837-020-04256-8.
- [25] M. Mohr, R. Wunderlich, R. Novakovic, E. Ricci, and H.-J. Fecht, “Precise Measurements of Thermophysical Properties of Liquid Ti–6Al–4V (Ti64) Alloy On Board the International Space Station,” *Adv. Eng. Mater.*, vol. 22, no. 7, p. 2000169, Jul. 2020, doi: 10.1002/adem.202000169.
- [26] M. Mohr, R. Wunderlich, and H.-J. Fecht, “Thermophysical Properties of Titanium Alloys,” in *Metallurgy in Space*, H.-J. Fecht and M. Mohr, Eds., in The Minerals, Metals & Materials Series. , Cham: Springer International Publishing, 2022, pp. 357–375. doi: 10.1007/978-3-030-89784-0_16.
- [27] M. Mohr and H.-J. Fecht, “Investigating Thermophysical Properties Under Microgravity: A Review,” *Adv. Eng. Mater.*, vol. 23, no. 2, p. 2001223, Feb. 2021, doi: 10.1002/adem.202001223.
- [28] M. Mohr *et al.*, “Electromagnetic levitation containerless processing of metallic materials in microgravity: thermophysical properties,” *Npj Microgravity*, vol. 9, no. 1, Art. no. 1, May 2023, doi: 10.1038/s41526-023-00281-4.
- [29] W.-K. Rhim *et al.*, “An electrostatic levitator for high-temperature containerless materials processing in 1-g,” *Rev. Sci. Instrum.*, vol. 64, no. 10, pp. 2961–2970, Oct. 1993, doi: 10.1063/1.1144475.
- [30] J. Nawer *et al.*, “A quantitative comparison of thermophysical property measurement of CMSX-4® Plus (SLS) in microgravity and terrestrial environments,” *High Temp.-High Press.*, vol. 52, no. 3–4, pp. 323–339, 2023, doi: 10.32908/hthp.v52.1407.
- [31] D. M. Matson *et al.*, “Use of Thermophysical Properties to Select and Control Convection During Rapid Solidification of Steel Alloys Using Electromagnetic Levitation on the Space Station,” *JOM*, vol. 69, no. 8, pp. 1311–1318, Aug. 2017, doi: 10.1007/s11837-017-2396-5.
- [32] R. W. Hyers, “Fluid flow effects in levitated droplets,” *Meas. Sci. Technol.*, vol. 16, no. 2, pp. 394–401, Feb. 2005, doi: 10.1088/0957-0233/16/2/010.
- [33] J. Lee, D. M. Matson, S. Binder, M. Kolbe, D. Herlach, and R. W. Hyers, “Magnetohydrodynamic Modeling and Experimental Validation of Convection Inside Electromagnetically Levitated Co-Cu Droplets,” *Metall. Mater. Trans. B*, vol. 45, no. 3, pp. 1018–1023, Jun. 2014, doi: 10.1007/s11663-013-9995-5.

- [34] N. Brosius, K. Ward, S. Matsumoto, M. SanSoucie, and R. Narayanan, “Faraday forcing of high-temperature levitated liquid metal drops for the measurement of surface tension,” *Npj Microgravity*, vol. 4, no. 1, Art. no. 1, May 2018, doi: 10.1038/s41526-018-0044-1.
- [35] J. Brillo, M. Watanabe, and H. Fukuyama, “Relation between excess volume, excess free energy and isothermal compressibility in liquid alloys,” *J. Mol. Liq.*, vol. 326, p. 114395, Mar. 2021, doi: 10.1016/j.molliq.2020.114395.
- [36] X. Xiao and J. Brillo, “Surface tension of liquid Fe-Ni, Fe-Cr, and Ni-Cr with physics-informed statistical modeling on the influence of oxygen content,” *J. Mol. Liq.*, vol. 360, p. 119599, Aug. 2022, doi: 10.1016/j.molliq.2022.119599.
- [37] Y. Mishin, D. Farkas, M. J. Mehl, and D. A. Papaconstantopoulos, “Interatomic potentials for monoatomic metals from experimental data and ab initio calculations,” *Phys. Rev. B*, vol. 59, no. 5, pp. 3393–3407, Feb. 1999, doi: 10.1103/PhysRevB.59.3393.
- [38] M. S. Daw and M. I. Baskes, “Embedded-atom method: Derivation and application to impurities, surfaces, and other defects in metals,” *Phys. Rev. B*, vol. 29, no. 12, pp. 6443–6453, Jun. 1984, doi: 10.1103/PhysRevB.29.6443.
- [39] T. B. Blank, S. D. Brown, A. W. Calhoun, and D. J. Doren, “Neural network models of potential energy surfaces,” *J. Chem. Phys.*, vol. 103, no. 10, pp. 4129–4137, Sep. 1995, doi: 10.1063/1.469597.
- [40] S. Chmiela, H. E. Sauceda, K.-R. Müller, and A. Tkatchenko, “Towards exact molecular dynamics simulations with machine-learned force fields,” *Nat. Commun.*, vol. 9, no. 1, p. 3887, Sep. 2018, doi: 10.1038/s41467-018-06169-2.
- [41] J. Behler and M. Parrinello, “Generalized Neural-Network Representation of High-Dimensional Potential-Energy Surfaces,” *Phys. Rev. Lett.*, vol. 98, no. 14, p. 146401, Apr. 2007, doi: 10.1103/PhysRevLett.98.146401.
- [42] Z. Li, J. R. Kermode, and A. De Vita, “Molecular Dynamics with On-the-Fly Machine Learning of Quantum-Mechanical Forces,” *Phys. Rev. Lett.*, vol. 114, no. 9, p. 096405, Mar. 2015, doi: 10.1103/PhysRevLett.114.096405.
- [43] G. P. P. Pun, V. Yamakov, J. Hickman, E. H. Glaessgen, and Y. Mishin, “Development of a general-purpose machine-learning interatomic potential for aluminum by the physically informed neural network method,” *Phys. Rev. Mater.*, vol. 4, no. 11, p. 113807, Nov. 2020, doi: 10.1103/PhysRevMaterials.4.113807.
- [44] J. J. Hoyt, M. Asta, and A. Karma, “Method for Computing the Anisotropy of the Solid-Liquid Interfacial Free Energy,” *Phys. Rev. Lett.*, vol. 86, no. 24, pp. 5530–5533, Jun. 2001, doi: 10.1103/PhysRevLett.86.5530.
- [45] J. Hoyt, “Atomistic and continuum modeling of dendritic solidification,” *Mater. Sci. Eng. R Rep.*, vol. 41, no. 6, pp. 121–163, Sep. 2003, doi: 10.1016/S0927-796X(03)00036-6.
- [46] M. Asta *et al.*, “Solidification microstructures and solid-state parallels: Recent developments, future directions,” *Acta Mater.*, vol. 57, no. 4, pp. 941–971, Feb. 2009, doi: 10.1016/j.actamat.2008.10.020.
- [47] A. Karma and D. Tourret, “Atomistic to continuum modeling of solidification microstructures,” *Curr. Opin. Solid State Mater. Sci.*, vol. 20, no. 1, pp. 25–36, Feb. 2016, doi: 10.1016/j.cossms.2015.09.001.
- [48] A. Karma, Z. T. Trautt, and Y. Mishin, “Relationship between Equilibrium Fluctuations and Shear-Coupled Motion of Grain Boundaries,” *Phys. Rev. Lett.*, vol. 109, no. 9, p. 095501, Aug. 2012, doi: 10.1103/PhysRevLett.109.095501.
- [49] *Parallel Grand Canonical Monte Carlo Simulation Code - ParaGrandMC*. FORTRAN 2004. NASA/LaRC, Hampton, VA. Accessed: Mar. 22, 2024. [Linux]. Available: <https://software.nasa.gov/software/LAR-19893-1>
- [50] B. Sundman, N. Dupin, and B. Hallstedt, “Algorithms useful for calculating multi-component equilibria, phase diagrams and other kinds of diagrams,” *Calphad*, vol. 75, p. 102330, Dec. 2021, doi: 10.1016/j.calphad.2021.102330.

- [51] G. Guillemot, O. Senninger, C. A. Hareland, P. W. Voorhees, and C.-A. Gandin, “Thermodynamic coupling in the computation of dendrite growth kinetics for multicomponent alloys,” *Calphad*, vol. 77, p. 102429, Jun. 2022, doi: 10.1016/j.calphad.2022.102429.
- [52] G. LINDWALL *et al.*, “Simulation of TTT Curves for Additively Manufactured Inconel 625,” *Metall. Mater. Trans. Phys. Metall. Mater. Sci.*, vol. 50, no. 1, p. 10.1007/s11661-018-4959-7, 2019, doi: 10.1007/s11661-018-4959-7.
- [53] B. Echebarria, R. Folch, A. Karma, and M. Plapp, “Quantitative phase-field model of alloy solidification,” *Phys. Rev. E*, vol. 70, no. 6, p. 061604, Dec. 2004, doi: 10.1103/PhysRevE.70.061604.
- [54] N. Cusato, S. A. Nabavizadeh, and M. Eshraghi, “A Review of Large-Scale Simulations of Microstructural Evolution during Alloy Solidification,” *Metals*, vol. 13, no. 7, Art. no. 7, Jul. 2023, doi: 10.3390/met13071169.
- [55] M. E. Glicksman, M. B. Koss, L. T. Bushnell, J. C. Lacombe, and E. A. Winsa, “Dendritic Growth in Terrestrial and Microgravity Conditions,” *MRS Proc.*, vol. 367, p. 13, 1994, doi: 10.1557/PROC-367-13.
- [56] J. LaCombe, C. Giummarra, M. Koss, J. Frei, A. Lupulescu, and M. Glicksman, “Sidebranch characteristics of pivalic acid dendrites grown under terrestrial-gravity and microgravity conditions,” in *40th AIAA Aerospace Sciences Meeting & Exhibit*, American Institute of Aeronautics and Astronautics. doi: 10.2514/6.2002-456.
- [57] M. Plapp and A. Karma, “Multiscale Random-Walk Algorithm for Simulating Interfacial Pattern Formation,” *Phys. Rev. Lett.*, vol. 84, no. 8, pp. 1740–1743, Feb. 2000, doi: 10.1103/PhysRevLett.84.1740.
- [58] A. Karma and W.-J. Rappel, “Quantitative phase-field modeling of dendritic growth in two and three dimensions,” *Phys. Rev. E*, vol. 57, no. 4, pp. 4323–4349, Apr. 1998, doi: 10.1103/PhysRevE.57.4323.
- [59] M. Plapp and A. Karma, “Multiscale Finite-Difference-Diffusion-Monte-Carlo Method for Simulating Dendritic Solidification,” *J. Comput. Phys.*, vol. 165, no. 2, pp. 592–619, Dec. 2000, doi: 10.1006/jcph.2000.6634.
- [60] A. Karma, Y. H. Lee, and M. Plapp, “Three-dimensional dendrite-tip morphology at low undercooling,” *Phys. Rev. E*, vol. 61, no. 4, pp. 3996–4006, Apr. 2000, doi: 10.1103/PhysRevE.61.3996.
- [61] F. L. Mota, K. Ji, L. S. Littles, R. Trivedi, A. Karma, and N. Bergeon, “Influence of macroscopic interface curvature on dendritic patterns during directional solidification of bulk samples: Experimental and phase-field studies,” *Acta Mater.*, vol. 250, p. 118849, May 2023, <https://doi.org/10.1016/j.actamat.2023.118849>.
- [62] Ch.-A. Gandin and M. Rappaz, “A coupled finite element-cellular automaton model for the prediction of dendritic grain structures in solidification processes,” *Acta Metall. Mater.*, vol. 42, no. 7, pp. 2233–2246, Jul. 1994, doi: 10.1016/0956-7151(94)90302-6.
- [63] Ch.-A. Gandin and M. Rappaz, “A 3D Cellular Automaton algorithm for the prediction of dendritic grain growth,” *Acta Mater.*, vol. 45, no. 5, pp. 2187–2195, May 1997, doi: 10.1016/S1359-6454(96)00303-5.
- [64] D. Tournet and A. Karma, “Multiscale dendritic needle network model of alloy solidification,” *Acta Mater.*, vol. 61, no. 17, pp. 6474–6491, Oct. 2013, doi: 10.1016/j.actamat.2013.07.026.
- [65] D. Tournet and A. Karma, “Three-dimensional dendritic needle network model for alloy solidification,” *Acta Mater.*, vol. 120, pp. 240–254, Nov. 2016, doi: 10.1016/j.actamat.2016.08.041.
- [66] P.-A. Geslin, C.-H. Chen, A. M. Tabrizi, and A. Karma, “Dendritic needle network modeling of the Columnar-to-Equiaxed transition. Part I: two dimensional formulation and comparison with theory,” *Acta Mater.*, vol. 202, pp. 42–54, Jan. 2021, doi: 10.1016/j.actamat.2020.10.009.
- [67] C.-H. Chen, A. M. Tabrizi, P.-A. Geslin, and A. Karma, “Dendritic needle network modeling of the Columnar-to-Equiaxed Transition. Part II: three dimensional formulation, implementation and

- comparison with experiments,” *Acta Mater.*, vol. 202, pp. 463–477, Jan. 2021, doi: 10.1016/j.actamat.2020.10.012.
- [68] G. Zimmermann *et al.*, “Columnar and Equiaxed Solidification of Al-7 wt.% Si Alloys in Reduced Gravity in the Framework of the CETSOL Project,” *JOM*, vol. 69, no. 8, pp. 1269–1279, Aug. 2017, doi: 10.1007/s11837-017-2397-4.
- [69] A. Pineau, G. Guillemot, D. Tournet, A. Karma, and Ch.-A. Gandin, “Growth competition between columnar dendritic grains – Cellular automaton versus phase field modeling,” *Acta Mater.*, vol. 155, pp. 286–301, Aug. 2018, doi: 10.1016/j.actamat.2018.05.032.
- [70] E. Dorari, K. Ji, G. Guillemot, C.-A. Gandin, and A. Karma, “Growth competition between columnar dendritic grains – The role of microstructural length scales,” *Acta Mater.*, vol. 223, p. 117395, Jan. 2022, doi: 10.1016/j.actamat.2021.117395.
- [71] L. Sturz, G. Zimmermann, and M. Hamacher, “In-situ observation of equiaxed dendritic growth and interaction in microgravity,” Jul. 2017.
- [72] L. Sturz, M. Wu, G. Zimmermann, A. Ludwig, and M. Ahmadein, “Benchmark experiments and numerical modelling of the columnar-equiaxed dendritic growth in the transparent alloy Neopentylglycol-(d)Camphor,” *IOP Conf. Ser. Mater. Sci. Eng.*, vol. 84, no. 1, p. 012086, May 2015, doi: 10.1088/1757-899X/84/1/012086.
- [73] B. Echebarria, R. Folch, A. Karma, and M. Plapp, “Quantitative phase-field model of alloy solidification,” *Phys. Rev. E*, vol. 70, no. 6, p. 061604, Dec. 2004, doi: 10.1103/PhysRevE.70.061604.
- [74] L. K. Aagesen, J. L. Fife, E. M. Lauridsen, and P. W. Voorhees, “The evolution of interfacial morphology during coarsening: A comparison between 4D experiments and phase-field simulations,” *Scr. Mater.*, vol. 64, no. 5, pp. 394–397, Mar. 2011, doi: 10.1016/j.scriptamat.2010.10.040.
- [75] G. Zimmermann, U. Müller, and S. H. Davis, “Bénard convection in binary mixtures with Soret effects and solidification,” *J. Fluid Mech.*, vol. 238, pp. 657–682, May 1992, doi: 10.1017/S002211209200185X.
- [76] S. Van Vaerenbergh, S. R. Coriell, and G. B. McFadden, “Morphological stability of a binary alloy: thermodiffusion and temperature-dependent diffusivity,” *J. Cryst. Growth*, vol. 223, no. 4, pp. 565–572, Mar. 2001, doi: 10.1016/S0022-0248(01)00620-0.
- [77] V. Timchenko, R. Bennacer, E. Leonardi, and G. de V. Davis, “The influence of the Soret effect on transient solidification of alloys in a horizontal Bridgman apparatus,” presented at the International Heat Transfer Conference 12, Begel House Inc., 2002. doi: 10.1615/IHTC12.2240.
- [78] A. Yamamura, S. Sakane, M. Ohno, H. Yasuda, and T. Takaki, “Data assimilation with phase-field lattice Boltzmann method for dendrite growth with liquid flow and solid motion,” *Comput. Mater. Sci.*, vol. 215, p. 111776, Dec. 2022, doi: 10.1016/j.commatsci.2022.111776.
- [79] Y. Zhang, J. Zhou, Y. Yin, X. Ji, X. Shen, and Z. Guo, “Study on the solutal convection during dendrite growth of superalloy under directional solidification condition,” *J. Mater. Res. Technol.*, vol. 23, pp. 3916–3927, Mar. 2023, doi: 10.1016/j.jmrt.2023.02.042.
- [80] R. Rojas, T. Takaki, and M. Ohno, “A phase-field-lattice Boltzmann method for modeling motion and growth of a dendrite for binary alloy solidification in the presence of melt convection,” *J. Comput. Phys.*, vol. 298, pp. 29–40, Oct. 2015, doi: 10.1016/j.jcp.2015.05.045.
- [81] S. A. Nabavizadeh, M. Eshraghi, S. D. Felicelli, S. N. Tewari, and R. N. Grugel, “Effect of bubble-induced Marangoni convection on dendritic solidification,” *Int. J. Multiph. Flow*, vol. 116, pp. 137–152, Jul. 2019, doi: 10.1016/j.ijmultiphaseflow.2019.04.018.
- [82] B. Jelinek, M. Eshraghi, S. Felicelli, and J. F. Peters, “Large-scale parallel lattice Boltzmann–cellular automaton model of two-dimensional dendritic growth,” *Comput. Phys. Commun.*, vol. 185, no. 3, pp. 939–947, Mar. 2014, doi: 10.1016/j.cpc.2013.09.013.
- [83] T. Takaki, S. Sakane, M. Ohno, Y. Shibuta, and T. Aoki, “Large-scale phase-field lattice Boltzmann study on the effects of natural convection on dendrite morphology formed during directional

- solidification of a binary alloy,” *Comput. Mater. Sci.*, vol. 171, p. 109209, Jan. 2020, doi: 10.1016/j.commatsci.2019.109209.
- [84] A. Aalilija, “Numerical modelling of chill cooling of levitated steel melts solidified in the International Space Station,” Doctoral dissertation, Université Paris sciences et lettres, Paris, FR, 2020.
- [85] D. M. Matson *et al.*, “Electromagnetic levitation containerless processing of metallic materials in microgravity: rapid solidification,” *Npj Microgravity*, vol. 9, no. 1, p. 65, Aug. 2023, doi: 10.1038/s41526-023-00310-2.
- [86] S. Zhang, G. Guillemot, C.-A. Gandin, and M. Bellet, “A partitioned two-step solution algorithm for concurrent fluid flow and stress–strain numerical simulation in solidification processes,” *Comput. Methods Appl. Mech. Eng.*, vol. 356, pp. 294–324, Nov. 2019, doi: 10.1016/j.cma.2019.07.006.
- [87] A. Aalilija, C.-A. Gandin, and E. Hachem, “A simple and efficient numerical model for thermal contact resistance based on diffuse interface immersed boundary method,” *Int. J. Therm. Sci.*, vol. 166, p. 106817, Aug. 2021, doi: 10.1016/j.ijthermalsci.2020.106817.
- [88] V. Bojarevics and R. W. Hyers, “Levitated Liquid Dynamics in Reduced Gravity and Gravity-Compensating Magnetic Fields,” *JOM*, vol. 64, no. 9, pp. 1089–1096, Sep. 2012, doi: 10.1007/s11837-012-0417-y.
- [89] S. DeWitt, S. Rudraraju, D. Montiel, W. B. Andrews, and K. Thornton, “PRISMS-PF: A general framework for phase-field modeling with a matrix-free finite element method,” *Npj Comput. Mater.*, vol. 6, no. 1, Art. no. 1, Mar. 2020, doi: 10.1038/s41524-020-0298-5.
- [90] PRISMS Center, *PRISMS-PF*. [Online]. Available: <https://prisms-center.github.io/phaseField/>
- [91] C. J. Permann *et al.*, “MOOSE: Enabling massively parallel multiphysics simulation,” *SoftwareX*, vol. 11, p. 100430, Jan. 2020, doi: 10.1016/j.softx.2020.100430.
- [92] A. D. Lindsay *et al.*, “2.0 - MOOSE: Enabling massively parallel multiphysics simulation,” *SoftwareX*, vol. 20, p. 101202, Dec. 2022, doi: 10.1016/j.softx.2022.101202.
- [93] F. Kong, “GPUs and/or CUDA · idaholab/moose · Discussion #21152,” GitHub. Accessed: Sep. 05, 2023. [Online]. Available: <https://github.com/idaholab/moose/discussions/21152>
- [94] S. G. Kim, W. T. Kim, and T. Suzuki, “Phase-field model for binary alloys,” *Phys. Rev. E*, vol. 60, no. 6, pp. 7186–7197, Dec. 1999, doi: 10.1103/PhysRevE.60.7186.
- [95] D. Schwen, C. Jiang, and L. K. Aagesen, “A sublattice phase-field model for direct CALPHAD database coupling,” *Comput. Mater. Sci.*, vol. 195, p. 110466, Jul. 2021, doi: 10.1016/j.commatsci.2021.110466.
- [96] L. K. Aagesen, Y. Gao, D. Schwen, and K. Ahmed, “Grand-potential-based phase-field model for multiple phases, grains, and chemical components,” *Phys. Rev. E*, vol. 98, no. 2, p. 023309, Aug. 2018, doi: 10.1103/PhysRevE.98.023309.
- [97] J. Tiaden, B. Nestler, H. J. Diepers, and I. Steinbach, “The multiphase-field model with an integrated concept for modelling solute diffusion,” *Phys. Nonlinear Phenom.*, vol. 115, no. 1, pp. 73–86, Apr. 1998, doi: 10.1016/S0167-2789(97)00226-1.
- [98] N. Moelans, “A quantitative and thermodynamically consistent phase-field interpolation function for multi-phase systems,” *Acta Mater.*, vol. 59, no. 3, pp. 1077–1086, Feb. 2011, doi: 10.1016/j.actamat.2010.10.038.
- [99] M. Plapp, “Unified derivation of phase-field models for alloy solidification from a grand-potential functional,” *Phys. Rev. E*, vol. 84, no. 3, p. 031601, Sep. 2011, doi: 10.1103/PhysRevE.84.031601.
- [100] A. Karma, “Phase-Field Formulation for Quantitative Modeling of Alloy Solidification,” *Phys. Rev. Lett.*, vol. 87, no. 11, p. 115701, Aug. 2001, doi: 10.1103/PhysRevLett.87.115701.
- [101] A. M. Jokisaari, P. W. Voorhees, J. E. Guyer, J. A. Warren, and O. G. Heinonen, “Phase field benchmark problems for dendritic growth and linear elasticity,” *Comput. Mater. Sci.*, vol. 149, pp. 336–347, Jun. 2018, doi: 10.1016/j.commatsci.2018.03.015.

- [102] PFHub, “Benchmark 3a.1 Results,” PFHub: The Phase Field Community Hub. Accessed: Sep. 05, 2023. [Online]. Available: <https://pages.nist.gov/pfhub/results/benchmark3a.1.ipynb/>
- [103] T. Takaki, S. Sakane, M. Ohno, Y. Shibuta, T. Aoki, and C.-A. Gandin, “Competitive grain growth during directional solidification of a polycrystalline binary alloy: Three-dimensional large-scale phase-field study,” *Materialia*, vol. 1, pp. 104–113, Sep. 2018, doi: 10.1016/j.mtla.2018.05.002.
- [104] Y. Song *et al.*, “Thermal-field effects on interface dynamics and microstructure selection during alloy directional solidification,” *Acta Mater.*, vol. 150, pp. 139–152, May 2018, doi: 10.1016/j.actamat.2018.03.012.
- [105] Y. Lysogorskiy *et al.*, “Performant implementation of the atomic cluster expansion (PACE) and application to copper and silicon,” *Npj Comput. Mater.*, vol. 7, no. 1, p. 97, Jun. 2021, doi: 10.1038/s41524-021-00559-9.
- [106] S. R. Xie, M. Rupp, and R. G. Hennig, “Ultra-fast interpretable machine-learning potentials,” *Npj Comput. Mater.*, vol. 9, no. 1, p. 162, Sep. 2023, doi: 10.1038/s41524-023-01092-7.
- [107] F. C. Robles Hernandez, J. M. Herrera Ramírez, and R. Mackay, “Principles of Solidification,” in *Al-Si Alloys*, Cham: Springer International Publishing, 2017, pp. 173–210. doi: 10.1007/978-3-319-58380-8_8.
- [108] S. Deville, “Ice-templating, freeze casting: Beyond materials processing,” *J. Mater. Res.*, vol. 28, no. 17, pp. 2202–2219, Sep. 2013, doi: 10.1557/jmr.2013.105.
- [109] K. Yin, K. Ji, L. S. Littles, R. Trivedi, A. Karma, and U. G. K. Wegst, “Hierarchical structure formation by crystal growth-front instabilities during ice templating,” *Proc. Natl. Acad. Sci.*, vol. 120, no. 23, p. e2210242120, Jun. 2023, doi: 10.1073/pnas.2210242120.
- [110] D. Tournet, A. J. Clarke, S. D. Imhoff, P. J. Gibbs, J. W. Gibbs, and A. Karma, “Three-Dimensional Multiscale Modeling of Dendritic Spacing Selection During Al-Si Directional Solidification,” *JOM*, vol. 67, no. 8, pp. 1776–1785, Aug. 2015, doi: 10.1007/s11837-015-1444-2.
- [111] C. Garcia Cardona *et al.*, “Crossing the mesoscale no-mans land via parallel kinetic Monte Carlo,” Sandia National Laboratories (SNL), Albuquerque, NM, and Livermore, CA (United States), SAND2009-6226, Oct. 2009. doi: 10.2172/966942.
- [112] M. Rolchigo *et al.*, “ExaCA: A performance portable exascale cellular automata application for alloy solidification modeling,” *Comput. Mater. Sci.*, vol. 214, p. 111692, Nov. 2022, doi: 10.1016/j.commatsci.2022.111692.
- [113] M. Tang, P. C. Pistorius, and J. L. Beuth, “Prediction of lack-of-fusion porosity for powder bed fusion,” *Addit. Manuf.*, vol. 14, pp. 39–48, Mar. 2017, doi: 10.1016/j.addma.2016.12.001.
- [114] W. Wang, J. Ning, and S. Y. Liang, “Analytical prediction of keyhole porosity in laser powder bed fusion,” *Int. J. Adv. Manuf. Technol.*, vol. 119, no. 11, pp. 6995–7002, Apr. 2022, doi: 10.1007/s00170-021-08276-9.
- [115] F. Roters, P. Eisenlohr, L. Hantcherli, D. D. Tjahjanto, T. R. Bieler, and D. Raabe, “Overview of constitutive laws, kinematics, homogenization and multiscale methods in crystal plasticity finite-element modeling: Theory, experiments, applications,” *Acta Mater.*, vol. 58, no. 4, pp. 1152–1211, Feb. 2010, doi: 10.1016/j.actamat.2009.10.058.
- [116] I. Roy, M. Rolchigo, J. Coleman, S. Chen, A. Plotkowski, and Y. Yang, “Understanding solidification of near eutectic alloy using Cellular Automata (CA),” *Comput. Mater. Sci.*, vol. 236, p. 112835, Mar. 2024, doi: 10.1016/j.commatsci.2024.112835.
- [117] Y. Zhang, J. Zhou, Y. Yin, X. Shen, and X. Ji, “Multi-GPU implementation of a cellular automaton model for dendritic growth of binary alloy,” *J. Mater. Res. Technol.*, vol. 14, pp. 1862–1872, Sep. 2021, doi: 10.1016/j.jmrt.2021.07.095.
- [118] A. Choudhury, K. Reuther, E. Wesner, A. August, B. Nestler, and M. Rettenmayr, “Comparison of phase-field and cellular automaton models for dendritic solidification in Al-Cu alloy,” *Comput. Mater. Sci.*, vol. 55, pp. 263–268, Apr. 2012, doi: 10.1016/j.commatsci.2011.12.019.

- [119] T. M. Rodgers, J. D. Madison, and V. Tikare, “Simulation of metal additive manufacturing microstructures using kinetic Monte Carlo,” *Comput. Mater. Sci.*, vol. 135, pp. 78–89, Jul. 2017, doi: 10.1016/j.commatsci.2017.03.053.
- [120] K. Teferra and D. J. Rowenhorst, “Optimizing the cellular automata finite element model for additive manufacturing to simulate large microstructures,” *Acta Mater.*, vol. 213, p. 116930, Jul. 2021, doi: 10.1016/j.actamat.2021.116930.
- [121] J. A. Mitchell *et al.*, “Parallel simulation via SPPARKS of on-lattice kinetic and Metropolis Monte Carlo models for materials processing,” *Model. Simul. Mater. Sci. Eng.*, vol. 31, no. 5, p. 055001, May 2023, doi: 10.1088/1361-651X/accc4b.
- [122] A. L. Garcia, V. Tikare, and E. A. Holm, “Three-dimensional simulation of grain growth in a thermal gradient with non-uniform grain boundary mobility,” *Scr. Mater.*, vol. 59, no. 6, pp. 661–664, Sep. 2008, doi: 10.1016/j.scriptamat.2008.05.039.
- [123] E. R. Homer, V. Tikare, and E. A. Holm, “Hybrid Potts-phase field model for coupled microstructural–compositional evolution,” *Comput. Mater. Sci.*, vol. 69, pp. 414–423, Mar. 2013, doi: 10.1016/j.commatsci.2012.11.056.
- [124] T. M. Rodgers *et al.*, “Simulation of powder bed metal additive manufacturing microstructures with coupled finite difference-Monte Carlo method,” *Addit. Manuf.*, vol. 41, p. 101953, May 2021, doi: 10.1016/j.addma.2021.101953.
- [125] T. M. Rodgers, J. D. Madison, V. Tikare, and M. C. Maguire, “Predicting Mesoscale Microstructural Evolution in Electron Beam Welding,” *JOM*, vol. 68, no. 5, pp. 1419–1426, May 2016, doi: 10.1007/s11837-016-1863-8.
- [126] T. M. Rodgers, J. A. Mitchell, and V. Tikare, “A Monte Carlo model for 3D grain evolution during welding,” *Model. Simul. Mater. Sci. Eng.*, vol. 25, no. 6, p. 064006, Aug. 2017, doi: 10.1088/1361-651X/aa7f20.
- [127] T. M. Rodgers, J. D. Madison, and V. Tikare, “Simulation of metal additive manufacturing microstructures using kinetic Monte Carlo,” *Comput. Mater. Sci.*, vol. 135, pp. 78–89, Jul. 2017, doi: 10.1016/j.commatsci.2017.03.053.
- [128] F. Roters, P. Eisenlohr, T. R. Bieler, and D. Raabe, *Crystal Plasticity Finite Element Methods: in Materials Science and Engineering*. Somerset: Wiley, 2011.
- [129] J. D. Pribe *et al.*, “A Process-Structure-Property Simulation Framework for Quantifying Uncertainty in Additive Manufacturing: Application to Fatigue in Ti-6Al-4V,” *Integrating Mater. Manuf. Innov.*, Aug. 2023, doi: 10.1007/s40192-023-00303-9.
- [130] M. Yaghoobi, K. S. Stopka, D. L. McDowell, L. Graham-Brady, and K. Teferra, “Effect of sample size on the maximum value distribution of fatigue driving forces in metals and alloys,” *Int. J. Fatigue*, vol. 176, p. 107853, Nov. 2023, doi: 10.1016/j.ijfatigue.2023.107853.
- [131] S. R. Yeratapally, A. R. Cerrone, and E. H. Glaessgen, “Discrepancy Between Crystal Plasticity Simulations and Far-Field High-Energy X-ray Diffraction Microscopy Measurements,” *Integrating Mater. Manuf. Innov.*, vol. 10, no. 2, pp. 196–217, Jun. 2021, doi: 10.1007/s40192-021-00216-5.
- [132] R. A. Lebensohn, A. K. Kanjarla, and P. Eisenlohr, “An elasto-viscoplastic formulation based on fast Fourier transforms for the prediction of micromechanical fields in polycrystalline materials,” *Int. J. Plast.*, vol. 32–33, pp. 59–69, May 2012, doi: 10.1016/j.ijplas.2011.12.005.
- [133] J. E. Warner, G. F. Bomarito, G. Heber, and J. D. Hochhalter, “Scalable Implementation of Finite Elements by NASA _ Implicit (SciFEi),” NF1676L-23876, Apr. 2016. Accessed: Sep. 19, 2023. [Online]. Available: <https://ntrs.nasa.gov/citations/20160006300>
- [134] M. G. D. Geers, V. G. Kouznetsova, and W. A. M. Brekelmans, “Multi-scale computational homogenization: Trends and challenges,” *J. Comput. Appl. Math.*, vol. 234, no. 7, pp. 2175–2182, Aug. 2010, doi: 10.1016/j.cam.2009.08.077.
- [135] T. I. Zohdi and P. Wriggers, *Introduction to computational micromechanics*. in Lecture notes in applied and computational mechanics, no. 20. Berlin Heidelberg: Springer, 2005.

- [136] S. Mahadevan, P. Nath, and Z. Hu, “Uncertainty Quantification for Additive Manufacturing Process Improvement: Recent Advances,” *ASCE-ASME J Risk Uncert Engrg Sys Part B Mech Engrg*, vol. 8, no. 1, p. 010801, Mar. 2022, doi: 10.1115/1.4053184.
- [137] *Sequential Monte Carlo Sampling with Python (SMCPy)*. NASA/LaRC. Accessed: Jun. 07, 2024. [Online]. Available: <https://software.nasa.gov/software/LAR-19517-1>
- [138] S. T. Radev, U. K. Mertens, A. Voss, L. Ardizzone, and U. Köthe, “BayesFlow: Learning Complex Stochastic Models With Invertible Neural Networks,” *IEEE Trans. Neural Netw. Learn. Syst.*, vol. 33, no. 4, pp. 1452–1466, Apr. 2022, doi: 10.1109/TNNLS.2020.3042395.
- [139] B. Peherstorfer, K. Willcox, and M. Gunzburger, “Survey of Multifidelity Methods in Uncertainty Propagation, Inference, and Optimization,” *SIAM Rev.*, vol. 60, no. 3, pp. 550–591, Jan. 2018, doi: 10.1137/16M1082469.
- [140] G. F. Bomarito, P. E. Leser, J. E. Warner, and W. P. Leser, “On the optimization of approximate control variates with parametrically defined estimators,” *J. Comput. Phys.*, vol. 451, p. 110882, Feb. 2022, doi: 10.1016/j.jcp.2021.110882.
- [141] E. Borgonovo and E. Plischke, “Sensitivity analysis: A review of recent advances,” *Eur. J. Oper. Res.*, vol. 248, no. 3, pp. 869–887, Feb. 2016, doi: 10.1016/j.ejor.2015.06.032.
- [142] M. Haines, A. Plotkowski, C. L. Frederick, E. J. Schwalbach, and S. S. Babu, “A sensitivity analysis of the columnar-to-equiaxed transition for Ni-based superalloys in electron beam additive manufacturing,” *Comput. Mater. Sci.*, vol. 155, pp. 340–349, Dec. 2018, doi: 10.1016/j.commatsci.2018.08.064.
- [143] J. Herman and W. Usher, “SALib: An open-source Python library for Sensitivity Analysis,” *J. Open Source Softw.*, vol. 2, no. 9, p. 97, Jan. 2017, doi: 10.21105/joss.00097.
- [144] T. Iwanaga, W. Usher, and J. Herman, “Toward SALib 2.0: Advancing the accessibility and interpretability of global sensitivity analyses,” *Socio-Environ. Syst. Model.*, vol. 4, p. 18155, May 2022, doi: 10.18174/sesmo.18155.
- [145] B. Richter, J. D. Pribe, R. Otis, and E. H. Glaessgen, “Uncertainty Quantification of Classical Theories of Dendritic Growth Kinetics Applied to Nickel-Based Alloys,” presented at the 153rd Annual Meeting and Exhibition of The Minerals, Metals & Materials Society (TMS), Orlando, FL: TMS, 2024.
- [146] C. M. Bishop, Ed., “Graphical Models,” in *Pattern Recognition and Machine Learning*, New York, NY: Springer, 2006, pp. 359–422. doi: 10.1007/978-0-387-45528-0_8.
- [147] J. C. Digitale, J. N. Martin, and M. M. Glymour, “Tutorial on directed acyclic graphs,” *J. Clin. Epidemiol.*, vol. 142, pp. 264–267, Feb. 2022, doi: 10.1016/j.jclinepi.2021.08.001.
- [148] A. J. Thomas, E. Barocio, I. Bilonis, and R. B. Pipes, “Bayesian inference of fiber orientation and polymer properties in short fiber-reinforced polymer composites,” *Compos. Sci. Technol.*, vol. 228, p. 109630, Sep. 2022, doi: 10.1016/j.compscitech.2022.109630.
- [149] N. H. Paulson, B. J. Bocklund, R. A. Otis, Z.-K. Liu, and M. Stan, “Quantified uncertainty in thermodynamic modeling for materials design,” *Acta Mater.*, vol. 174, pp. 9–15, Aug. 2019, doi: 10.1016/j.actamat.2019.05.017.
- [150] R. Otis, “Uncertainty reduction and quantification in computational thermodynamics,” *Comput. Mater. Sci.*, vol. 212, p. 111590, Sep. 2022, <https://doi.org/10.1016/j.commatsci.2022.111590>.
- [151] “Guide: Guide for the Verification and Validation of Computational Fluid Dynamics Simulations,” in *Guide: Guide for the Verification and Validation of Computational Fluid Dynamics Simulations (AIAA G-077-1998(2002))*, in AIAA Standards, no. G-077-1998., American Institute of Aeronautics and Astronautics, Inc., 1998. doi: 10.2514/4.472855.001.
- [152] *STANDARD FOR MODELS AND SIMULATIONS*, NASA Technical Standard NASA-STD-7009, Mar. 05, 2024.
- [153] J. Sowards, “Permanent Low-Earth Orbit Testbed for Welding and Joining: A Path Forward for the Commercialization of Space,” 2021. [Online]. Available: <https://ntrs.nasa.gov/citations/20210023463>

- [154] Materials Genome Initiative Autonomous Materials Innovation Infrastructure Interagency Working Group, “Accelerated Materials Experimentation Enabled by the Autonomous Materials Innovation Infrastructure (AMII) A Workshop Report,” National Science Foundation, Alexandria, VA, Workshop report, Jun. 2024.

Supplementary material

Further investigation is warranted as to the effect of differing compute architectures – including node CPU core count, interconnect bandwidth and speed, and memory bandwidth and speed – and operating parameters – including output options and compiler optimizations – on code performance. For example, on the NAS hardware, the PRISMS-PF simulation used OpenMPI (a distributed-memory paradigm) and was set to output restart checkpoint files at the beginning, halfway through the simulation, and at the end. Solution files are written every 4,000 timesteps for a total of fifty solution files. The performance, as indicated by wall clock time, was substantially slower for the same CPU count than for the PRISMS-PF developers (compare Figure 45 to Figure 36). As the PRISMS-PF developers did not output results files, this discrepancy was investigated by turning off file output for the NAS facility runs. However, no substantial speedup was noticed, indicating that file transactions were not responsible for the difference. The PRISMS-PF code was also run without adaptive meshing on the Northeastern University HPC Discovery Cluster in OpenMP (a shared-memory paradigm) using Intel Cascade Lake CPUs (Intel(R) Xeon(R) Platinum 8276 @ 2.20GHz) and yielded comparable execution wall times no matter the choice of file outputs as seen in Figure 45. The relative fraction of time taken up by file output did not vary with increasing CPU core count. One possible explanation for the differences in execution times on various systems is the compiler optimizations available and selected. Re-compiling ICME tools for high-performance computing resources is not a straightforward task and our efforts have shown much variability. Therefore, attention should be focused on understanding the aspects of compute architecture and model parameters that influence code performance.

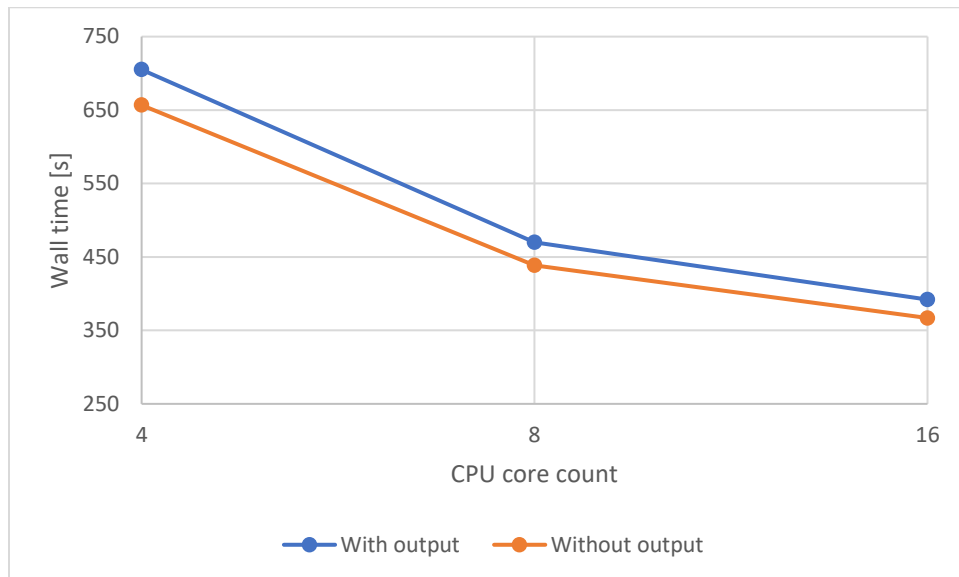


Figure 45: Influence of file output settings on PRISMS-PF performance using the Discovery Cluster.

Attention should also be paid to how computing costs are charged. For example, at NAS the cost per Standard Billing Unit (SBU) of the architecture in terms of node-hours is per node, not per CPU core. The fastest CPU core architecture is not necessarily the best option. For example, using sixteen cores of the Sandy Bridge architecture currently costs 0.105 SBUs. Using sixteen cores of Cascade Lake costs 0.292 SBUs because the charge is as if the entire node was occupied; however, using the entire node (40 cores for Cascade Lake) only costs 0.128 SBUs as the simulation completes more quickly and releases the node sooner, limiting total charged time. Using 128 cores of the AMD Rome node, meanwhile, costs 0.184 SBUs. Consideration should be taken to placement for balancing cost and turn-around time. For comparison, typical CFD simulations being currently conducted by NASA Marshall's Fluid Dynamics Branch for the Artemis Program are routinely requiring upwards of 20,000 SBUs, five orders of magnitude greater than this benchmark. Any ICME tools requiring high-performance computing should be cognizant not only of performance optimization but also of computing expense optimization.

DSI-R parameters using PRISMS-PF: This case was run two ways to benchmark for time: (a) on four cores on a NASA issued laptop, and (b) on 40 cores on the NASA AMES supercomputer Pleiades. A summary of timing can be seen in Table 4. Note that there was only a 6.8x speedup for 10x the cores on a machine designed for fast-

running simulations. This pointed toward some issues with implementation, but this was not further explored during this initial period of performance. Simulations results were identical between the two computers.

Table 4. Benchmarking of PRISMS-PF example: laptop versus HPC.

	Laptop	HPC	Compare: L/H (H/L)
Compute time	~ 1.61e4 sec (~2.50 hrs)	~ 0.24e4 sec (~0.67 hrs)	6.83x (0.15x)
Cores	4	40	0.10x (10x)

Table 5: Comparison of PRISMS-PF running on various NAS architectures and CPU core counts.

Architecture	Mode of Parallelism	CPU Cores	Elapsed Time [s]
Sandy Bridge (0.47 SBU/node-hr) Simulation Cost=0.105 SBUs	MPI	1	
	MPI	2	
	MPI	4	
	MPI	8	2260
	MPI	16	810
	OpenMP	16	1480
Sandy Bridge (0.47 SBU/node-hr)	MPI	2x16	463
	MPI	3x16	405
Ivy Bridge (0.66 SBU/node-hr) Simulation Cost=0.105 SBUs	MPI	1	
	MPI	2	
	MPI	4	2940
	MPI	8	1820
	MPI	16	752
	MPI	20	576
OpenMP	20	Not attempted	
Ivy Bridge (0.66 SBU/node-hr)	MPI	2x20	346
	MPI	3x20	271
Haswell (0.80 SBU/node-hr) Simulation Cost=0.106 SBUs	MPI	1	
	MPI	2	
	MPI	4	3330
	MPI	8	1920
	MPI	16	749
	MPI	24	480
OpenMP	24	Not attempted	
Haswell (0.80 SBU/node-hr)	MPI	2x24	301
	MPI	3x24	259
Broadwell (1.00 SBU/node-hr) Simulation Cost=0.108 SBUs	MPI	1	
	MPI	2	
	MPI	4	2920

	MPI	8	1290
	MPI	16	698
	MPI	28	392
	OpenMP	28	Not attempted
Broadwell (1.00 SBU/node-hr)	MPI	2x28	249
	MPI	3x28	228
Skylake (1.59 SBU/node-hr) Simulation Cost=0.128 SBUs	MPI	1	
	MPI	2	
	MPI	4	2940
	MPI	8	1350
	MPI	16	709
	MPI	32	372
	MPI	40	292
	OpenMP	40	Not attempted
Skylake (1.59 SBU/node-hr)	MPI	2x40	191
	MPI	3x40	160
Cascade Lake (1.64 SBU/node-hr) Simulation Cost=0.128 SBUs	MPI	1	
	MPI	2	
	MPI	4	2190
	MPI	8	1030
	MPI	16	641
	MPI	32	356
	MPI	40	281
	OpenMP	40	Not attempted
Cascade Lake (1.64 SBU/node-hr)	MPI	2x40	181
	MPI	3x40	140
AMD Rome (4.06 SBU/node-hr) Simulation Cost=0.184 SBUs	MPI	1	
	MPI	2	
	MPI	4	
	MPI	8	
	MPI	16	1120
	MPI	32	379
	MPI	64	221
	MPI	128	164
	OpenMP	128	VERY SLOW-Aborted

Table 6. PRISMS-PF computational parameters for solidification example.

Parameter	Value
Dimensions	2
Mesh adaptivity	false
Time step size, max number	0.0005, 400k
Number of outputs	50
Skip print steps	1000
Number of checkpoints	2

Table 7. PRISMS-PF material parameters for solidification example.

Parameter	Value
epsilon	0.01
k	0.14
c0	3.0
lamda	20.0
Dtilde	12.534
Vtilde	9.4536
ltilde	21175.7186
U0	-1.0
U_off	0.9
Y0	5.0
regval	1.0e-10

Acknowledgements

The authors would like to thank the Biological and Physical Sciences (BPS) Division of NASA's Science Mission Directorate (SMD) for funding this project. Some computational resources supporting this work were provided by the NASA High-End Computing (HEC) Program through the NASA Advanced Supercomputing (NAS) Division at Ames Research Center. Thanks to the PRISMS-PF developers for fruitful discussions. Thanks to the MOOSE developers for engaging with this study. Thanks to Dr Tommy Britt for participating in initial discussions during this study period. Thanks to Dr Ellis Crabtree for his helpful reviews of this report.

Disclaimer

The computational tools and other software used and referenced in this report are not intended to imply endorsement by NASA.

<p>The use of trademarks or names of manufacturers in this report is for accurate reporting and does not constitute an official endorsement, either expressed or implied, of such products or manufacturers by the National Aeronautics and Space Administration.</p>
